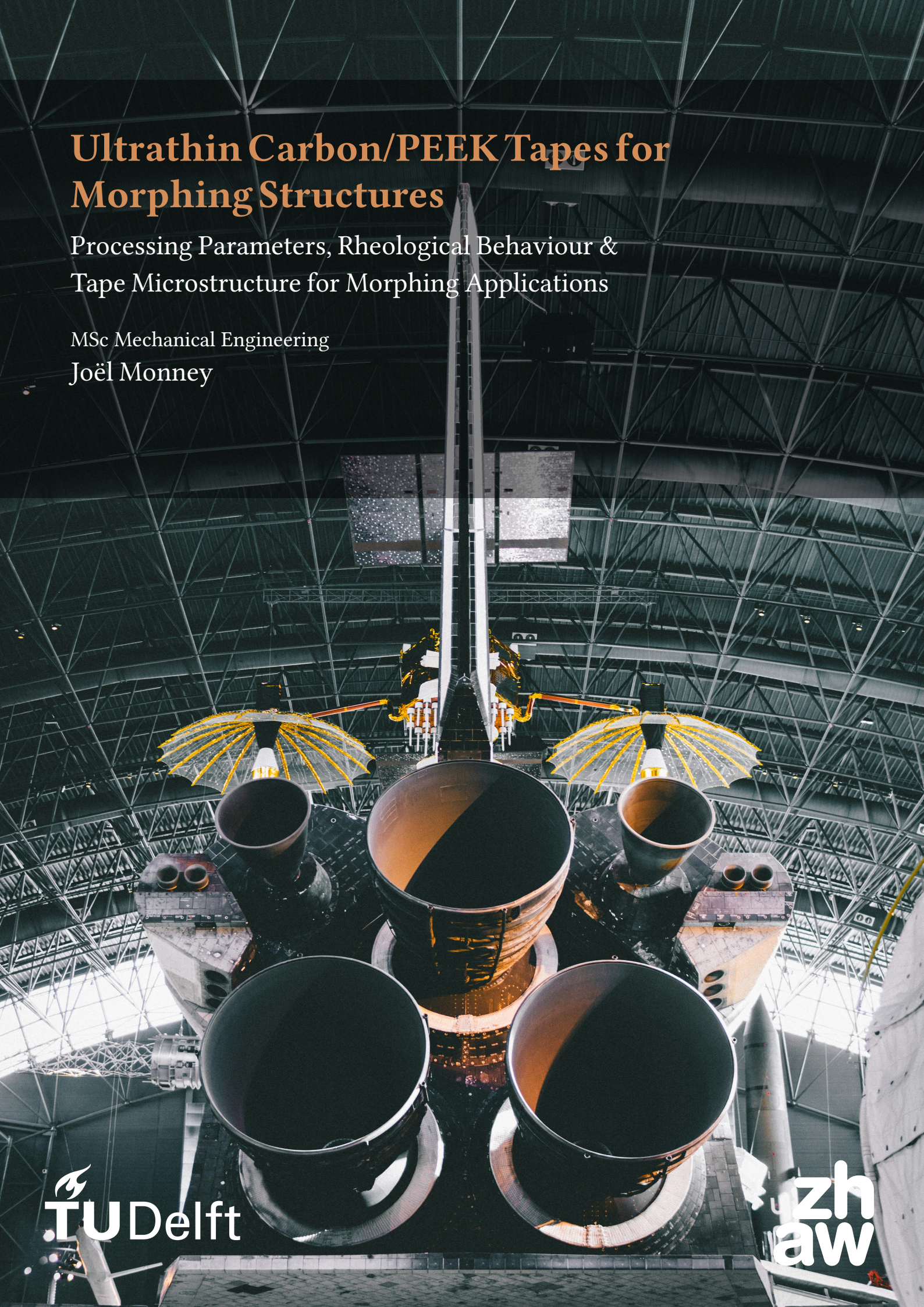
Ultrathin Carbon/PEEK Tapes for Morphing Structures

Processing Parameters, Rheological Behaviour & Tape Microstructure for Morphing Applications

MSc Mechanical Engineering
Joël Monney



TU Delft

zhaw

Zurich University of Applied Sciences

Department School of Engineering

Institute of Mechanical Systems (IMES)

Master thesis

Processing and Microstructural Characterisation of Ultrathin Carbon/PEEK Tapes Produced via Slurry-Based Impregnation for Morphing Applications

Author:
Joël Monney

Supervisors:
Prof. Dr. Marcello Righi
Dr. Shailee Upadhyay
Prof. Clemens Dransfeld

External Supervisor:
Mr. Gerald Piller

Submitted on
February 06, 2026

Study program:
Institute of Mechanical Systems (IMES), Specialisation Lightweight Structures, M.Sc.

Imprint

Project:	Master thesis
Title:	Processing and Microstructural Characterisation of Ultrathin Carbon/PEEK Tapes Produced via Slurry-Based Impregnation for Morphing Applications
Author:	Joël Monney
GitHub:	`github.com/Joel`
Date:	February 06, 2026
Keywords:	thermoplastic composites, PEEK, slurry impregnation, fibre volume fraction, microstructure, TU Delft, ZHAW
Copyright:	Zurich University of Applied Sciences

Study program:
Institute of Mechanical Systems (IMES), Specialisation Lightweight Structures, M.Sc.
Zurich University of Applied Sciences

Co-supervision:
Delft University of Technology (TU Delft)

Supervisor 1:
Prof. Dr. Marcello Righi
Zurich University of Applied Sciences

Supervisor 2:
Dr. Shailee Upadhyay
Delft University of Technology

Supervisor 3:
Prof. Clemens Dransfeld
Delft University of Technology

External Supervisor:
Mr. Gerald Piller
Aerostructures - Senior Analysis Engineer
Aurora Swiss Aerospace

Abstract

Many lightweight high-performance applications have accelerated the adoption of carbon fibre-reinforced thermoplastic composites with thermoplastic matrices, particularly Polyether-etherketone (PEEK) matrices. However, manufacturing high-quality thermoplastic composite tapes remains challenging because high melt viscosity limits fibre impregnation. Wet powder impregnation addresses this by coating fibres with a water-based suspension of thermoplastic particles before consolidation.

This thesis investigates slurry-based manufacturing of unidirectional carbon/PEEK tapes. It relates process parameters and slurry state to tape quality by comparing two impregnation configurations: the Kiss-roller and Nip-roller processes. The investigation is structured around systematic manufacturing campaigns where key process parameters are varied. Line speed and creel tension are investigated for both impregnation routes, and the Nip gap is also varied for the Nip-roller configuration. Tape quality is assessed using gravimetric fibre volume fraction (FVF), while lateral tape quality indicators are computed over a rectangular region of interest (ROI) spanning the full tape width at the tape's mid-length to quantify surface quality. Cross-section microscopy is used to support and bound the interpretation of surface-based metrics.

Within this dataset, the Kiss-roller process shows readable parametric trends. In Campaign 2, increasing line speed from 3.0 to 3.6 m/min systematically decreases FVF, with a smaller drop in speed sensitivity at higher creel tension. In contrast, the Nip-roller process is dominated by strong process variability, which limits the identification of monotonic effects of line speed or creel tension when conditions are not strictly repeated. In the most comparable subset (gap 35, L=0), FVF ranges from 64.5-67.9% at 3.6 m/min and from 64.5-68.8% at 4.2 m/min. The spread within each speed is similar to the difference between speeds. In-process qualitative observations suggest that rapid inlet-regime transitions and tow spreading or overlap quality can yield distinct deposition states under similar setpoints.

Finally, microscopy highlights a key methodological limitation of surface-based analysis: tape quality indicators quantify lateral surface quality variations on the ROI but do not provide direct evidence of through-thickness impregnation. These data provide a consistent basis for discussing the trade-offs in controllability and reproducibility between the two impregnation routes. They show that robust parametric identification requires controlling slurry rheological state for the Kiss-roller process, where surface deposition behaviour is dominant, and stabilising inlet flow regime and tow spreading conditions for the Nip-roller process. Targeted microstructural validation is required when impregnation through the tape thickness governs mechanical reliability.

Acknowledgements

I would like to express my sincere gratitude to my supervisors, Prof. Dr. Marcello Righi, Dr. Shailee Upadhyay, and Prof. Clemens Dransfeld, for their valuable guidance, constructive feedback, and continuous support throughout this project. I would also like to thank Mr. Gerald Piller, who acted as an external supervisor, for his input and review of the thesis.

I would also like to express my heartfelt appreciation to Melvin Moulin, whose support extended far beyond the laboratory. His thoughtful perspectives, help in the refinement and polishing of the samples, and his continuous encouragement during moments of doubt were invaluable. His presence and advice made a tangible difference in both the scientific progress of this thesis and the personal journey it represented.

I am also thankful to the Zurich University of Applied Sciences (ZHAW) and Delft University of Technology (TU Delft) for providing the opportunity and resources to conduct this research.

Contents

Abstract iii

Acknowledgements iv

List of Figures vii

List of Tables xi

1 Introduction 1

2 State of the Art 3
2.1 Context and industrial motivation . . . 3
2.2 Thermoplastic composite tape manufacturing processes . . . 4
2.3 Melt-based Impregnation Processes . . . 5
2.4 Slurry-based Impregnation Processes . . . 6
2.4.1 Kiss and Nip-roller impregnation process . . . 7
2.5 Ultrathin Thermoplastic Tapes and Industrial Motivation . . . 13
2.6 Rheology of Slurries for Composite Processing . . . 14
2.7 Microstructural Quality of Thermoplastic Tapes . . . 16
2.8 Identified gaps and positioning of the present work . . . 18

3 Materials & equipment 19
3.1 Materials . . . 19
3.2 Equipment . . . 22
3.2.1 Tape line . . . 22
3.2.2 Measuring devices . . . 33

4 Methodology 35
4.1 Overview of Experimental Trials . . . 35
4.2 Slurry experiments . . . 37
4.2.1 Slurry preparation . . . 37
4.2.2 Rheology: planned viscosity mapping and study limitations . . . 38
4.2.3 Slurry PEEK weight fraction monitoring during processing . . . 38
4.2.4 Particle Size Distribution Analysis . . . 41
4.3 Tape manufacturing . . . 42
4.4 Tape quality . . . 44
4.4.1 Fibre volume fraction . . . 44
4.4.2 Image-based tape quality . . . 46

5 Results & Discussion 50
5.1 Tape quality after production for Kiss-roller . . . 50
5.1.1 Influence of slurry PEEK weight fraction on FVF . . . 51

5.1.2 Particle size distribution evolution for Kiss-roller . . . 53
5.1.3 Influence of Machine Parameters on FVF Kiss-roller . . . 57
5.1.4 In-Process Qualitative Observations . . . 72
5.1.5 Optical cross-section microscopy (microstructural cross-check) . . . 73
5.2 Tape quality after production for Nip-roller . . . 75
5.2.1 Slurry PEEK wt% variability at sampled positions and PSD signatures 75
5.2.2 Influence of machine parameters on FVF – Nip-roller . . . 79
5.2.3 In-Process Qualitative Observations . . . 82
5.2.4 Optical cross-section microscopy . . . 84

6 Conclusion & Recommendations 85
6.1 Kiss-roller vs Nip-roller: reading framework, key results, and implications . 85
6.1.1 Comparison framework and interpretation cautions . . . 85
6.1.2 Kiss-roller process: dominant sensitivities and the lateral transition-FVF link . . . 85
6.1.3 Nip- roller process: scatter, inlet regimes, and limits of parametric isolation . . . 86
6.1.4 Comparable vs non-transferable: scope of the comparison . . . 86
6.2 Limitations and robustness considerations . . . 87
6.3 Perspectives and recommendations . . . 88

A Materials Data Sheets 89
A.1 Toray Carbon Fibers . . . 89
A.2 PEEK Matrix (Vicote 700 Series) . . . 89
A.3 Additives . . . 89

B Processing and equipment 90
B.1 Test plan for tape line manufacturing . . . 90
B.2 Test plan - Kiss roller . . . 90
B.3 Test plan - Nip roller . . . 99

C Additional results 107
C.1 Methodology of viscosity mapping for different thickener and PEEK wt% . . 107
C.2 Extra PSD plot, Nip roller . . . 109
C.3 Quality metrics heatmap, Nip roller . . . 110
C.4 Complementary Comsol transient images . . . 111

D Models and Derivations 113
D.1 Viscosity Model for Nip-Roller Impregnation . . . 113
D.2 Uncertainty estimation for PEEK content and fibre volume fraction . . . 121
D.3 Uncertainty estimation for slurry PEEK mass fraction . . . 123

E New student, Read me 127
E.1 Project repository and continuation package . . . 127

F Declaration of Originality 128

Bibliography 129

List of Figures

2.1 Schematic illustration of incomplete impregnation in a carbon fibre tow: molten polymer penetrates only part of the tow, leaving an unimpregnated core region where voids and dry fibres remain. 5
2.2 Kiss roller setup sketch [34] 7
2.3 Illustration of the film thickness accumulated on slurry wheel [35] 8
2.4 Schematic of a two-roll coater operating in forward mode.[39] 8
2.5 The Upstream Bank of Liquid Characteristic of a Fully-Flooded Forward Roll Coater in real conditions.[33] 9
2.6 Schematic flow features in forward roll coating: (a) flow near the film-splitting point.[33]; (b) illustration of the important streamlines and features which make up the lower and upper eddies.[39]. 9
2.7 Magnified view of the nip region of a two-roll coater. Comparison between (a) a flooded inlet configuration, with a rolling bank of liquid ahead of the wetting line, and (b) a starved inlet configuration, where liquid supply is insufficient and the dynamic wetting line shifts, typical mechanisms relevant to meniscus roll coating [33]. 10
2.8 A Typical Pressure Profile with Reynolds Conditions at Outlet [33]. 12
2.9 Illustration of a seamless morphing wing concept in aerospace applications. In such systems, the skin must undergo large-amplitude curvature changes while maintaining in-plane load-carrying capacity. 13
2.10 Illustration of the difference between a polymer solution (left) and a particle dispersion/slurry (right). 14
2.11 (A) Thermogravimetric analysis of four additives; (B) residua carbon mass of prepreg manufactured.[8] 16
2.12 Examples of microstructural defects in thermoplastic composites: (a) fibre–matrix debonding, indicating poor interfacial adhesion; (b) void within a fibre tow, acting as a local stress concentrator. Such defects are not captured by global indicators such as fibre volume fraction, but can strongly degrade strength and durability.[9] 17

3.1 Toray T700SC carbon fibre tow: schematic representation and bobbin picture. 19
3.2 Schematic of the stabilisation mechanism of polyether ether ketone dispersion with different surfactants. (A) TX;(B) PEG; and (C) CS1, and CS2 (compound solution). [30] 21
3.3 Overview of the full tape-line equipment used in this study. The eight main modules are highlighted and numbered from (1) to (8). This configuration is installed as a Nip-roller. 22
3.4 Overview of the tape line in the Kiss-roller impregnation configuration. The corresponding process schematic is shown at the top left. The creel (1) and dry-spreading unit (2) are not included. 23
3.5 Kiss-roller impregnation module with annotated zones (A–E). 23

3.6 Open and alternative views of the Kiss-roller impregnation module with annotated zones (A–E). . . . 24
3.7 Overview of the tape line in the Nip-roller impregnation configuration. The corresponding process schematic is shown at the top left. The creel (1) and dry-spreading unit (2) are not included. . . . 24
3.8 Nip-roller impregnation module with annotated zones (A–F). . . . 25
3.9 Nip-roller impregnation module with annotated zones (A–E). . . . 26
3.10 Left: creel holds carbon and glass fibres, showing the region selected for the zoom. Right: zoomed view of the fibre pulling section. . . . 27
3.11 Tension sensor used to monitor the creel tension. . . . 27
3.12 Dry spreading unit used to open the fibre tow before impregnation. . . . 28
3.13 Illustration of the bar-spreading effect on a single tow. . . . 28
3.14 Close-up views of the dry spreading module and adjustable features. . . . 29
3.15 Drying bridge unit. The red arrow shows the manufacturing direction, while the green arrow shows the forced ventilation exit . . . 29
3.16 Main heat unit. . . . 30
3.17 Post spreading unit (a) and calender unit (b) . . . 30
3.18 Post spreading (a) and calendering unit (b) . . . 31
3.19 Illustration of the operating principle of a calendering unit. Red arrows indicate the manufacturing direction, and the second arrow shows the direction of calender pressure. . . . 31
3.20 Pulling unit . . . 32
3.21 Post spreading unit (a) and calender unit (b) . . . 32
3.22 Rheometer geometry sketch, dimensions in [mm] [38]. . . . 33
3.23 Illustration showing the principle behind a laser diffraction measurement with diffracted light from dispersed particles picked up by optimally positioned detectors [50] . . . 33

4.1 Sampling syringe on the bottom and plastic vial. on the top . . . 38
4.2 Slurry sampling procedure used during manufacturing. . . . 39
4.3 Illustration of the position where the top and bottom samples were taken. The distance in centimetres is measured from where the gap is minimal (gap size). . . . 40
4.4 Time dependence of TX100 residue in air. [51] . . . 41
4.5 Heat-resistant glass vial used for slurry drying and additive degradation. Marker-based labelling is used to identify samples before furnace treatment. 41
4.7 Excess of PEEK powder peeling off the tape surface during the melting process 44
4.8 This example (T18) shows image binarisation in ImageJ using a global threshold. The grayscale image is converted to black and white to enhance contrast between fibre-rich and matrix-rich regions before extracting grayscale signals. 47
4.9 The rectangular region of interest (ROI) represented in yellow is centred on the tape width. It is chosen to ensure spatial averaging over a representative central area and to minimise bias from local heterogeneities. . . . 47
4.10 Example of grayscale intensity profile extracted from the binarised image within the defined ROI. The profile represents spatial variations in grayscale intensity across the tape width. . . . 48

5.1 FVF as a function of PEEK weight fraction - Campaign 1 (Kiss-roller impregnation). . . . 51
5.2 FVF as a function of PEEK weight fraction - Campaign 2 (Kiss-roller impregnation). . . . 52

5.3 FVF as a function of PEEK weight fraction - Campaign 3 (Kiss-roller impregnation). . . . 52
5.4 Average PSD measured at different sampling times. . . . 54
5.5 Differential PSD evolution relative to the initial state ($t = 0$(D50=$\sim$9.28 µm)). Positive and negative values indicate respectively an increase or decrease in volume fraction for a given size class. . . . 54
5.6 Average PSD measured at different sampling times. . . . 55
5.7 Differential PSD evolution relative to the initial state ($t = 0$(D50=$\sim$10.00 µm)). Positive and negative values indicate respectively an increase or decrease in volume fraction for a given size class. . . . 55
5.8 Effect of line speed on FVF during Campaign 1 at fixed creel tension, impregnation temperature, and calendar pressure. $\Delta\text{PEEKcontent(abs)} = 1.04\%$. 58
5.9 Effect of line speed on tape morphology during Campaign 1 at fixed creel tension, impregnation temperature, and calendar pressure. Composite-rich: yellow, intermediate: green, PEEK-rich: blue . . . 58
5.10 Effect of line speed on FVF during Campaign 2 at fixed creel tension, impregnation temperature, and calendar pressure. . . . 59
5.11 Effect of line speed on tape morphology during Campaign 2 at $L = 500$ cN, with fixed impregnation temperature and calendar pressure. . . . 60
5.12 Effect of line speed on FVF during Campaign 2 for a higher creel tension. $\Delta\text{PEEKcontent(abs)} = 1.35\%$ . . . 60
5.13 Effect of line speed on tape morphology during Campaign 2 for a medium creel tension. . . . 61
5.14 Effect of line speed on FVF during Campaign 2 for a higher creel tension investigated. $\Delta\text{PEEKcontent(abs)} = 0.63\%$ . . . 61
5.15 Effect of line speed on tape morphology during Campaign 2 at $L = 1000$ cN, with fixed impregnation temperature and calendar pressure. . . . 62
5.16 FVF as a function of creel tension during Campaign 2, with fixed line speed, impregnation temperature, and calendar pressure. $\Delta\text{PEEKcontent(abs)} = 1.21\%$ . . . 64
5.17 Tape morphology as a function of creel tension during Campaign 2, with fixed line speed, impregnation temperature, and calendar pressure. . . . 65
5.18 FVF as a function of creel tension during Campaign 2 for an alternative fixed line speed configuration. $\Delta\text{PEEKcontent(abs)} = 0.58\%$ . . . 66
5.19 Tape morphology as a function of creel tension during Campaign 2 for an alternative fixed line speed configuration. . . . 66
5.20 Influence of calendar pressure on FVF during Campaign 2 at fixed creel tension, line speed, and impregnation temperature. $\Delta\text{PEEKcontent(abs)} = 2.54\%$ . . . 69
5.21 Effect of calendar pressure on tape morphology during Campaign 2 at fixed creel tension, line speed, and melting temperature ($N = 420°\text{C}$). . . . 69
5.22 Influence of calendar pressure on FVF during Campaign 3 at fixed creel tension, line speed, and melting temperature. $\Delta\text{PEEKcontent(abs)} = 0.59\%$. 70
5.23 Effect of calendar pressure on tape morphology during Campaign 3 at fixed creel tension, line speed, and melting temperature ($N = 450°\text{C}$). . . . 71
5.24 In-process photograph of the Kiss-roller impregnation zone shows spatial transition of impregnation and filtration states along the tow. Colored boxes indicate key regions referenced in the text. . . . 72
5.25 In-process picture after drying bridge showing a gap between tapes is already visible at the tape edge (orange). . . . 73

5.26 Optical cross section microscopy highlighting limitations of the heatmap-based *composite-rich*/*PEEK-rich* classification. 74
5.27 Slurry PEEK wt% at sampled positions 75
5.28 ΔPSD comparison for T5 and T6. 77
5.29 ΔPSD comparison with the *top* reference of each run. 78
5.30 FVF as a function of line speed M for $L = 0$ cN. Bar colours indicate the nip-gap setting. 79
5.31 FVF as a function of creel tension L at fixed $M = 3.6$ m/min. Bar colours indicate the nip-gap setting. 80
5.32 Lateral heatmap plot of tape morphology as a function of line speed (subset at $L = 0$ cN). 81
5.33 Lateral heatmap plot of tape morphology as a function of creel tension (subset at $M = 3.6$ m/min). 81
5.34 In-process photographs illustrating rapid changes in slurry state in the Nip (from fully flooded to thickened/starved conditions). 82
5.35 Qualitative Comsol model 83
5.36 In-process pictures illustrating tow spreading/overlap sensitivity and its link to banded tape morphology in the Nip-roller route. 83
5.37 Optical cross section microscopy cross-check highlighting limitations of the heatmap-based *composite-rich*/*PEEK-rich* classification. 84

C.1 Slurries viscosity over shear rate range (10 to 2700 [1/s]) with small PEEK concentration increments.[38] 107
C.2 PSD average curves (Nip route) — additional plots. 109
C.3 COMSOL snapshots (early timesteps). 111
C.4 COMSOL snapshots (mid timesteps). 111
C.5 COMSOL snapshots (late timesteps). 112
C.6 COMSOL snapshot at $t = 1.0$ s. 112

List of Tables

2.1 Key Microstructural Metrics for Tape Quality 17

4.1 Kiss-roller trials and processing parameters (performed trials only). 36
4.3 Nip-roller trials and processing parameters (performed trials only). 37

5.1 Representative measurement uncertainties for FVF and slurry PEEK mass fraction. 50
5.2 Summary of particle size distribution (PSD) averages for slurry samples. . . 56
5.3 Summary of FVF values. The variation amplitude reflects the temporal stability. 57
5.4 Line speed (Campaign 1): Quality metrics 59
5.5 Line speed (Campaign 2, L = 500): quality metrics 60
5.6 Line speed (Campaign 2, L = 700): quality metrics 61
5.7 Line speed (Campaign 2, L = 1000): quality metrics 62
5.8 Line-speed-induced change in FVF from 3.0 to 3.6 m/min. 62
5.9 Creel-tension-induced change in FVF at fixed line speed ($M = 3.0$ m/min). . 64
5.10 Creel tension (Campaign 2, M = 3.0): quality metrics 65
5.11 Creel-tension-induced change in FVF at fixed line speed. 66
5.12 Creel tension (Campaign 2, $M = 3.6$): quality metrics 67
5.13 Calendar pressure (Campaign 2, $N = 420°C$): quality metrics. 70
5.14 Calendar pressure (Campaign 3, $N = 450°C$): quality metrics 71
5.15 Summary of slurry sampling positions and measured PEEK weight fraction . 76
5.16 Subset summary at fixed $L = 0$ cN and gap 35: FVF range (min–max) as a function of line speed M. n is the occurrence. 80

C.1 Quantitative heatmap metrics (creel tension). 110
C.2 Quantitative heatmap metrics (line speed). 110

Nomenclature

Term	Type	Definition
FVF	Acronym	Fibre Volume Fraction.
ROI	Acronym	Region of Interest (central rectangular zone used for signal extraction).
PEEK	Acronym	Poly(ether ether ketone).
PPS	Acronym	Poly(phenylene sulfide).
PVDF	Acronym	Poly(vinylidene difluoride).
UD (tape)	Abbreviation	Unidirectional tape.
PEG	Acronym	Poly(ethylene glycol) (definition implicit in the manuscript).
XG	Acronym	Xanthan gum (thickening agent).
ΔPSD	Convention	PSD difference relative to a reference curve (typically “top”).
top / bot	Convention	Slurry sampling positions: top and bottom of the reservoir.
Transitions [/1000 px]	Convention	Transition rate normalised per 1000 pixels.
Trial ID “Txx”	Convention	Trial identifier (implicit: sequential trial number).
_35	Tag	Nip gap encoded in tenths of mm (0.35 mm).
V	Tag	Sample collected after a visible viscosity increase during the same run.
NS	Tag	No spreading: dry-spreading bar not used.
comp / int / PEEK	Convention	Phase-fraction classes: composite-rich / intermediate / PEEK-rich.
pp	Unit shorthand	Percentage points.
M	Process parameter	Line speed.
L	Process parameter	Creel tension.
N	Process parameter	Impregnation roller set temperature.
O	Process parameter	Calendering pressure.

List of Symbols

Symbol	Meaning
V_f	Fibre volume fraction (FVF).
σ_{V_f}	Propagated uncertainty on V_f.
m_c	Mass of the composite tape segment.
m_f	Mass of fibres contained in the segment.
m_m	Matrix (PEEK) mass in the segment ($m_m = m_c - m_f$).
w_m	Matrix (PEEK) mass fraction in the tape ($w_m = 1 - m_f/m_c$).
ρ_f	Carbon fibre density.
ρ_m	PEEK density.
σ_y	Uncertainty on a quantity y (first-order error propagation).
x_i	Input variable in error propagation.
σ_{x_i}	Uncertainty on x_i.
m_0	Mass of the empty vial.
m_1	Mass of vial + wet slurry.
m_3	Mass of vial after drying/calcination (PEEK residue remaining).
m_{slurry}	Slurry mass ($m_{\text{slurry}} = m_1 - m_0$).
m_{PEEK}	PEEK mass after calcination ($m_{\text{PEEK}} = m_3 - m_0$).
w_{PEEK}	PEEK mass fraction in the slurry.
v	Normalised grayscale contrast variable ($v = \text{Gray_Value}/255$, $v \in [0,1]$).
Gray_Value	8-bit grayscale intensity (0–255).

Glossary of Terms

Term	Definition
Kiss-roller impregnation	Impregnation route in which a slurry film carried by a roll transfers matrix material onto fibres upon contact.
Nip-roller impregnation	Impregnation route in which fibres pass through a roll gap while slurry is entrained and pressurised within the nip.
Slurry	A water-based suspension of polymer powder (e.g. PEEK) with additives, used as a matrix precursor for impregnation.
Creel tension	Tension applied to the fibre tow at the creel, influencing tow spreading, stability, and impregnation conditions.
Line speed	Speed at which the fibre/tape travels through the line, affecting residence time and deposition/impregnation dynamics.
Fibre Volume Fraction (FVF)	Fibre volume fraction in the final composite, computed here from a mass balance and constituent densities.
Mass-balance FVF method	FVF calculation method using the composite mass over a known length, the corresponding fibre mass, and fibre/matrix densities.
First-order error propagation	Uncertainty estimation by linearisation using partial derivatives and root-sum-square combination of independent contributions.
ROI (Region of Interest)	Fixed central rectangular image region used for averaging/extracting the grayscale signal while limiting edge artefacts.
Image binarisation (ImageJ)	Conversion of grayscale images into binary images using a threshold to enhance phase contrast for segmentation.
Grayscale profile	One-dimensional intensity signal extracted across the tape width within the ROI, representing lateral contrast variations.
Composite-rich / Intermediate / PEEK-rich classes	Three-state classification defined by thresholds on the normalised grayscale variable $v \in [0, 1]$.
Transition rate (/1000 px)	Metric quantifying how frequently the classified state changes along the lateral direction, normalised per 1000 pixels.
Run length (mean / max)	Length of contiguous segments of a given class, reported using mean and maximum statistics.
PSD / ΔPSD	Particle size distribution; ΔPSD denotes the difference between PSD curves relative to a chosen reference.
Viscosity mapping	Experimental plan to map viscosity as a function of formulation variables (e.g. PEEK wt%, PEG, XG) to support process design.

Scientists discover the world that exists,
engineers create the world that never was.

— Theodore von Kármán

Chapter 1

Introduction

The Evolution of Composites: UD Tapes Between Thermoset Heritage and Thermoplastic Future

The high-performance composites industry has traditionally relied on thermosetting matrices. This is partly because their low viscosity before cure allows easy impregnation of fibre tow in processes such as resin transfer moulding (RTM) and vacuum-assisted RTM (VARTM) [1]. Thermosetting prepregs, particularly epoxy-based systems, are widely used in aerospace and defence. However, thermosets also have practical and sustainability constraints, including limited out-life, storage requirements, cure-driven processing cycles, and restricted end-of-life options [2].

In response, thermoplastic matrices have gained attention due to their high toughness, weldability, reprocessability, and long shelf life at ambient conditions [3]. These properties make them attractive for applications requiring short cycle times and a high level of automation in sectors such as aerospace, automotive, and energy. A key challenge remains the impregnation of continuous fibres with thermoplastics, as their melt viscosity is typically high, approximately 1000 times more viscous than epoxy, which can hinder infiltration of fibre bundles and limit tape quality and reproducibility [4].

Several routes have been developed to manufacture thermoplastic UD tapes [3, 5–7]. In melt impregnation, the polymer is processed in the molten state and forced between the fibres [5]. Powder-based routes deposit polymer particles onto the tows before melting and consolidation [3]. Solvent impregnation uses polymer solutions followed by solvent evaporation. Film stacking introduces polymer films between dry fibre layers before pressing and heating [6]. Among powder-based approaches, aqueous suspensions provide a practical way to coat continuous fibre tows with thermoplastic particles before consolidation [3, 7].

Polyetheretherketone (PEEK) is a key high-performance thermoplastic used in continuous fibre composites because of its fracture toughness and fatigue resistance, chemical stability, and suitability for reprocessing. Its combination of thermal performance and manufacturability has enabled demanding applications in aerospace, automotive, and marine structures. Recent research on continuous fibre–reinforced PEEK tapes has focused on linking processing conditions to microstructure and homogeneity to improve tape quality and homogeneity [8–10]. In slurry-based impregnation, this requires understanding how slurry state and machine parameters affect deposition behaviour and final tape properties, while accounting for process variability and regime changes during manufacturing.

This work is conducted on the Delft TapeLab, a pilot-scale research platform for unidirectional thermoplastic tape manufacturing [11, 12]. The open architecture of the line enables controlled experimentation on impregnation conditions and rapid iteration of fibre–matrix combinations at small-batch scale, providing an environment suited to studying process structure relationships under experimentally accessible conditions.

Against this background, this thesis investigates slurry-based manufacturing of unidirectional carbon/PEEK tapes, aiming to relate process parameters and slurry state to tape quality. Two impregnation configurations, the Kiss-roller and Nip-roller processes, are investigated and compared under controlled manufacturing conditions. Tape quality is characterised using the gravimetric fibre volume fraction (FVF) and surface-based tape quality indicators evaluated over a defined region of interest (ROI), providing a common basis across both routes.

The work combines systematic manufacturing campaigns with FVF measurements, in-process observations, and cross-section microscopy to guide interpretation of surface-based indicators. By identifying conditions that yield clear parametric trends versus those dominated by regime variability, such as inlet-state transitions and tow spreading or overlap effects, the thesis provides guidance for process optimisation and for designing more identifiable experiments. This supports more robust and reproducible manufacturing routes for high-performance thermoplastic tapes.

Generative AI tools were selectively used to support the preparation of this thesis. Grammarly provided language support, including spelling correction and sentence improvement, without influencing scientific content. Consensus assisted with literature exploration by identifying relevant peer-reviewed publications and aiding the initial screening of sources. ChatGPT 5.2 served as a brainstorming and reflection tool during decision-making, helping to structure thoughts, consider alternative interpretations, and reflect on methodological choices, and assistance in developing Python scripts for data visualisation but did not generate scientific results or conclusions. Mendeley was used to organise references and retrieve information from cited publications. In all cases, the author retained full responsibility for content selection, interpretation, verification, and scientific conclusions. [1]

[1] Generative AI tools were used in a supportive manner during this work: OpenAI (2025), *ChatGPT* (GPT-5.2), https://chat.openai.com; Consensus AI (2025), *Consensus* (web-based version), https://consensus.app.

Chapter 2

State of the Art

2.1 Context and industrial motivation

This chapter positions the present work within the broader context of thermoplastic composite tape manufacturing and slurry-based impregnation. Unidirectional carbon fibre reinforced thermoplastic (CFRTP) tapes are increasingly used as semi-finished products for lightweight structures due to their high specific stiffness, strength, weldability, and recyclability. However, industrial adoption is limited by the challenges of impregnating carbon fibre tows with high-melt-temperature thermoplastic matrices at acceptable production speeds and quality levels.

Various manufacturing routes have been developed to address this challenge, including melt impregnation, powder- and film-based processes, and slurry-assisted strategies. Each method relies on different physical mechanisms for resin transport and consolidation, resulting in distinct limitations regarding fibre volume fraction, void content, process stability, and scalability. Roller-based coating configurations, such as Kiss and Nip rollers, offer promising options for continuous impregnation. However, most existing models are based on simple Newtonian liquids and impermeable substrates, which differ significantly from the slurry–tow systems examined in this work.

The objective of this State of the Art is not only to review existing processes and models, but also to identify the physical principles governing fibre impregnation with thermoplastic matrices and highlight gaps in current knowledge for predicting slurry-based roller impregnation of carbon fibre tows. The chapter first reviews thermoplastic tape manufacturing processes and their main limitations, then focuses on slurry-based impregnation and the specific roles of Kiss and Nip roller configurations. It discusses the rheology and stability of PEEK-based slurries in relation to roller processing, followed by an overview of microstructural quality metrics for thermoplastic tapes, with emphasis on fibre volume fraction. Finally, ultrathin thermoplastic tapes for morphing applications are briefly introduced to motivate the pursuit of thin, homogeneous, well-impregnated tapes that form the basis of the experimental work in this thesis.

2.2 Thermoplastic composite tape manufacturing processes

Overview of existing thermoplastic composite tape manufacturing processes

Thermoplastic composite tapes can be manufactured using several methods, such as pultrusion, film-stacking, commingled-sliver impregnation, compression moulding, and emerging in-situ and additive-manufacturing techniques [13]. These processes primarily differ in resin delivery to the fibre tow and consolidation methods.

Pultrusion and commingled systems provide continuous, automated production and are benchmarks for high-quality profiles [14]. Film-stacking improves local wetting and mechanical properties, while compression moulding is usually used as a secondary consolidation step.

In-situ and additive-manufacturing techniques have attracted recent interest. However, their use for carbon-fibre/PEEK tapes is limited by short residence times and the high melt viscosity of these polymers, which hinders complete impregnation of tightly packed tows [15, 16]. Other routes, such as dry-powder deposition, exist in which polymer particles are mechanically deposited before melting, but they primarily change the form of resin delivery and do not resolve the melt-viscosity limitation.

Criteria used to compare thermoplastic tape manufacturing processes

Thermoplastic tape manufacturing processes are evaluated using three main criteria: mechanical performance, process capability, and final tape quality. Mechanical metrics include tensile and flexural strength, elastic modulus, interlaminar shear strength, and fracture toughness, typically benchmarked to thermoset-based references. Process capability covers line speed, automation, energy demand, and geometric flexibility. Quality indicators such as fibre volume fraction, void content, and impregnation uniformity determine structural integrity and consistency [16–19].

These criteria underscore a key challenge in thermoplastic tape production. Methods that maximise mechanical performance often reduce speed or quality control. Currently, no process achieves high impregnation quality, high throughput, and low void content simultaneously for carbon-fibre/PEEK systems.

Central challenge: Impregnation of carbon fibres with high melt temperature thermoplastics

Even under idealised melt-contact conditions, full penetration of thermoplastic matrices into carbon fibre tows is difficult to achieve. Figure 2.1 visualises the typical outcome: an outer impregnated shell and an unfilled central region. This phenomenon underpins the motivation for exploring impregnation strategies that reduce viscosity prior to consolidation.

The primary challenge in thermoplastic composite tape manufacturing is impregnating carbon fibre tows with engineering polymers such as PEEK or PPS, also PA or PP, for the automotive industry. These polymers maintain high melt viscosity and surface tension at processing temperatures, which restricts resin flow and fibre wetting [15, 20]. Achieving complete impregnation would require extended residence times or elevated temperature and pressure, increasing the risk of thermal degradation and still failing to eliminate voids or unfilled spaces [20].

Traditional infiltration models such as Darcy's law are inadequate because thermoplastic melts display non-Newtonian, viscoelastic behaviour, which invalidates the assumptions of Newtonian flow and prevents accurate prediction of impregnation efficiency [20]. Fibre architecture compounds this issue: carbon fibres, with small filament diameters and tightly packed tows, create low-permeability pathways that molten matrices cannot easily penetrate within practical processing conditions. While improved wetting—through reduced melt surface tension and increased fibre surface energy—can enhance impregnation, achieving such conditions remains challenging in industrial thermoplastic processing [21, 22].

While solvent-assisted and ultrasound-assisted methods can temporarily reduce apparent viscosity, their mechanisms are not well understood and have not achieved reliable, continuous impregnation for carbon-fibre/thermoplastic tapes [23, 24]. The combined challenges of rheology, thermal stability, permeability, and industrial requirements significantly limit the suitability of melt-based impregnation for the industrial production of ultrathin carbon fibre/PEEK tapes.

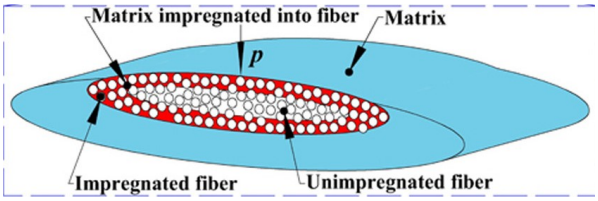


Figure 2.1: Schematic illustration of incomplete impregnation in a carbon fibre tow: molten polymer penetrates only part of the tow, leaving an unimpregnated core region where voids and dry fibres remain.

2.3 Melt-based Impregnation Processes

Melt-based impregnation is common in thermoplastic composite manufacturing because it lets the polymer matrix form directly around continuous fibre tows without drying them first. In tape production, this method includes film stacking, commingled yarn consolidation, and direct melt coating. It is often used as a benchmark for high fibre volume fractions and low void contents [3, 6].

Raising temperature or pressure can help impregnation by lowering melt viscosity and improving wetting. However, this also narrows the processing window because of thermal stability limits and the risk of disturbing the fibre structure [21, 22]. Thermoplastic melts also have non-Newtonian and viscoelastic properties.

An alternative strategy is to reduce effective viscosity during impregnation by suspending thermoplastic particles in a liquid carrier, improving fibre wetting before consolidation. This motivates the use of slurry-based impregnation methods, which address the primary physical bottleneck in thermoplastic tape manufacturing but introduce new considerations regarding slurry rheology, stability, and coating mechanics. The next section discusses these topics.

2.4 Slurry-based Impregnation Processes

Slurry impregnation reduces the effective viscosity during impregnation by dispersing the thermoplastic powder in a carrier liquid, allowing the fibres to be wetted in a low-viscosity state before the polymer melts [3, 25]. In this process, a continuous fibre tow is coated with a polymer slurry; the liquid phase is then removed by evaporation or drying, and the remaining polymer particles are consecutively consolidated through heating and pressure.

Since impregnation occurs when the polymer is in a slurry state rather than a molten state, suspension processing overcomes the viscosity limitation of polymer melt-based processes, which do not allow complete infiltration of carbon fibre tows within practical dwell times [15]. However, this paradigm shift introduces new considerations: the suspension rheology changes over time, particles can sediment, and the distribution and transfer of liquid onto the tow are highly dependent on the coating mechanism. These aspects are essential for continuous tape manufacturing and are discussed in the following sections.

Physical mechanisms enabling improved fibre wetting

Slurry-based impregnation enhances fibre impregnation by using a low-viscosity liquid to transport the polymer, which infiltrates the tow more effectively than molten thermoplastics [26, 27]. This liquid phase reduces flow resistance and surface tension, enabling contact with internal filaments. Mechanical effects, such as fibre spreading and differential slippage during slurry impregnation, also contribute to increasing fibre surface exposure and resin access. Fine polymer particles are deposited throughout the tow during infiltration, supporting subsequent fusion and consolidation with a more uniform resin distribution [3].

While this mechanism improves access to fibre surfaces, its effectiveness depends on slurry rheology, particle stability, wettability of carrier liquid, and the method of liquid transfer to the tow. These parameters must be controlled to prevent sedimentation, non-uniform coating, or local pore entrapment.

Challenges related to slurry rheology, stability, and process control

Slurry-based impregnation presents new challenges, as the suspension's viscosity and structure change during processing. High solids content raises viscosity and can cause shear thickening, which complicates liquid transfer and uniform coating [6, 28, 29]. Additionally, particle sedimentation and phase separation threaten spatial uniformity, so stabilisation strategies such as polymeric thickeners or surfactants are needed to maintain a workable suspension over time [30].

These effects show that slurry impregnation depends not only on the liquid state, but also on how the suspension behaves during handling. Viscosity drift, solvent loss, or sediment buildup in the bath can directly affect fibre wetting and final tape quality. Traditional rheological measurements do not fully predict performance during continuous line operation, where flow, residence time, and mechanical interaction with the fibre tow determine coating efficiency [31]. Consistent impregnation requires reproducible slurry properties, highlighting the need to understand slurry transfer to the tow in continuous processes.

2.4.1 Kiss and Nip-roller impregnation process

In continuous tape manufacturing, the slurry is typically transferred onto the fibre tow using roller coating systems. Roller coating allows for controlled deposition of a thin liquid film and is widely used in industry for fluids of varying viscosity [32, 33]. However, most analytical models and industrial applications assume rigid, impermeable substrates, which differ fundamentally from a tensioned, porous carbon fibre tow.

Kiss-roller and nip roller configurations are considered here. They determine the amount of slurry entrained on the tow and how it is squeezed into the tow, directly linking roll mechanics to impregnation efficiency in slurry-based tape production.

Kiss-roller

The kiss roller configuration (Fig. 2.2) is one of the simplest roller-based coating systems. A rotating roller, partially immersed in a slurry bath, entrains a liquid film and transfers it directly to the substrate. The amount of liquid picked up depends on hydrodynamic entrainment, which is influenced by roller speed, liquid viscosity, and surface tension, as described in classical film-pick-up models [34, 35].

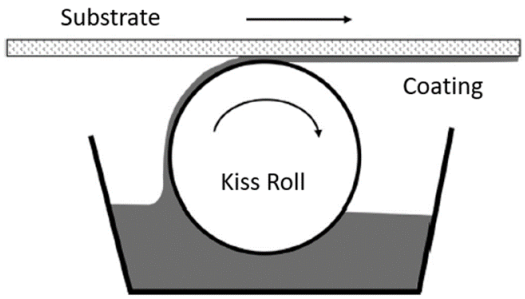


Figure 2.2: Kiss roller setup sketch [34]

In the coating literature, Kiss-rollers are typically studied in roll-to-roll systems with rigid substrates or alongside downstream metering elements that control final coating thickness. As a result, most analytical models focus on film-splitting and thickness distribution at the nip, rather than direct transfer to a porous substrate used in kiss roller [32, 33, 36, 37].

However, analytical models have been developed to describe liquid pick-up and film formation on a rotating roller partially immersed in a bath, independent of downstream processing (Fig. 2.3). These models relate the hydrodynamic entrainment, liquid flux, capillarity number and film thickness to operating parameters such as roller speed and fluid rheology for both Newtonian and non-Newtonian fluids. While originally designed for roll coating machinery, they provide a first-order framework for estimating liquid available for transfer in kiss roller configurations [35].

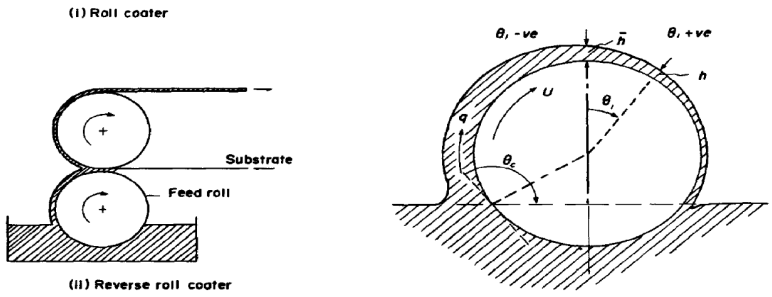


Figure 2.3: Illustration of the film thickness accumulated on slurry wheel [35]

For slurry-based fibre impregnation, this modelling strategy offers a practical approximation of the Kiss-roller pick-up mechanism, while intentionally excluding fibre compressibility, porosity, and downstream consolidation. It was used as an initial analytical tool in early experiments and previously applied in the Master's thesis of Andrieux, where it supported the characterisation of slurry pick-up behaviour rather than tape manufacturing [38]. Although simplified, it provides a useful starting point for interpreting experimental trends and underscores the need for further refinement to address specific interactions between the slurry-coated roller and a fibre tow.

Nip-roller

In a nip roller configuration (fig. 2.4), the substrate is compressed and coated as it passes through the narrow gap between two counter-rotating rolls. The nip region is critical to coating performance because pressure buildup, meniscus effects, and film splitting determine the amount of liquid transferred and retained on the substrate [39]. Classical analytical and numerical models predict pressure distribution, velocity fields, and resulting film thickness.

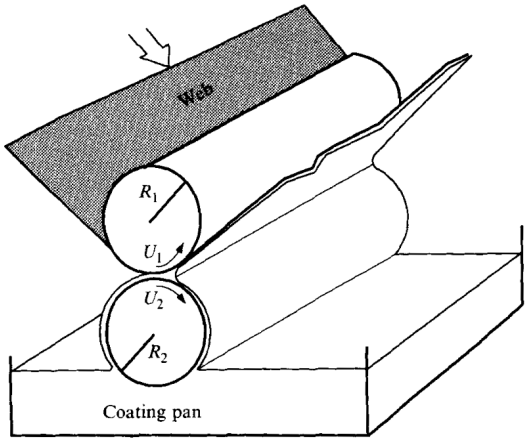


Figure 2.4: Schematic of a two-roll coater operating in forward mode.[39]

Most studies describe nip coating in roll-to-roll systems with rigid, impermeable substrates transported horizontally [39, 40]. In this context, the configuration is inverted, with the tow moving vertically between horizontally aligned rolls. Gravitational effects are negligible compared to viscous and pressure-driven mechanisms. Therefore, lubrication-theory predictions from classical nip studies are considered transferable, though their applicability

to a porous, deformable fibre tow requires careful evaluation for slurry impregnation[39, 40]. The following subsection, therefore, reviews the lubrication-theory models typically used to describe nip flow and film formation.

Fundamental Nip Physics - Pressure, Film Split and Meniscus Effects

Studies of Newtonian meniscus roll-coating show that hydrodynamic entrainment between two counter-rotating rolls governs flow in the nip. No-slip boundary conditions at both roller surfaces create a quadratic velocity profile, resulting in two recirculating eddies and a narrow unidirectional transfer jet, which is the main pathway for liquid transport.[39] Capillary action at the upstream meniscus generates a sub-ambient pressure field, with pressure peaking at the nip centre. These features can be observed experimentally in Figure 2.5, which shows the upstream liquid bank and eddy formation in a fully-flooded roller.

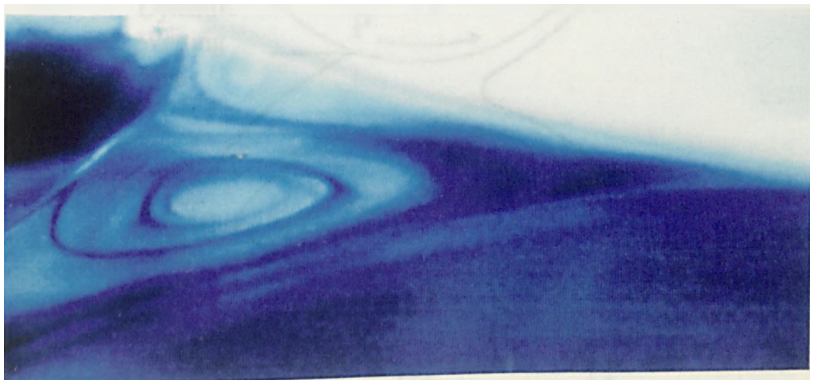
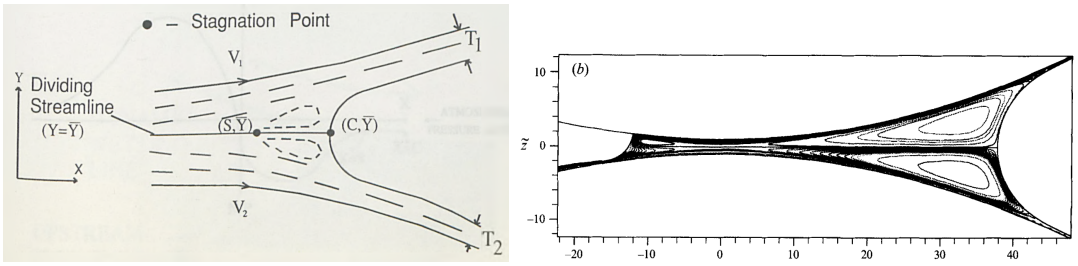


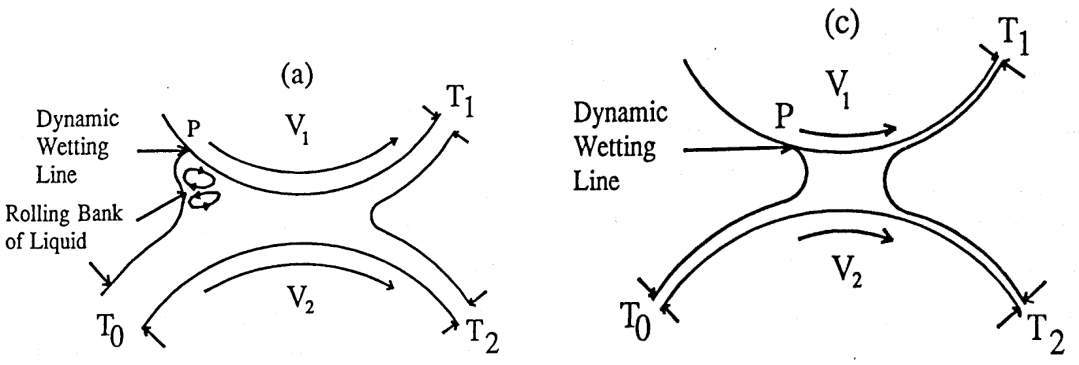
Figure 2.5: The Upstream Bank of Liquid Characteristic of a Fully-Flooded Forward Roll Coater in real conditions.[33]



(a) Film-splitting region. **(b)** Recirculating eddies.

Figure 2.6: Schematic flow features in forward roll coating: (a) flow near the film-splitting point.[33]; (b) illustration of the important streamlines and features which make up the lower and upper eddies.[39].

Gap distance significantly affects the pressure field and coating thickness. Increasing the gap lowers peak pressure and increases leakage-film thickness [33]. Under fully-flooded inlet conditions (fig. 2.7a), the film thickness approaches the mechanical separation between the rolls. In starved inlet conditions (fig. 2.7b), reduced liquid supply causes the film to become much thinner than the gap [33]. The geometry of this film-splitting region and the recirculating eddies is illustrated schematically in Figure 2.6a, while Figure 2.6b shows numerical predictions of the same flow field under starved inlet conditions. These flow features motivate analytical formulations based on lubrication theory, which are reviewed in the next subsection.



(a) Flooded inlet (meniscus roll coating). **(b)** Starved inlet (reduced film supply).

Figure 2.7: Magnified view of the nip region of a two-roll coater. Comparison between (a) a flooded inlet configuration, with a rolling bank of liquid ahead of the wetting line, and (b) a starved inlet configuration, where liquid supply is insufficient and the dynamic wetting line shifts, typical mechanisms relevant to meniscus roll coating [33].

Lubrication-Theory-Based Analytical Models

Lubrication theory serves as the main analytical framework for nip roller coating. With the thin-film approximation, the velocity field combines Couette and Poiseuille flow, and the pressure profile follows a Reynolds-type formulation [39]. These models typically assume Newtonian rheology, negligible inertia, and a rigid, impermeable substrate.

This framework predicts velocity, pressure, and liquid flux through the nip. Lubrication theory applies to both fully flooded and starved inlet conditions [33]. In the fully flooded case, the inlet is completely filled with liquid and the upstream pressure decays to atmospheric, so the flux is determined directly from the lubrication equations. Under starved conditions, the free surface moves closer to the nip, making the previous boundary condition invalid. In this case, the flux is specified as an inlet parameter, while lubrication theory still governs the internal flow.

Although these formulations are the classical basis of nip-coating theory, they do not account for substrate porosity, fibre-tow deformation, capillary uptake, or shear-dependent viscosity. Their use for slurry impregnation should therefore be considered with caution. The next subsection summarises how numerical and finite-element methods have extended these analytical models.

Numerical and Finite-Element Modelling of Nip-region Flow

Numerical techniques, including finite-element simulation, have been developed to overcome the limitations of analytical lubrication models and to describe two-dimensional flow near free surfaces and menisci in the nip region [33, 39, 41]. These methods solve the steady Navier–Stokes equations using velocity–pressure formulations and account for dynamic wetting lines and surface-tension effects, which are difficult to capture analytically. Numerical results have identified nested-eddy substructures and transitions where secondary fluid-transfer jets form.

Typical boundary conditions include no-slip at roller surfaces, zero shear stress and kinematic conditions at free surfaces, and no-traction at outflow boundaries to ensure mass and

momentum conservation. Although these methods are more comprehensive, they introduce challenges such as mesh distortion near curved menisci and increased computational cost when exploring large parameter spaces [33, 39].

Numerical models extend predictive capabilities beyond analytical limits, especially in regions where lubrication theory does not apply. However, they still assume a continuous Newtonian fluid and a rigid substrate, so they do not account for fibre-tow porosity, compressibility, or particle-laden slurry behaviour. For continuous composite-tape impregnation, these models are mainly conceptual rather than directly predictive.

Film Thickness Control and Effect of Nip Pressure

Liquid transfer in nip roller coating is strongly controlled by the pressure distribution within the nip and the inlet liquid-supply condition. fig. 2.8 illustrate a pressure profil with Reynolds conditions at outlet in fully flooded condition. In the nip under fully flooded operation, a rolling bank of liquid forms upstream, and pressure increases smoothly as the liquid moves through the narrowing gap. This promotes stable, continuous film formation, and film thickness approximates the minimum gap [33].

When the inlet supply is insufficient, starvation occurs, and the rolling bank gradually disappears. Thompson et al. categorise starved conditions as moderate (fig. 2.7b) or ultra-starved, depending on the degree of liquid shortage [33]. In these regimes, pressure buildup is localised at the zero-reverse-flow boundary, where all supplied liquid passes unidirectionally through the nip. This altered pressure distribution reduces the load-carrying capacity of the nip and changes liquid-transfer behaviour, potentially compromising film uniformity. Observations of meniscus roll-coating also identify transitions where secondary transfer jets emerge beyond defined critical flow rates, showing that nip-pressure behaviour and inlet supply together define the liquid-transfer regime [39].

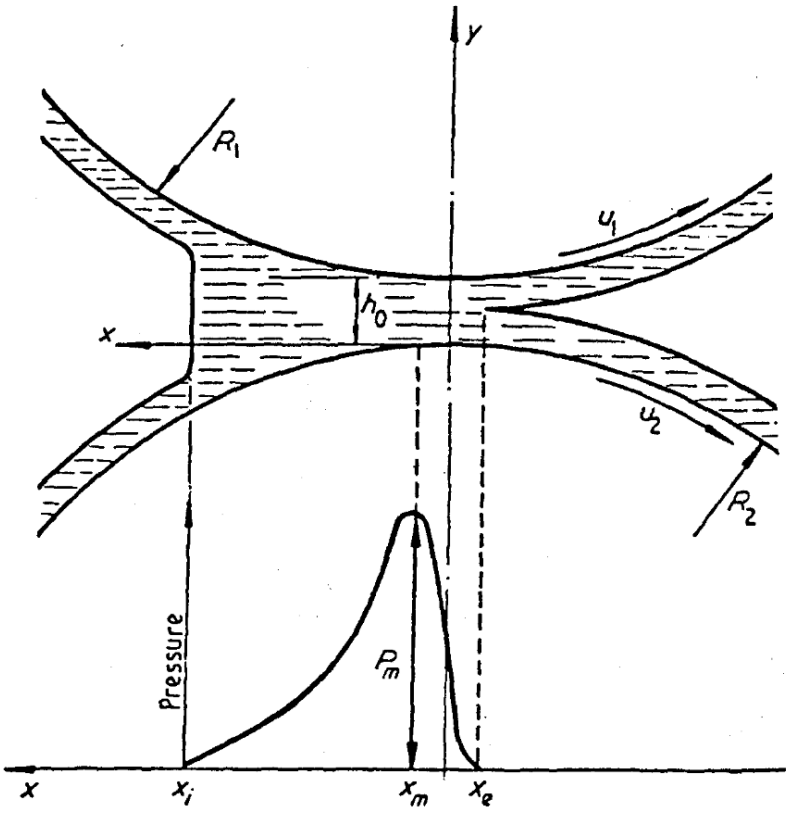


Figure 2.8: A Typical Pressure Profile with Reynolds Conditions at Outlet [33].

Extension to Non-Newtonian Fluids

Non-Newtonian behaviour has been incorporated into nip analysis mainly through simplified constitutive models. Reverse-roller coating of a Williamson pseudoplastic fluid provides analytical expressions for velocity, flow rate, and pressure gradient using perturbation-based lubrication theory [42].

Roll-over-web coating has also been studied using a simplified Phan-Thien-Tanner viscoelastic model [43]. Increasing the Weissenberg number and extensibility parameter raises the pressure gradient in the nip, while viscoelastic effects reduce lubrication pressure, roll force, and power demand [43].

In summary, non-Newtonian extensions provide valuable information on how rheological parameters influence pressure and film formation in the contact line, but they remain fundamentally limited by their treatment of the liquid as a homogeneous, single-phase continuum.

Scope and Limitations for Slurry-Based Fibre Impregnation

Before extending these findings to fibre-based systems, it is essential to underline a key point: all preceding studies are formulated for impermeable, continuous substrates.

Existing nip-roller models provide a robust theoretical and numerical framework for predicting liquid flow, pressure distribution and final film thickness in roll-coating systems comprising rigid rolls and continuous, impermeable substrates [33, 39, 42, 43]. These models

assume Newtonian or simplified non-Newtonian rheology, steady-state two-dimensional flow and continuous liquid films.

In slurry-based fibre impregnation, additional complexities arise from the non-Newtonian behaviour of the slurry, the porous and deformable nature of fibre tows, and the interaction between nip pressure and fibre compaction. These effects are not explicitly captured by classical lubrication-based or numerical nip roller models. While such models are valuable for understanding liquid metering and transfer mechanisms, their applicability to slurry impregnation of fibre-based substrates is limited and requires careful interpretation.

Taken together, the literature reveals a clear knowledge gap: no existing nip-roller model currently predicts slurry flux into a porous tow or accounts for particle-mediated impregnation under deformation. This gap directly motivates the experimental investigation presented in Chapter 4.

2.5 Ultrathin Thermoplastic Tapes and Industrial Motivation

Ultrathin thermoplastic tapes enable laminate skins that deform continuously without hinges, an essential feature for morphing aerospace structures (Fig. 2.9). Their bending-compliant behaviour is not a mechanical goal in this thesis, but it motivates the industrial need for thin, homogeneous tapes. Continuous UD thermoplastic tapes can be as thin as $\approx$ 0.1 mm.[3] Thinner tapes significantly reduce bending stiffness, which is essential for morphing skins, compliant mechanisms, and adaptive laminates.[17]

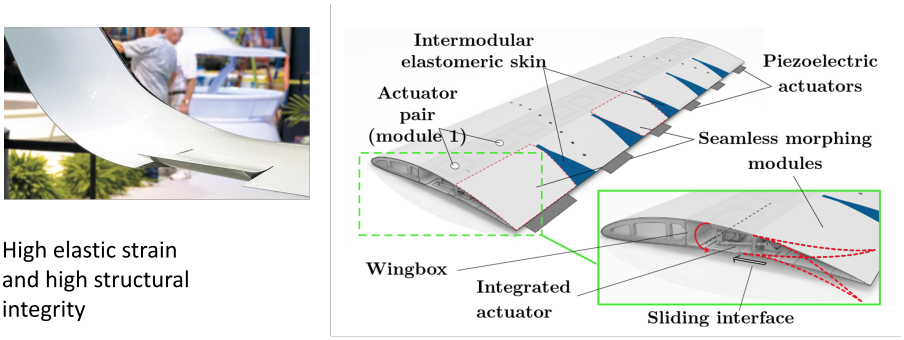


Figure 2.9: Illustration of a seamless morphing wing concept in aerospace applications. In such systems, the skin must undergo large-amplitude curvature changes while maintaining in-plane load-carrying capacity.

Although this thesis does not directly address morphing performance, it highlights the need for thin, homogeneous tapes with controlled impregnation and fibre volume fraction. Industrial tape technologies typically prioritise structural load-bearing rather than ultra-thin flexibility. Manufacturing tapes below 0.15 mm presents challenges, including increased sensitivity in resin metering, higher risk of fibre architecture disturbances, and greater impact from voids or resin-rich zones.

This work focuses on improving manufacturing quality, specifically impregnation uniformity and fibre volume fraction control, which are essential for future morphing-capable laminates.

2.6 Rheology of Slurries for Composite Processing

Slurries for fibre impregnation are colloidal suspensions of solid particles in a liquid carrier [44]. Their behaviour depends on particle–fluid interactions, particle concentration, and the liquid phase composition. Slurry flow is governed by three main mechanisms: Brownian motion (relevant for submicron particles), DLVO forces (Derjaguin–Landau–Verwey–Overbeek) (van der Waals attraction versus electrostatic repulsion), and sedimentation when gravity overcomes colloidal forces [44]. For the micron-scale PEEK powders in this study, Brownian motion does not provide adequate suspension stability, so formulation strategies are required to prevent settling.

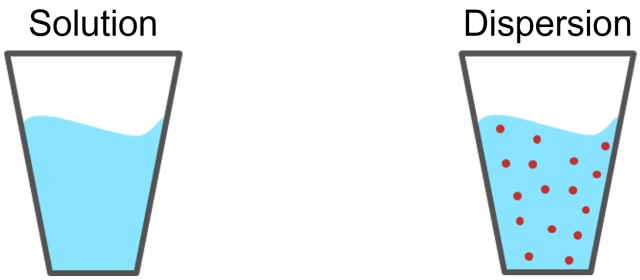


Figure 2.10: Illustration of the difference between a polymer solution (left) and a particle dispersion/slurry (right).

Unlike polymer solutions, slurries exhibit particle–particle and particle–fluid interactions that result in non-Newtonian behaviour and time-dependent viscosity. These factors must be considered when analysing slurry flow in the nip and liquid transfer to the tow during continuous tape processing.

Rheological Parameters Relevant to Composite Impregnation

For roller-based impregnation, viscosity, yield stress, and shear-dependence are the key factors influencing impregnation efficiency [38]. Viscosity and surface tension determine the slurry's ability to penetrate fibre tows and control film thickness on the roller. High viscosity increases pick-up but can hinder wetting and cause non-uniform deposition, particularly at high solids contents such as 30–40 wt% PEEK [21, 22, 38].

Shear-thinning behaviour, where viscosity decreases as shear rate increases, is advantageous for tow impregnation. High shear during coating reduces viscosity and aids polymer infiltration, while at rest or in the coating bath, higher viscosity prevents settling [45]. PEEK-based systems typically exhibit three rheological regimes: shear-thinning at low shear, an intermediate plateau, and shear-thickening at very high shear due to hydrocluster formation [38]. As PEEK concentration increases, the transition shear rate rises, reflecting denser particle networks that require stronger shear to disrupt [38].

These rheological characteristics constrain the usable process window: the slurry must be fluid enough under kiss/nip shear to wet fibres, yet sufficiently structured to remain stable in the reservoir. However, most existing studies focus on bulk rheometry and do not establish how these behaviours translate to local shear conditions inside the nip during continuous tape manufacturing.

Slurry Stability, Sedimentation and Time-Evolution

The stability of slurry does not depend only on viscosity. Suspensions can remain fluid and kinetically stable if their microstructure forms weak flocs, covering the entire space, which limits sedimentation. At rest, gravity causes particles to sediment, concentrating solids at the bottom and reducing viscosity in the upper part. When shearing resumes, the particles resuspend and viscosity increases sharply. Continuous agitation or recirculation can delay this sedimentation [38].

Evaporation of the carrier liquid also destabilises the slurry. In PEEK-based suspensions, water loss increases viscosity and can lead to uneven wetting and variations in fibre volume fraction if drying is not controlled [46].

Overall, slurry stability is dynamic: viscosity changes within minutes, not just during formulation. Most studies evaluate stability under static or bulk shear conditions and do not address the evolution of sedimentation or evaporation at time scales relevant to the nip ($\approx$0.5-2 s of interaction) in continuous tape manufacturing. This gap has an impact on process design, as formulations must be selected based on the impregnation time scale, not just on initial rheological measurements.

Role of Additives: XG – Triton X-100 – PEG

Because thermoplastic powders in the typical range of 10 μm do not remain suspended on their own, additives are included primarily for functional processability rather than as variables for scientific study. Their role is to ensure that the slurry remains handleable and stable over the timescale relevant to roller impregnation.

Xanthan Gum (XG) - is a high-molecular-weight polysaccharide that significantly increases low-shear viscosity and provides strong shear-thinning [47]. In slurries, it forms network-like bridges between particles, creating a soft three-dimensional microstructure that prevents sedimentation even at low polymer fractions, above a critical stabilisation concentration (CSC $\approx 2\,\mathrm{g\,l^{-1}}$ in model systems) [47]. These networks break under shear and reform when shear stops, providing both processing fluidity and kinetic stability [8, 30].

Triton X-100 (TX) - is a nonionic surfactant used to improve wetting of the powder and fibres. While it enhances dispersion, it does not provide long-term suspension stability; PEEK powder in the typical range of 10 μm slurries stabilised only with Triton will eventually sediment [30].

Polyethylene Glycol (PEG) - provides steric stabilisation by adsorbing polymer chains around particles, forming a soft shell that prevents close contact and slows sedimentation. In PEEK systems, adding PEG (1.25–2.5 %) increases low-shear viscosity while keeping viscosity manageable at typical coating shear rates [38]. Combined with Triton, PEG significantly extends usable pot-life (from about 5 minutes to 50 minutes) and prevents rapid densification [30].

Overall, Triton improves wetting and reduces contact angle, while XG and PEG provide stability through structural and steric effects. In this work, additives serve as processing enablers rather than modelling targets.

Impact of Additives on Residual Carbon and Interlaminar Performance

Recent studies indicate that additives in slurry systems do not fully decompose during drying or high-temperature melting. Thermogravimetric tests of different surfactants (AOT, Triton X-100, A25) and a thickener (XG) show significant differences in residual carbon at 400°C. AOT leaves the lowest residue (approximately 19%), while Triton produces nearly six times more carbon (Fig. 2.11) [8].

These residues remain at the fibre–resin interface after melting, where they can create stress-concentration sites and hinder self-bonding between PEEK particles. Short-beam shear tests confirm that interlaminar strength decreases as residual carbon increases. Compared to a circulating ethanol-based reference, retention rates of interlaminar shear strength dropped by 24.4% for AOT, 50.9% for A25, and 60.1% for Triton (Fig2.11) [8].

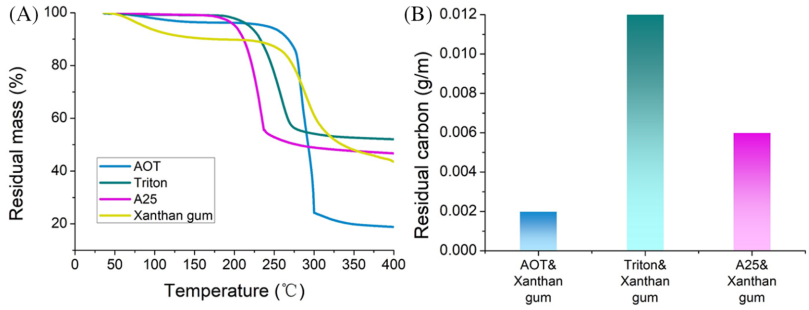


Figure 2.11: (A) Thermogravimetric analysis of four additives; (B) residua carbon mass of prepreg manufactured.[8]

This finding shows that additives are not just "processing aids." Their decomposition products directly affect composite quality and serve as key performance parameters in thermoplastic prepreg manufacturing.

2.7 Microstructural Quality of Thermoplastic Tapes

While various microstructural indicators are used to assess unidirectional thermoplastic composite tapes, this study focuses on FVF, as it was the metric systematically measured across all samples.

FVF is defined as the ratio of fibre volume to the total composite volume. It is quantified using mass-based approaches combined with known fibre and matrix densities. A stable FVF is essential for consistent mechanical properties along the tape. Process parameters such as polymer content in the slurry bath and line speed directly affect FVF. Industrial thermoplastic Carbon fibre/PEEK tapes typically target FVF values between 0.58 and 0.62 [3].

Other microstructural metrics are not applied in this study. Due to time and equipment constraints, additional indicators such as void content (optical microscopy, µCT), fibre alignment or misalignment (µCT, von-Mises distribution), fibre neighbourhood topology (Voronoi tessellation), tortuosity, and fibre intersection density were not implemented. These methods offer deeper insight into impregnation uniformity and microscopic defects, and may be considered in future work [9, 10, 18, 25, 48, 49].

Beyond global indicators such as fibre volume fraction, local microstructural defects at the fibre–matrix scale strongly influence mechanical performance. In particular, interfacial debonding and voids act as stress concentrators and initiation sites for cracks [8]. Figure 2.12 presents micrographs illustrating these two defect types.

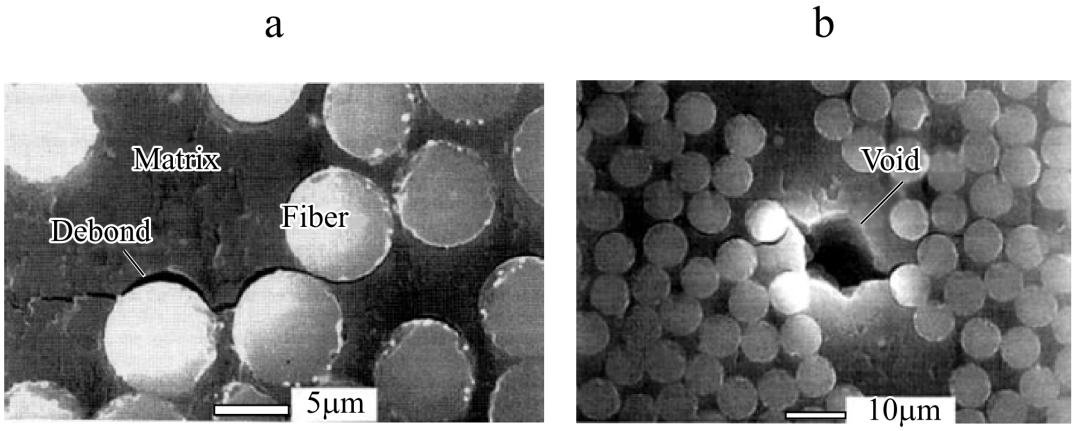


Figure 2.12: Examples of microstructural defects in thermoplastic composites: (a) fibre–matrix debonding, indicating poor interfacial adhesion; (b) void within a fibre tow, acting as a local stress concentrator. Such defects are not captured by global indicators such as fibre volume fraction, but can strongly degrade strength and durability.[9]

A summary of these complementary metrics is provided in the following section.

Table 2.1: Key Microstructural Metrics for Tape Quality

Metric	Description	Measurement	Impact
FVF [3, 9, 18]	Ratio of fibre volume to total composite volume	Weighing, density	Controls mechanical properties
Fibre Distribution Uniformity [10, 49]	Variation of fibre content across tape cross-section	Optical microscopy, image analysis	Consistent performance
Void Content [9, 48]	Voids within composite	Optical microscopy, μCT	Reduces strength and durability
Fibre Alignment / Misalignment [10, 48]	Angular deviation from principal direction	μCT, von Mises distribution	Affects load transfer and stiffness
Fibre Neighbourhood Metrics [10]	Clustering / spatial arrangement of fibres	SRCT, topology analysis	Insight into microstructure
Tortuosity [9, 10]	Complexity of fibre path	Rare metric (proposed)	Local variability
Intersection Density [9, 10]	Number of fibre contacts	Microscopy, network analysis	Correlates with tensile performance

This study, therefore, uses FVF as a quantitative metric for tape quality, while acknowledging that more advanced microstructural descriptors will be required in future work to fully resolve slurry-to-microstructure relationships.

2.8 Identified gaps and positioning of the present work

The state of the art provides extensive insight into the mechanisms of thermoplastic composite impregnation and the physics of roller-based coating. Analytical and numerical models describe liquid entrainment, pressure build-up, and film formation in nip-roller configurations, while slurry-based thermoplastic impregnation has been widely studied from formulation and suspension-stability perspectives. However, considering these bodies of work together reveals several limitations regarding continuous slurry-based impregnation of carbon fibre tapes.

First, existing roller-coating models are developed mainly for continuous, impermeable substrates and homogeneous liquids. They do not account for the porous and deformable nature of fibre tows or for particle-laden slurry behaviour. As a result, current models do not predict how slurry transfers into or distributes within a fibre tow, limiting their use in process design for slurry-based tape impregnation.

Second, most experimental studies on slurry-based thermoplastic impregnation focus on slurry formulation, stability, and final laminate properties, while the influence of machine setpoints and operating conditions during continuous impregnation remains insufficiently characterised. In particular, limited experimental evidence links process parameters to measurable deposition behaviour and tape-quality indicators under realistic, pilot-scale manufacturing conditions.

Third, although both kiss-roller and nip-roller configurations are used for slurry transfer in continuous processing, no systematic comparison applies a common experimental basis to both. This makes it difficult to distinguish effects intrinsic to the slurry formulation from those arising from the impregnation configuration itself.

These gaps limit the ability to interpret experimental results across different impregnation routes and hinder the identification of robust process trends for slurry-based thermoplastic tape manufacturing. The present thesis addresses these limitations by adopting a process-oriented experimental approach to slurry-based impregnation of ultrathin UD carbon/PEEK tapes. Rather than developing fully predictive models or optimising slurry formulations, the work focuses on clarifying how process parameters and slurry state influence deposition behaviour and tape quality, and how these relationships differ between kiss-roller and nip-roller impregnation.

Accordingly, the central research question of this thesis is:

"How do process parameters and slurry state translate into deposition behaviour and tape quality in slurry-based impregnation, and how do these relationships differ between kiss-roller and nip-roller configurations?"

Chapter 3

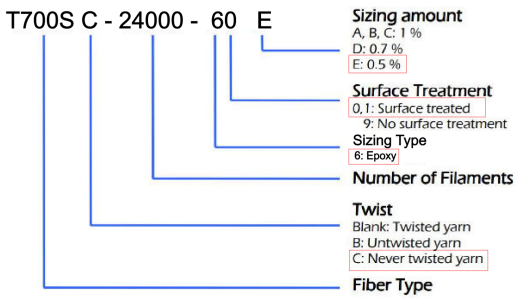
Materials & equipment

This chapter presents the equipment used for this study and describes the tools and machines used.

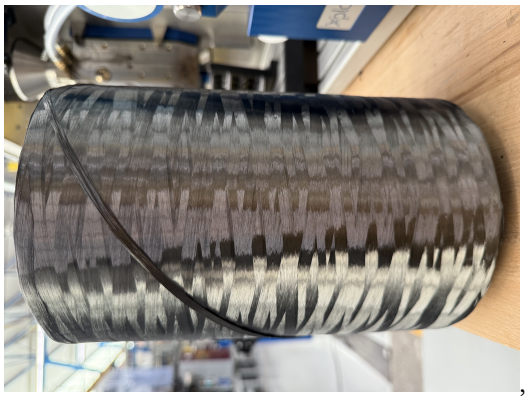
3.1 Materials

Reinforcement

The reinforcement used in this work is a Toray T700SC carbon fibre, as shown in Figure 3.1b, supplied in 24k tow form (T700SC-24000-60E) with a density of 1.8 [g/cm³] and a linear weight of 1.65 [g/m]. The fibre is coated with 60E sizing, which the manufacturer specifies as epoxy-compatible. (Fig.3.1a). The tow is fed directly from the bobbin without pre-spreading or pre-treatment. The technical datasheet is available in Appendix A.1



(a) Schematic of the Toray T700SC carbon fibre tow.



(b) Bobbin of Toray T700SC carbon fibre tow used during manufacturing.

Figure 3.1: Toray T700SC carbon fibre tow: schematic representation and bobbin picture.

Matrix

The matrix material is PEEK powder, grade VICOTE™ 704 (Victrex), from the VICOTE™ 700 Series. PEEK is a high-performance polymer recognised for its strength and chemical resistance. This off-white, semi-crystalline powder has a median particle size of approximately 10 µm and was developed for high-temperature coating applications. The powder is used as received, without drying or sieving. It exhibits typical PEEK properties, including a continuous use temperature of about 260 °C, excellent wear resistance, chemical stability, and a density of 1.32 g/cm³. This material has a glass transition temperature of 143°C and a melting temperature of 343°C. In the slurry formulations for this study, the PEEK powder content ranges from 25 to 33 wt% to assess how polymer concentration affects rheological behaviour and composite properties. This range was chosen based on preliminary experiments that identified optimal flowability and tape properties under the examined processing conditions. The technical datasheet is available in Appendix A.2

Thickener

Polyethylene glycol (PEG) (Sigma-Aldrich, P6667, PEG-10000) served as a water-soluble thickener to stabilise the PEEK dispersion and adjust its rheology. PEG, with a density of 1.07 [g/cm³], was used at concentrations up to 10 wt%. This concentration was avoided, as preliminary trials at 10 wt% PEG led to ignition ignitition point at 305°C) of the tape on the heated roller units. The technical datasheet is available in Appendix A.3

Food-grade XG was evaluated as an alternative rheology modifier, primarily because it is non-toxic, biodegradable, and widely accepted in food and pharmaceutical applications. In contrast to PEG, xanthan gum is less likely to cause thermal ignition and is effective at much lower concentrations. Concentrations up to 0.1 [wt%] (approximately 1 g/L) were used. This range was chosen based on [8]. No datasheet is available as this product was purchased in a food shop.

Surfactant

Triton X-100 (Sigma-Aldrich, X100), a non-ionic surfactant, was added in small quantities (approximately 0.5% for 33% PEEK powder calculated on the total weight of the solution) to promote wetting and dispersion of PEEK particles. Its hydrophilic polyethylene oxide segment and hydrophobic aromatic tail enable effective adsorption at solid–liquid interfaces. Due to its high aquatic toxicity (H400 / H410), it was handled with proper ventilation and waste collection procedures. The technical datasheet is available in Appendix A.3

The stabilisation mechanism of the suspension is shown in Figure 3.2. Triton X-100 wets PEEK particles more effectively and is mainly adsorbed onto the surface of PEEK powder, helping to disperse it in water. However, because Triton X-100 has a short molecular chain, the PEEK powder will settle and become compact over time. PEG has a longer molecular chain and is adsorbed onto the surface of PEEK in smaller amounts. However, PEG can form a three-dimensional network structure in the suspension, which improves stability. The combined effect of Triton X-100 and PEG provides stronger steric hindrance. After the PEEK powder settles, there is no obvious compaction. [30]

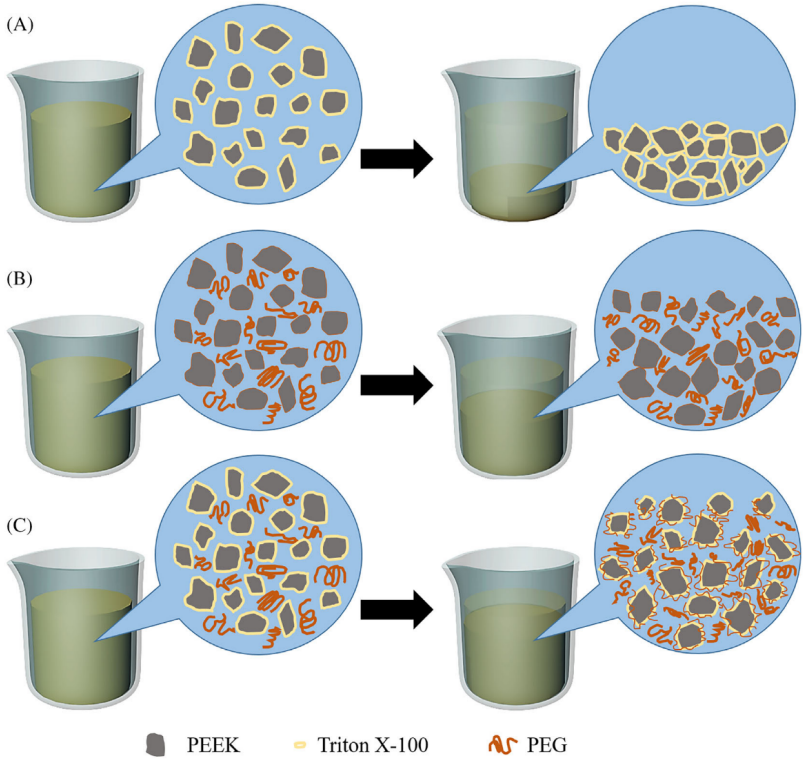


Figure 3.2: Schematic of the stabilisation mechanism of polyether ether ketone dispersion with different surfactants. (A) TX;(B) PEG; and (C) CS1, and CS2 (compound solution). [30]

3.2 Equipment

This section presents the equipment used for this study and describes the tools and machines used. The pilot-scale impregnation line used in this study is part of the Delft TapeLab, an open research facility at TU Delft focused on the development, processing, and characterisation of unidirectional thermoplastic composite tapes. The TapeLab offers a flexible experimental environment for controlled manufacturing trials, direct access to process parameters, and in-line observations not typically available on industrial production lines. It supports small-batch tape production, systematic parameter studies, and detailed process–structure investigations in close collaboration with academic and industrial partners.

3.2.1 Tape line

The tape line presented in Figure 3.3 is the primary equipment used to manufacture the tape. This unique modular pilot line was developed and built by Van Wees (Tilburg, Netherlands).

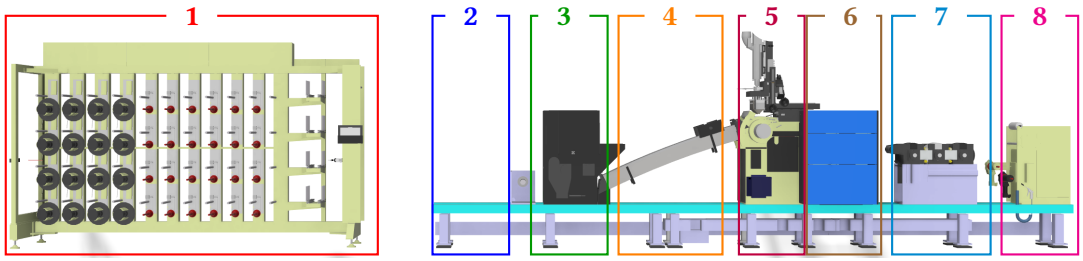


Figure 3.3: Overview of the full tape-line equipment used in this study. The eight main modules are highlighted and numbered from (1) to (8). This configuration is installed as a Nip-roller.

The tape line includes eight consecutive functional modules, as shown in Figure 3.3. The fibre creel (1) holds and guides individual tows into the process. The dry spreading unit (2) opens the tow to improve impregnation efficiency (module 2 is not shown in the image and will be presented in 3.2.1). The impregnation system (3) applies the PEEK–powder–based slurry to the fibres, and the drying bridge (4) removes the water before melting. The heating and consolidation units (5) melt and compact the material. The double-belt calender system (6) ensures uniform thickness and consolidation. The pulling unit (7) controls line speed, and the winding module (8) collects the finished tape.

Two different methods are implemented to impregnate the fibre with the slurry. The first one is the Kiss-roller configuration, shown in Figure 3.4 and the second one is the Nip-roller configuration, shown in Figure 3.7.

In the Kiss-roller configuration (Fig. 3.4), the fibre tow contacts a slurry-coated rotating roller. This configuration transfers a polymer particles from slurry onto the fibres through capilarity action before they enter the drying, heating and consolidation sections of the tape line. The only differences between Nip-roller and Kiss-roller configurations are module 3 and the slope of module 4. The rest remains unchanged.

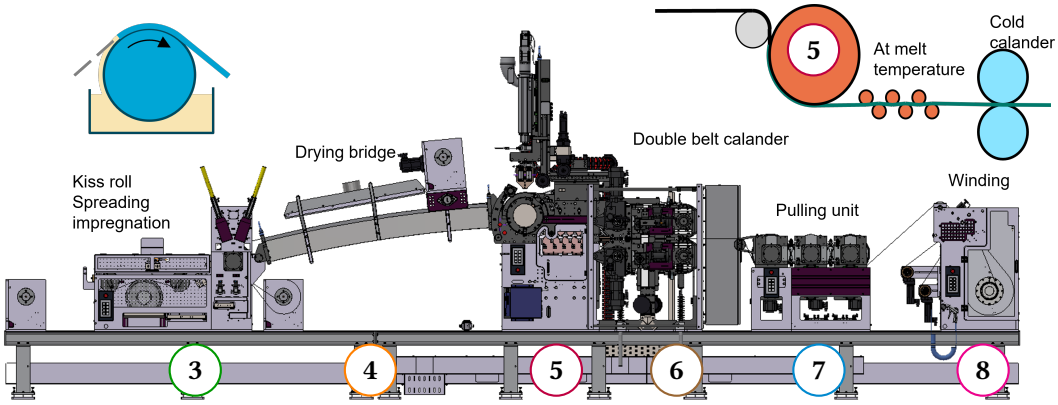


Figure 3.4: Overview of the tape line in the Kiss-roller impregnation configuration. The corresponding process schematic is shown at the top left. The creel (1) and dry-spreading unit (2) are not included.

To complement the line overview, the Kiss-roller impregnation module (Module 3) is described in detail below.

The Kiss-roller impregnation module (Figure 3.5, 3.6) applies a uniform, controlled film of PEEK-based slurry to the carbon fibre tow before consolidation. A rotating roller (C), partially immersed in the slurry tray (D), transfers a thin liquid film from the tray (D) to the fibre tow by direct contact. To refill the tray (D), a funnel (B) is connected to a tube as shown in 3.6. The slurry amount depends on the roller's speed, surface properties and the suspension's viscosity. Dry spreading units (A) placed before and after the impregnation zone maintain tow spreading and alignment. A scraper (E) removes excess slurry from the impregnated fibre tows before it exits the module.

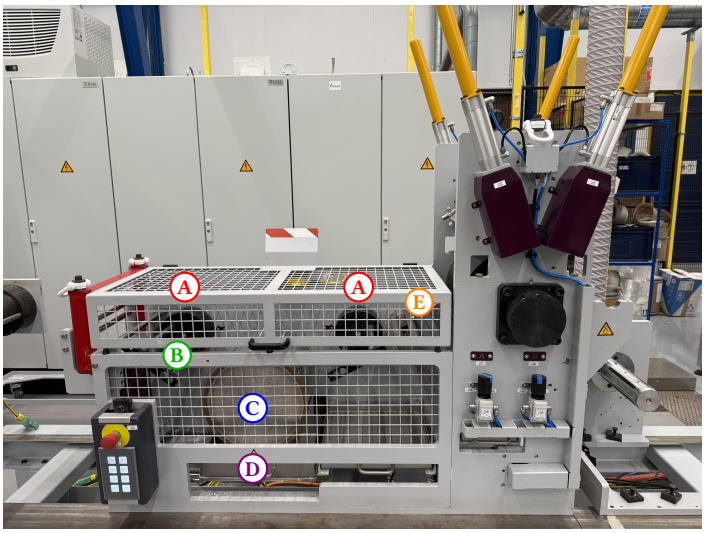
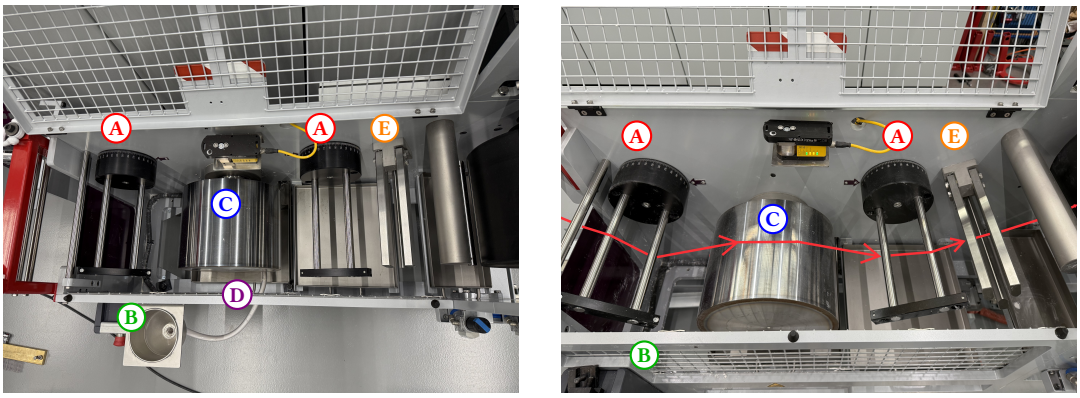


Figure 3.5: Kiss-roller impregnation module with annotated zones (A–E).



(a) Open configuration. **(b)** Alternative view with fibre trajectory.

Figure 3.6: Open and alternative views of the Kiss-roller impregnation module with annotated zones (A–E).

In the Nip-roller configuration (Figure 3.7), the fibre and slurry are compressed between two counter-rotating rollers. This increases the local impregnation pressure into the tow before it enters the drying, heating, and consolidation sections of the tape line.

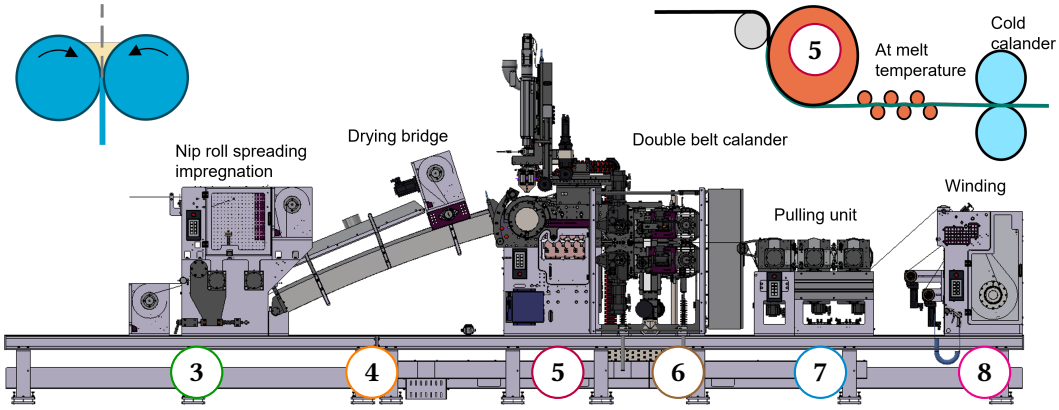


Figure 3.7: Overview of the tape line in the Nip-roller impregnation configuration. The corresponding process schematic is shown at the top left. The creel (1) and dry-spreading unit (2) are not included.

The Nip-roller impregnation module (Figure 3.8 and 3.9) applies slurry by forcing the fibre tow through a converging contact zone formed by two counter-rotating rolls (C). Slurry is continuously supplied to the Nip region through a dedicated refill line (B). The tow is impregnated by the combined effects of roll contact and constrained flow within the nip. A polyurethane (PU) carrier paper from the unwinder (F) is fed under the fibre tow and passes through the nip in contact with the left-hand roll only. It remains under the slurry-coated tape through the drying section, providing temporary support before being removed upstream of consolidation. A dry spreading/return bar (A) guides and stabilises the tow trajectory upstream of the nip, while a scraper (E) removes excess slurry after impregnation.

The key adjustable parameter of the Nip-roller module is the Nip gap, which directly controls mechanical compaction and slurry film thickness. The gap is set mechanically and monitored with a dial indicator (D) to enable reproducible positioning and systematic comparison between trials.

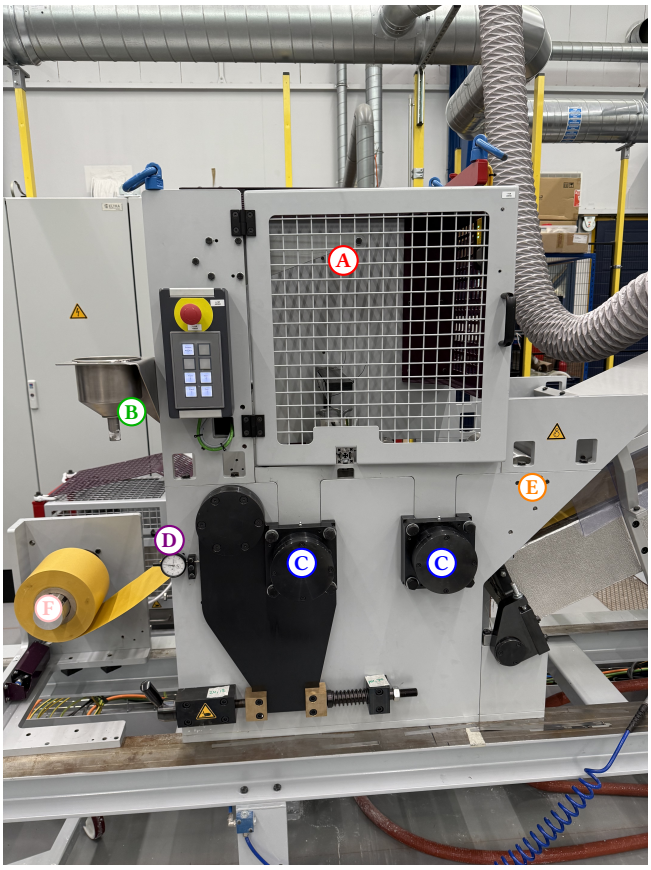
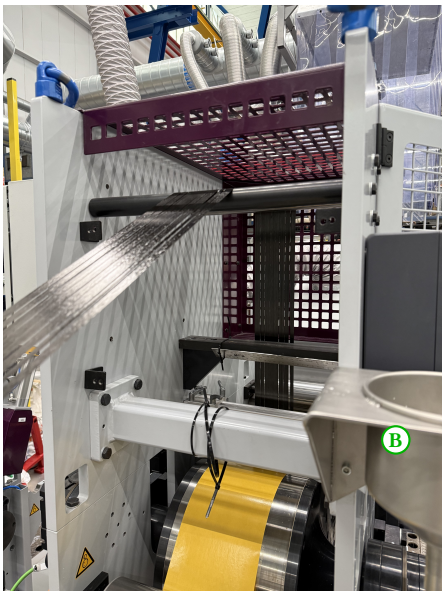
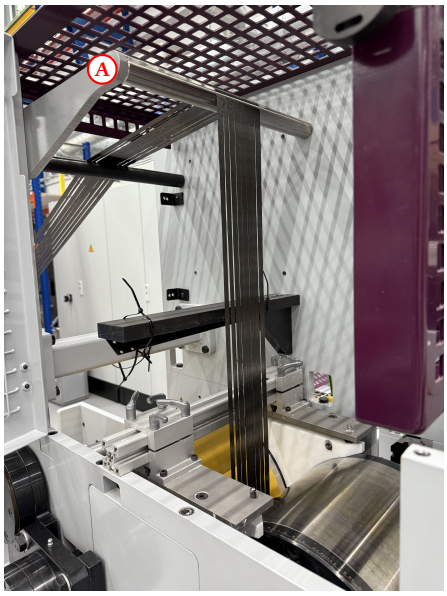


Figure 3.8: Nip-roller impregnation module with annotated zones (A–F).



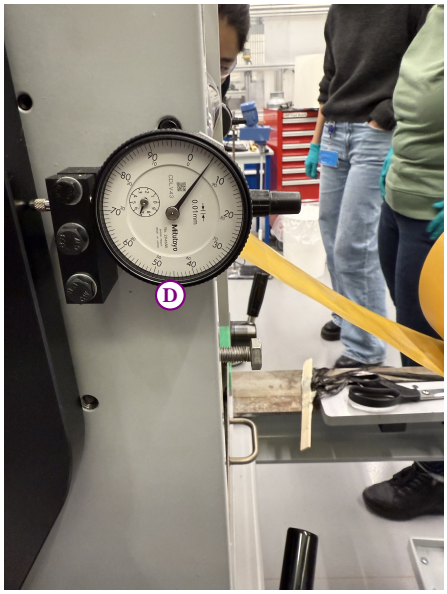
(a) Open configuration.



(b) Fibre trajectory view.



(c) Nip region close-up.



(d) Nip gap dial indicator.

Figure 3.9: Nip-roller impregnation module with annotated zones (A–E).

Physically, the Kiss-roller and Nip-roller configurations correspond to two distinct fibre–slurry contact regimes. The Kiss-roller operates under low mechanical load and relies on slurry film formation, wetting, and contact time at the fibre surface. In contrast, the Nip-roller introduces a constrained flow region with mechanical compaction, where impregnation is governed by nip gap, pressure, and forced slurry transport through the tow. These differences define distinct impregnation regimes and motivate separate experimental campaigns and parameter sets, as described in Chapter 4.3.

Creel (1)

The creel (Figure 3.10) holds and guides the fibre bobbins at the tape line entrance, applying controlled resistance to establish initial line tension. This tension stabilises the tow during unwinding, ensures uniform fibre spreading and enhances contact conditions for efficient slurry impregnation.

The red and orange arrows indicate the pulling direction, consisting of 2 outputs, each with 4 tows. The marker (A) corresponds to the position of the pressure sensor used to monitor the pretension applied to the fibre tow.

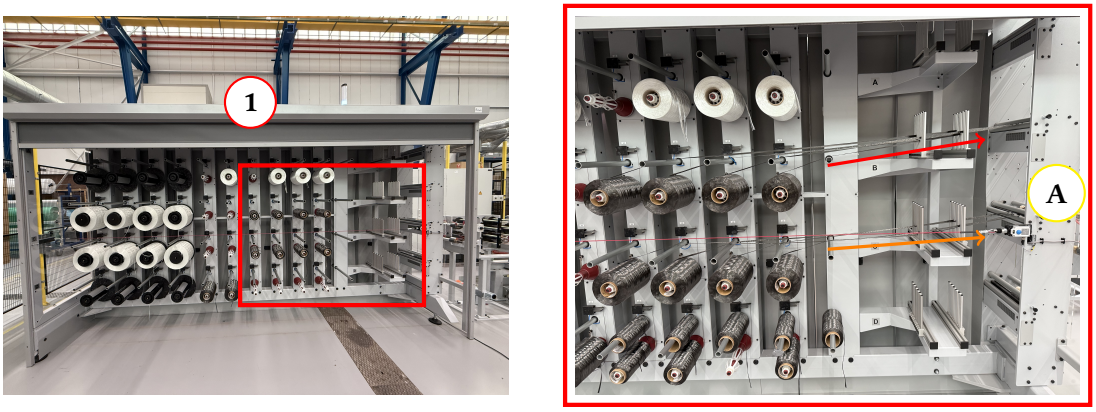


Figure 3.10: Left: creel holds carbon and glass fibres, showing the region selected for the zoom. Right: zoomed view of the fibre pulling section.

Tension sensor (A)

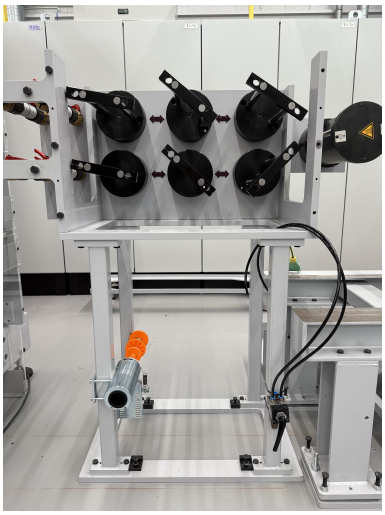
The white tension sensor (Figure 3.11) is mounted before the impregnation module to monitor the pulling load and regulate line tension, which directly affects tow spreading and impregnation efficiency.



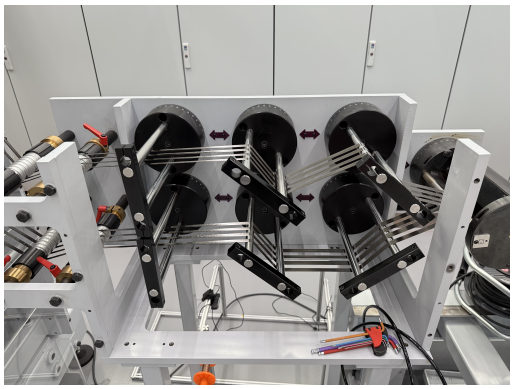
Figure 3.11: Tension sensor used to monitor the creel tension.

Dry bar spreading unit (2)

The dry bar spreading unit (Figure 3.12) separates the tow and enhances mechanical fibre distribution. This step is critical for achieving tape with the specified width and consistent thickness.



(a) Full overview of dry spreading module.



(b) Close view of the module with loaded fibres.

Figure 3.12: Dry spreading unit used to open the fibre tow before impregnation.

Figure 3.13 demonstrates that spreading causes the tows to become wider and thinner compared to the original tow on the spool.

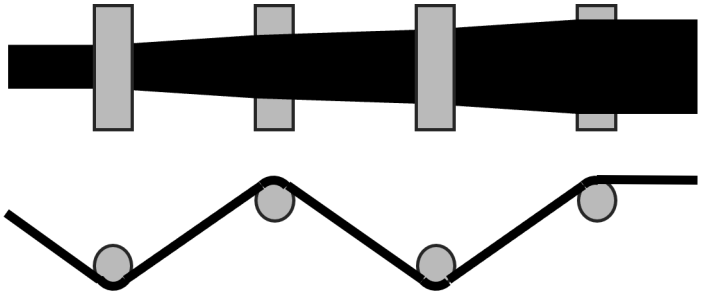
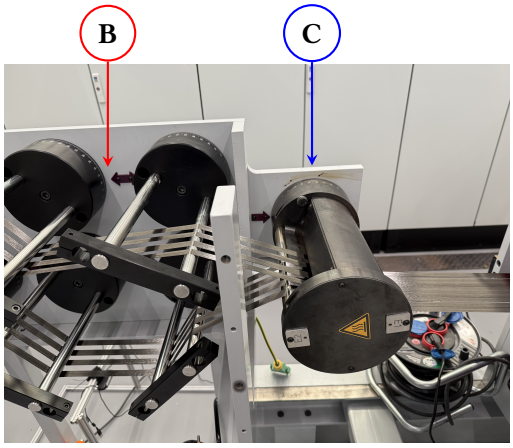


Figure 3.13: Illustration of the bar-spreading effect on a single tow.

The module consists of two levels, each containing two positioning units (3.14a). Each level also includes three pairs of spreader bars with a diameter of 15mm (3.12b) on bases that can be adjusted individually, with angle indicators for precise control (3.14b (B)). Increasing the wrap angle around the spreader bar enhances tow spreading. It also raises fibre tension and friction at the bars, which can affect spreading efficiency [38]. After the spreader bar pairs, a final double-bar device (3.14b (C)) combines fibres from the top and bottom levels. This part can also be heated, introducing an additional adjustable process parameter. Heating softens the fibre sizing, which can promote tow spreading and tow mixing [38].



(a) Overview of the two dry spreading entries.



(b) Annotated detailed view of the spreading and heating area.

Figure 3.14: Close-up views of the dry spreading module and adjustable features.

Drying bridge (4)

The drying bridge (Fig.3.15), after the impregnation unit, removes water from the slurry through convective drying. The temperature of the deck is set at 120°C, while forced ventilation promotes moisture removal and stabilises the deposited matrix prior to consolidation.



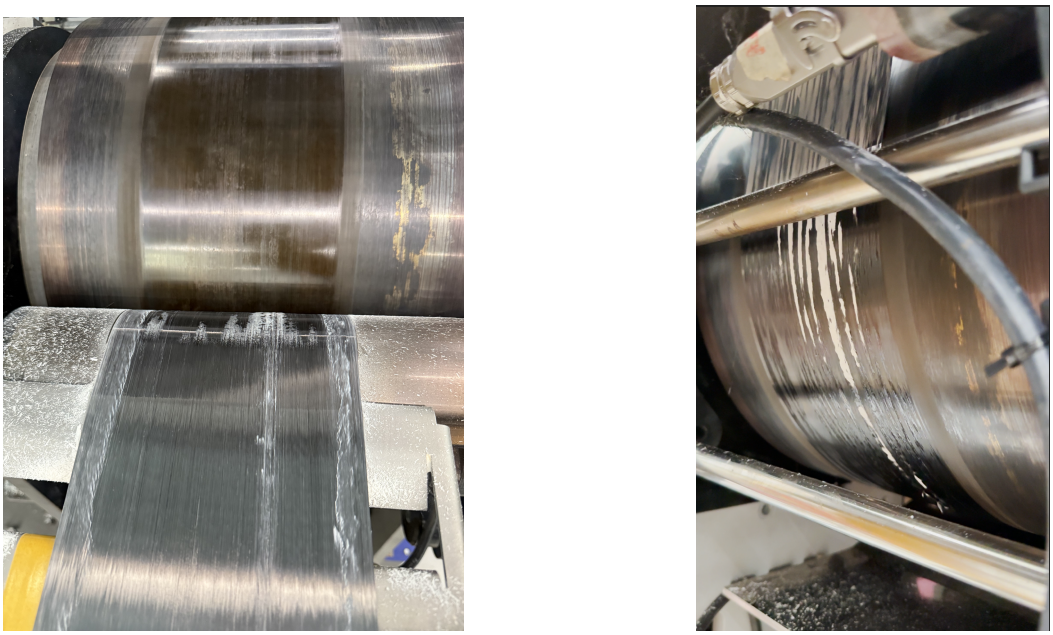
Figure 3.15: Drying bridge unit. The red arrow shows the manufacturing direction, while the green arrow shows the forced ventilation exit

Heat unit (5)

The main heated roller (Fig. 3.16) is temperature-controlled and runs at the line speed. In this work, it was set to 420 °C and 450 °C. However, the surface temperature ranges from 370°C at the roller's center to 350°C at its edges. After the drying bridge, the thermoplastic matrix melts upon contact with the roll (Fig. 3.17), promoting matrix flow and tape consolidation. The assembly above the roller is a melt-processing extruder for hot-melt operation (pellet feeding) and was not used in this study.



Figure 3.16: Main heat unit.

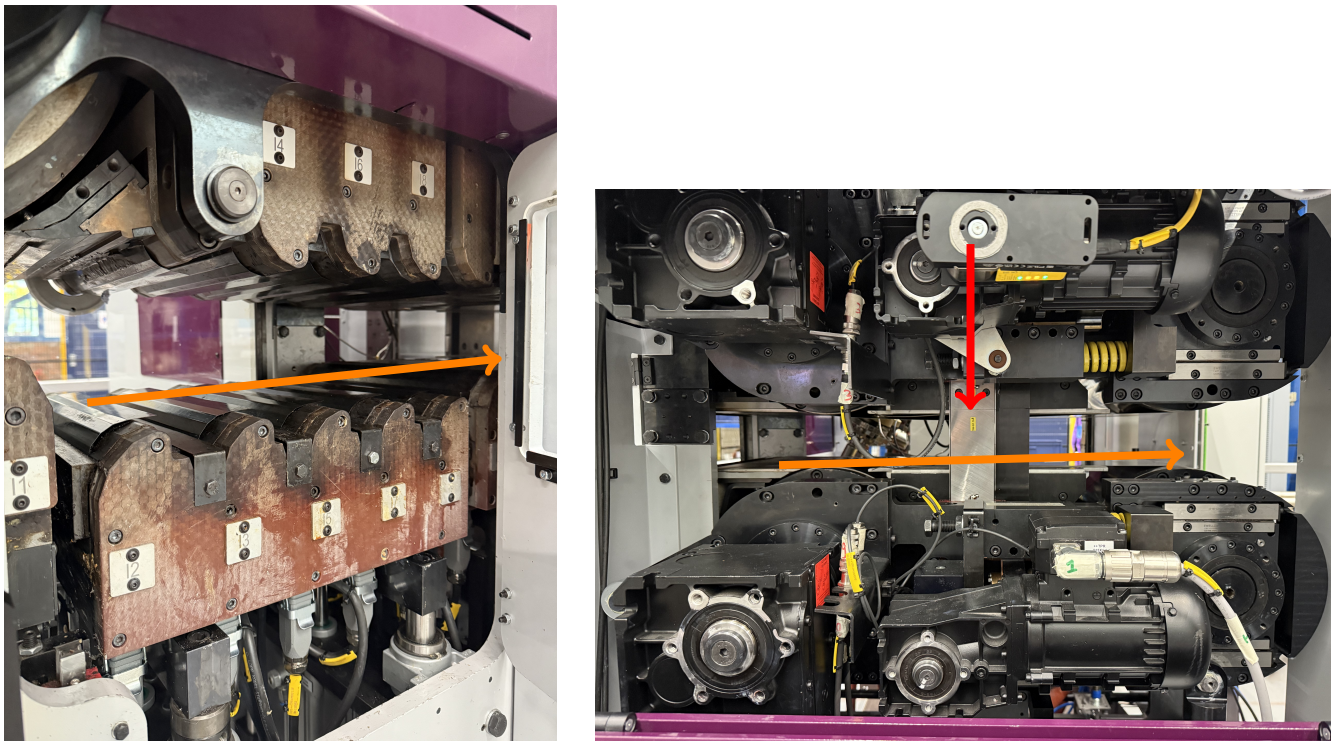


(a) **(b)**

Figure 3.17: Post spreading unit (a) and calender unit (b)

Post spreading and double belt calender(6)

The post spreading (Fig. 3.18(a)) is heated to the same set temperature as the heat unit. This temperature is more stable than the heat unit. Metal blades press onto the fibres to spread the tape when the matrix is molten. The calendering unit is shown in Figure 3.18(b), and the temperature is set to 120°C. The tape is pressed between two belts, forcing the thermoplastic and fibres together. Figure 3.19 illustrates the double-belt principle: orange arrows show the manufacturing direction, and the red arrow shows the direction of the closing force.



(a) Heated post-spreading **(b)** Double-belt calender

Figure 3.18: Post spreading (a) and calendering unit (b)

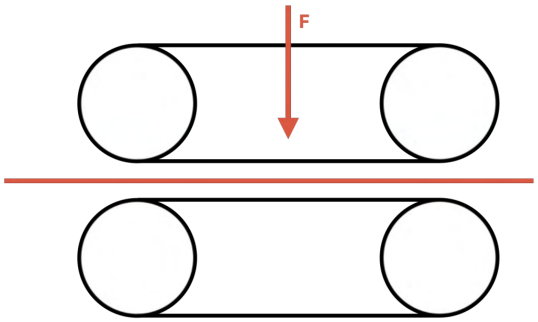


Figure 3.19: Illustration of the operating principle of a calendering unit. Red arrows indicate the manufacturing direction, and the second arrow shows the direction of calender pressure.

Pulling unit (7)

The unit 3.20 controls line speed. The tape passes through three driven rolls, which, through capstan friction, set the pulling speed and ensure stable transport along the process.

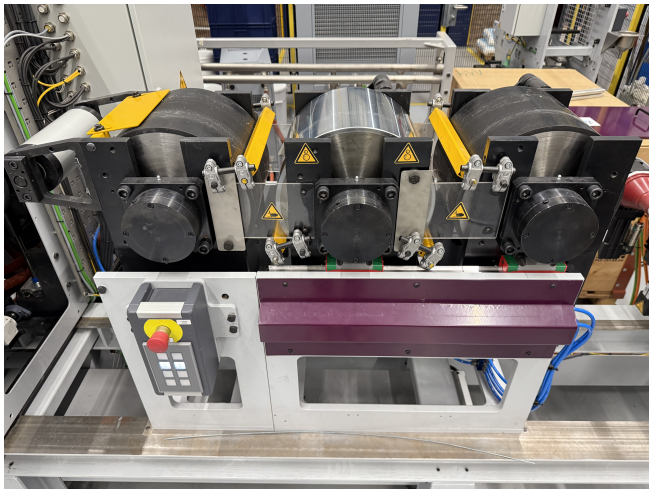
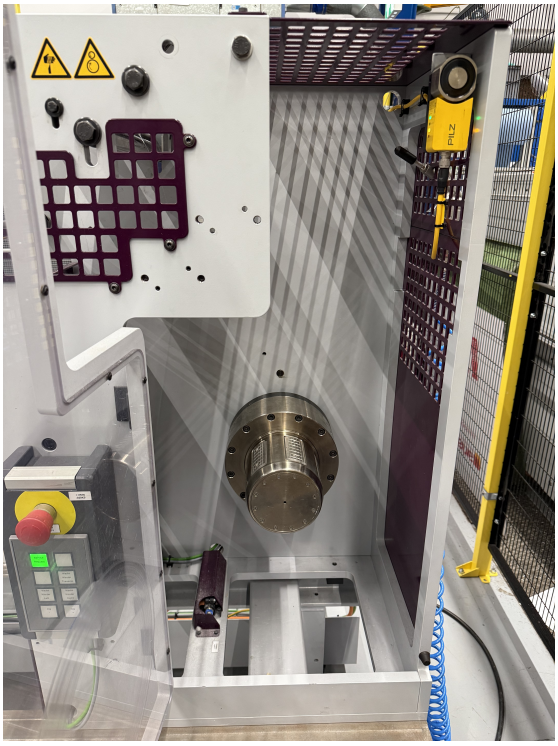


Figure 3.20: Pulling unit

Winding module (8)

The module 3.21 (a) winds the tape at the end of the line. It also includes a slitting function (b) to cut the tape into narrower strips for the desired final width if needed.



(a)



(b)

Figure 3.21: Post spreading unit (a) and calender unit (b)

3.2.2 Measuring devices

Rheometer

Viscosity measurements were performed using a TA Instruments Hybrid Discovery rheometer (model HR-3). The setup shown below (Fig. 3.22) uses a concentric-cylinder geometry, also known as Couette flow, to measure slurry properties. The bob diameter is 28 mm and the cup diameter is 30.36 mm, creating a 1.18 mm gap.

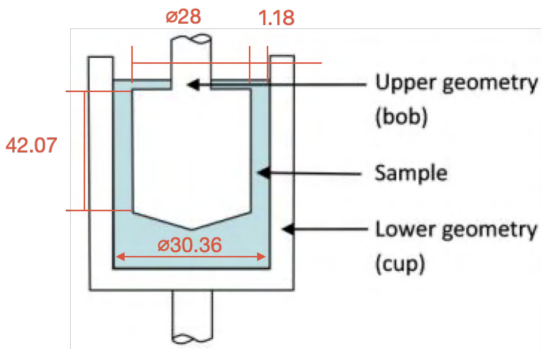


Figure 3.22: Rheometer geometry sketch, dimensions in [mm] [38].

Particles Size Analyser

This study used the Mastersizer 3000 particle size analyser from Malvern Panalytical. The analyser works with the Hydro SM module to measure particles in water suspension.

With a measurement range between 0.01 and 3500 µm, the mastersizer uses a laser diffraction systems determine particle size from the resulting light-scattering pattern as a collimated laser beam passes through the sample, as shown in Figure 3.23. Large particles scatter with high intensity at narrow angles relative to the incident beam, while smaller particles generate a weaker signal that extends to wider angles. Laser diffraction analyzers calculate the particle-size distribution of the sample using the measured angular dependence of the scattered light based on an appropriate theory of light scattering, generally Mie theory [50].

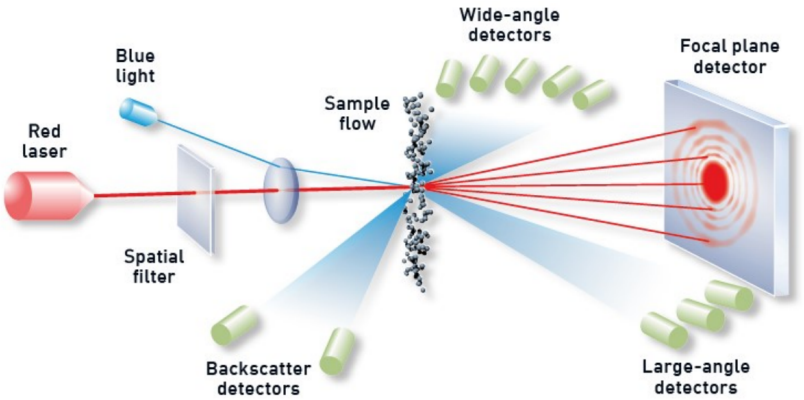


Figure 3.23: Illustration showing the principle behind a laser diffraction measurement with diffracted light from dispersed particles picked up by optimally positioned detectors [50]

Microscopes

Optical imaging was performed using a Keyence VK-X1000 confocal laser scanning microscope. The system allows high-resolution surface and microstructural observation through interchangeable objective lenses with nominal magnifications of 5×, 10×, 20×, and 50×.

All images in this work were acquired using the 20× objective, which balances field of view and spatial resolution for comparative tape-quality analysis.

Scales

Mass measurements were performed using a Mettler Toledo laboratory balance with a resolution of 0.1 mg. The balance was used both to weigh slurry samples during composition analysis and to measure tape masses required for fibre volume fraction determination.

Oven and Furnace

Slurry samples were dried using a Heraeus UT 6200 laboratory oven to evaporate water and achieve complete drying. Drying was performed at controlled temperature to avoid boiling, splashing, or loss of solid material.

Thermal degradation of organic additives was carried out in a Nabertherm muffle furnace to burn off the Triton X-100 surfactant present in the dried slurry, enabling isolation of the PEEK residue for gravimetric mass-fraction determination.

Chapter 4

Methodology

This chapter follows a campaign-based experimental strategy to investigate slurry-based impregnation under controlled, reproducible conditions. Instead of varying all parameters at once, trials were grouped into successive campaigns, each designed to isolate the influence of a limited set of process parameters while keeping other conditions constant. This approach allows systematic comparison across trials and helps identify trends versus campaign-specific variability.

4.1 Overview of Experimental Trials

Tables 4.1 and 4.3 provide an overview of the experimental trials performed for the Kiss-roller and Nip-roller configurations, respectively. For each configuration, trials are organised by campaign, with the corresponding processing parameters reported to document the experimental space explored in this study. A trial lasts about 10 minutes for the Kiss-roller and 5 minutes for the Nip-roller. Each trial start was marked to measure its duration. The test plans used during laboratory trials are available in Appendix B.1.

For the Kiss-roller configuration (Tab. 4.1), the experimental campaigns were designed to investigate the influence of individual process parameters on slurry deposition and final tape quality. Depending on the campaign, line speed, fibre tension, impregnation roller temperature, and calendar pressure were varied. Each campaign, therefore, focuses on a distinct subset of parameters, enabling their effects to be assessed in relative isolation.

Table 4.1: Kiss-roller trials and processing parameters (performed trials only).

Campaign	Trial	Fiber tension (cN)	Line speed (m/min)	Impreg. roller temperature (°C)	Calendar pressure (N)
1	T16	500	1.8	420	500
1	T17	500	3.0	420	500
1	T18	500	2.4	420	500
1	T20	500	5.0	420	500
1	T21	500	4.2	420	500
2	T22	700	3.0	420	500
2	T23	250	3.0	420	500
2	T24	1000	3.0	420	500
2	T25	850	3.0	420	500
2	T26	1300	3.0	420	500
2	T28	500	3.0	420	500
2	T29	700	3.6	420	500
2	T31	1000	3.6	420	500
2	T35	500	3.6	420	500
2	T37	700	3.6	420	1000
2	T39	700	3.6	420	2000
2	T41	700	3.6	420	3000
3	T42	700	3.6	450	500
3	T43	700	3.6	450	1000
3	T46	700	3.6	450	2500
3	T47	700	3.6	450	3000

For the Nip-roller configuration (Tab. 4.3), the same campaign-based approach was adopted, with trials organised to vary one parameter at a time while maintaining the others constant. In this case, the impregnation temperature was kept fixed, and the experimental space focused on line speed, fibre tension, and the Nip gap, which introduces an additional mechanical control parameter governing compaction and slurry flow in the Nip region.

Table 4.3: Nip-roller trials and processing parameters (performed trials only).

Campaign	Trial	Fiber tension (cN)	Line speed (m/min)	Impreg. roller temperature (°C)	Calendar pressure (N)	Gap (tenth mm)
1	T01	150	3.6	420	1500	22.5
1	T02	0	3.6	420	1500	22.5
2	T02	0	3.6	420	1500	27
2	T02	0	3.6	420	1500	30
2	T03	200	3.6	420	1500	30
2	T05	250	3.6	420	1500	30
2	T05	250	3.6	420	1500	35
2	T07	0	3.0	420	1500	35
2	T09	0	3.6	420	1500	35
3	T06	0	5.0	420	1500	35
3	T06	0	5.0	420	1500	45
3	T06	0	5.0	420	1500	55
3	T08	0	4.2	420	1500	45
3	T08	0	4.2	420	1500	35
3	T09	0	3.6	420	1500	35
3	T12	0	3.6	420	1500	35

The experimental procedures, measurement protocols, and characterisation methods used in these trials are described in the following sections.

4.2 Slurry experiments

4.2.1 Slurry preparation

PEEK powder is hydrophobic and does not disperse easily in water, leading to particle agglomeration. To improve wetting and achieve uniform dispersion, Triton X-100 is added in an amount sufficient to coat the particles and prevent aggregation. If too little surfactant is used, clumping or a persistent foam layer may form at the slurry surface, even with vigorous stirring. If too much is added, it generates foam and can modify the surface tension. These defects can disrupt slurry flow and cause irregularities along the tapeline during impregnation.

The required amounts of water, PEEK powder, and TX are determined using the formulation sheet developed during a previous study with this material [38]. All components are combined in a plastic container and mixed with a mechanical stirrer. The container is covered with a plastic cover during mixing to minimise water evaporation.

4.2.2 Rheology: planned viscosity mapping and study limitations

Rheological characterisation was defined as a central part of the experimental methodology to establish a quantitative viscosity window for slurry-based impregnation and systematically assess the influence of formulation parameters: PEEK, PEG, and XG. The approach aimed to reproduce, with reduced PEG content, the functional viscosity levels previously identified for Kiss-roller tape manufacturing in earlier work. It also sought to construct a viscosity–shear-rate map over a defined formulation space to support the development and comparison of nip-roller impregnation conditions.

The rheological mapping campaign was limited by the failure of a critical rheometer component, which prevented completion of the planned measurement matrix. As a result, only a restricted set of preliminary measurements was performed, which was insufficient to establish a comprehensive viscosity database covering the full range of manufacturing conditions in this study.

Consequently, the rheological framework adopted in this thesis is based primarily on the laboratory's experimental baseline, including viscosity ranges previously shown to be effective for Kiss-roller impregnation [38], complemented by limited rheometer measurements acquired before instrument failure. The complete experimental protocol originally designed for rheological mapping, together with the associated formulation space (PEEK/PEG/XG ranges) and targeted shear-rate domains, is provided in Appendix C.1.

4.2.3 Slurry PEEK weight fraction monitoring during processing

Slurry Sampling Methodology

– slurry sampling for the kiss-roller

To monitor changes in slurry composition during manufacturing, samples are collected from the Kiss-roller tray every twenty minutes. This approach ensures the samples reflect the environment the fibre encounters during roller pick-up, not the reservoir composition.

Samples are drawn with a syringe (Fig. 4.2a), keeping a consistent horizontal position and immersion depth to minimise local composition variations. Each 10 ml sample is immediately transferred to a sealed, labeled plastic vial (Fig. 4.2b).



Figure 4.1: Sampling syringe on the bottom and plastic vial. on the top



(a) Sampling with syringe directly in the tray of the Kiss-roller.



(b) Slurry sample after collection.

Figure 4.2: Slurry sampling procedure used during manufacturing.

– slurry sampling for Nip-roller

To assess how slurry composition evolves locally during nip-roller processing, slurry samples were collected at defined positions relative to the Nip and analysed for PEEK weight fraction. The *top* sample was taken above the Nip at a fixed and constant slurry height. The *bot* sample was taken at the bottom of the nip at a fixed and constant sampling height, at the end of a run when the nip was nearly empty, and eddies were visually observed. Some trials also include a *top_5min* sample, collected at the same top location 5 minutes after the initial top sample while maintaining the slurry level at the same top height. All trials T1–T7 used the same slurry formulation containing 28wt% of PEEK and 0.5g/l of xanthan gum.

Two measurement approaches were performed. In trials T1–T4, the objective was to compare the initial *top* composition to the *bot* composition reached as the nip approaches a starved condition, at fixed line speed and varying gap settings. The figure 4.3 shows the sampled positions. In trials T5–T7 at fixed gap, the objective was to monitor short-term evolution at the top location (*top* vs *top_5min*) and to document the *bot* composition under different line-speed conditions. Due to practical constraints (refill and run-out), not all planned sampling points were obtained (no *top_5min* for T4; no *top_5min* for T7; and T6 includes a *bot* sample under non-identical run conditions compared with the fully drained and cleaned Nip-roller T1–T4 runs). As a result, comparisons are restricted to the most directly comparable subsets within this dataset. The notation T here does not represent the trials used during campaigns for tape manufacturing. It is a unique notation for this test. For this reason, the term “sample” will be used in the results to present this part. An explicative table is presented in section 5.2.1 (Tab. 5.15).

This method was used only when measuring the PEEK weight fraction. During tape manufacturing, the slurry level was maintained at the top by continuously adding slurry.

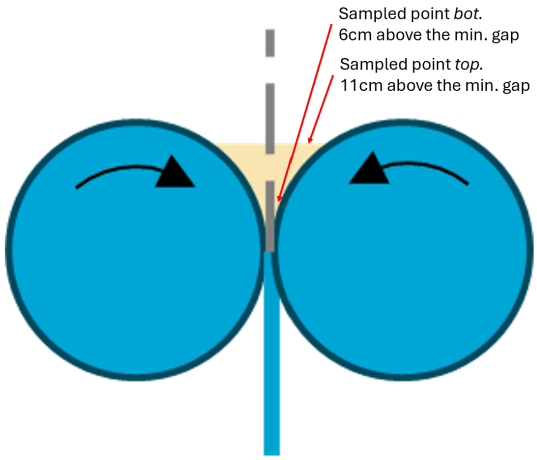


Figure 4.3: Illustration of the position where the top and bottom samples were taken. The distance in centimetres is measured from where the gap is minimal (gap size).

Sample Traceability and Identification

Each sample is labelled with the date, exact sampling time, and batch number to enable accurate cross-referencing with manufacturing parameters and prevent ambiguity during processing (Fig. 4.5).

PEEK Content Analysis Methodology (% by mass)

PEEK mass fraction was quantified using a gravimetric drying and calcination method adapted from Mitsuda et al [51].

Empty glass vials are weighed, then filled with slurry and weighed again to minimise water evaporation before thermal treatment. Samples (Fig. 4.5 are placed in a laboratory oven for at least twelve hours at 90 °C, a temperature selected to prevent boiling and powder ejection.

After oven drying, vials are weighed immediately to limit humidity reabsorption, although PEEK absorbs little moisture. Vials are then placed in a furnace at 300 °C for fifteen minutes, following Mitsuda's method, to degrade the Triton X100 additive and isolate the PEEK mass (Fig. 4.4). A final weighing determines the masses of water, additive, and PEEK, enabling calculation of the PEEK mass fraction.

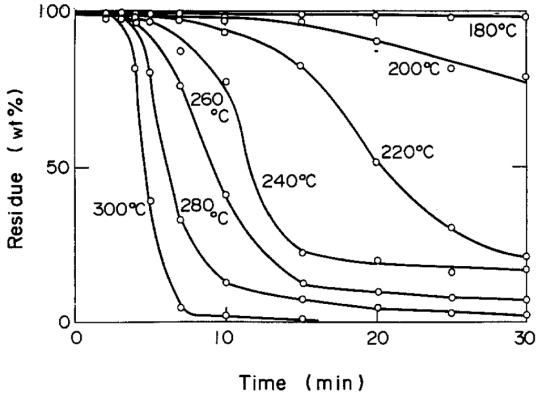


Figure 4.4: Time dependence of TX100 residue in air. [51]

Marker-based labels on vials will disappear during high-temperature processing. Before placing samples in the furnace, we photographed their positions or use heat-resistant labels for identification.



Figure 4.5: Heat-resistant glass vial used for slurry drying and additive degradation. Marker-based labelling is used to identify samples before furnace treatment.

Uncertainty estimation

Uncertainty in the gravimetric determination of the slurry PEEK mass fraction was estimated using first-order error propagation. The balance resolution leads to a negligible instrumental uncertainty. In practice, the overall uncertainty is dominated by procedural effects (e.g., incomplete drying or moisture reabsorption, minor handling losses, and non-PEEK residue after thermal treatment). A conservative constant method uncertainty of ± 0.125 wt% ($\pm 5mg$) is adopted for all slurry PEEK mass fraction values. The derivation of the instrumental uncertainty and the rationale for the adopted method uncertainty are provided in Appendix D.3.

4.2.4 Particle Size Distribution Analysis

To support the investigation of slurry viscosity changes caused by water evaporation, the particle size distribution of PEEK powder was analysed for each batch. This analysis aimed to determine whether Particle Size Distribution (PSD) changes occur during manufacturing and if these changes affect the pick-up behaviour of the Kiss-roller.

Specifically, the analysis evaluates whether preferential pick-up or sedimentation is linked to specific particle size ranges. Smaller particles are expected to more easily penetrate the

fibre tow and possibly migrate away from the impregnation interface, while larger particles may remain at the surface. The analysis also identifies particle size fractions that tend to sediment over time.

Measurement technique

The particle size distribution of PEEK samples is measured using a Hydro SM manual liquid dispersion unit with a Mastersizer 3000. For each slurry sample, five measurements are taken under identical conditions. The arithmetic mean of these measurements represents the PSD for that sample. Only the averaged distributions are presented in the results.

Temporal monitoring of characteristic particle diameters

In addition to standard particle size distribution curves, the temporal evolution of characteristic particle diameters is analysed. The values of D_{10}, D_{50}, and D_{90} are extracted for each sample and plotted over time for Campaign 1 and 2. This approach assesses potential time-dependent changes in particle size during manufacturing.

Relative PSD evolution with respect to the initial state

To quantify changes in particle size distribution over time, a relative volume-based PSD representation is used. For each batch, the initial PSD ($t = 0$) serves as the reference. Subsequent PSDs are expressed as percentage variations from this reference. This method helps identify shifts in particle size fractions and clarifies potential redistribution during processing.

4.3 Tape manufacturing

This chapter presents the manufacturing methodology for slurry-based tape impregnation on the Van Wees tape line. It details how the studied machine parameters influence fibre impregnation and complements the equipment information in Chapter 3.2.1.

Tape manufacturing trials were performed using a slurry with an initial solid content of 27 wt% PEEK. For Nip-roller trials, 0.5 g/l of XG was additionally used as a thickener. The focus is on the active zones that govern slurry–fibre interaction and material transport. An important point is the use of a heated spreader bar (3C, Fig. 3.14b) heated to 200°C to soften the fibre sizing, which can promote tow spreading and mixing during the Nip-roller process.

Slurry state and handling

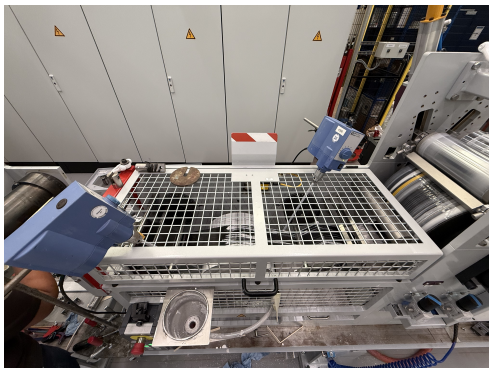
The impregnation slurry is stored and processed in an open reservoir that supplies the impregnation unit (open reservoir for Kiss-roller(Fig. 3.5 (D) and Nip-roller (Fig. 3.8 (B)). Water continuously evaporates during tape manufacturing, which is currently unavoidable and gradually increases the slurry's PEEK weight fraction.

Without an automatic refill or closed-loop control system, the slurry level in the reservoir decreases during operation. This reduction changes the immersion depth of the impregnation roller and may affect the amount of slurry transferred to the fibre tow.

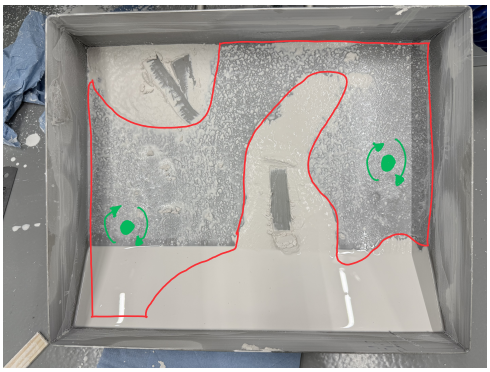
Initially, the reservoir lacked an efficient mixing system. Local mechanical mixers were subsequently installed to mitigate PEEK particle sedimentation (Figure 4.6a). Despite these

additions, Figrue 4.6b indicated persistent spatial inhomogeneity in the slurry during Kiss-roller manufacturing, characterised by:

- Well-mixed flow regions in the immediate vicinity of the mixers.
- Quasi-stagnant peripheral zones where PEEK powder deposits were observed.



(a) Implementation of two mechanical mixers above the slurry tray to improve powder dispersion and reduce particle sedimentation during Kiss-roller manufacturing.



(b) Flow behaviour of the slurry inside the Kiss-roller open tray, showing particle sedimentation and powder deposits in non-mixed peripheral zones outside of the red area. The green points represent the mixer positions and their rotation.

Consequently, the slurry delivered to the Kiss-roller may display local variations in solid content and viscosity, depending on the prevailing flow patterns within the reservoir. This configuration introduces inherent process variability and defines the experimental context in which impregnation behaviour is investigated. This leads to uncontrolled variability during tape manufacturing with the Kiss-roller.

Before being transferred to the reservoir, the slurry was stored in a separate covered container and continuously mixed to limit particle sedimentation and reduce evaporation. The slurry was transferred manually to the reservoir using a small intermediate container. There was no quantitative control of the slurry level or the consumption rate by the Kiss-roller during processing.

The slurry state evolves continuously during processing and sets the boundary conditions for machine parameters. This evolution must be considered when analysing impregnation behaviour and tape quality.

Tension-controlled

Line tension is applied during the complete impregnation, playing a central role in fibre transport and impregnation conditions.

Tension stabilises the fibre tow, maintains alignment, and controls the degree of spreading before slurry contact. By controlling the tow width and thickness, tension indirectly influences the contact area between the fibres and the slurry. During Kiss-roller impregnation, tension contributes to the normal force acting at the fibre–slurry interface, thereby affecting local shear conditions and slurry transfer mechanisms. Excessive tension can cause fibre damage or tow breakage, while insufficient tension may compromise tow spreading. In this configuration, tension is a critical process parameter influencing impregnation conditions. Total tension is created by creel tension and dry spreading angle.

Post-impregnation stages

After impregnation, the tape undergoes drying, heating, and calendering, as described in detail in Chapter 3.2.1.

Although the heating phase may redistribute the matrix and remove weakly bonded excess polymer from the tape surface (Fig. 4.7), it is not expected to alter the fibre volume fraction. The fibre volume fraction is mainly determined by the amount of matrix initially deposited during impregnation, with post-impregnation steps consolidating and stabilising it.



Figure 4.7: Excess of PEEK powder peeling off the tape surface during the melting process

4.4 Tape quality

4.4.1 Fibre volume fraction

After production, the tape is analysed to determine the fibre volume fraction (FVF).

Sample preparation and measurements

For each manufacturing condition, the tape is cut into 1000 mm sections. The first section is taken approximately 1 meter after the start of the trial, the second from the middle, and

the last 1 meter before the end. This approach ensures representative sampling for each trial.

Each tape section is weighed using a laboratory balance with of 0.1 mg readability to obtain the total tape mass M_{tape}.

The fibre mass in each tape section is determined by directly weighing the dry carbon fibre tows used during manufacturing. To account for tow-to-tow variability, two independent measurements are taken by weighing bundles of four tows over 1000 mm.

$$m_{4,1} \quad \text{and} \quad m_{4,2}. \tag{4.1}$$

The mean mass of four tows is calculated as:

$$\overline{m}_4 = \frac{m_{4,1} + m_{4,2}}{2}. \tag{4.2}$$

Since the tape contains eight fibre tows, the total fibre mass in a 1000 mm section is calculated as:

$$M_{\text{fibres}} = 2\,\overline{m}_4. \tag{4.3}$$

This method avoids reliance on manufacturer-provided linear mass values and ensures consistency between the measured fibre mass and the fibres processed on the tape line.

The matrix (PEEK) mass is calculated by subtraction:

$$M_{\text{PEEK}} = M_{\text{tape}} - M_{\text{fibres}}. \tag{4.4}$$

Calculation of fibre volume fraction

The fibre and matrix volumes are calculated using the material densities ρ_{fibres} and ρ_{PEEK} as follows:

$$V_{\text{fibres}} = \frac{M_{\text{fibres}}}{\rho_{\text{fibres}}}, \tag{4.5}$$

$$V_{\text{PEEK}} = \frac{M_{\text{PEEK}}}{\rho_{\text{PEEK}}}. \tag{4.6}$$

The fibre volume fraction is then defined as:

$$\text{FVF} = \frac{V_{\text{fibres}}}{V_{\text{fibres}} + V_{\text{PEEK}}}. \tag{4.7}$$

This mass-based method determines the fibre volume fraction without the need for direct thickness or porosity measurements.

Uncertainty estimation

The uncertainty in the fibre volume fraction was estimated using first-order (linear) error propagation. Only the main sources of uncertainty were considered: the composite tape mass and the fibre mass.

Uncertainty in tape mass is mainly due to the cutting tolerance of the 1000 mm sample length and is assumed to scale linearly with length. Fibre mass uncertainty is estimated from the variability between repeated measurements. Balance readability is negligible compared to these factors.

The resulting uncertainty in the fibre volume fraction is small compared to the observed sample variations. Only the final uncertainty values are reported in the results; full derivations and numerical examples are provided in the appendices (D.2).

4.4.2 Image-based tape quality

Tape quality was evaluated using image-based analysis with the Fiji distribution of ImageJ [52]. Images were acquired by direct photography using a smartphone camera (iPhone 16 Pro).

For each manufacturing condition, the tape segment selected for imaging corresponds to the middle 1000 mm section defined in Section 4.4.1. The image was taken at the midpoint of this section to ensure spatial consistency and representative sampling.

During image acquisition, the tape was illuminated using a fixed LED spotlight (Nanlite FS-200). Both the tape and the camera were positioned at constant distances from the light source and from each other across all measurements. Camera exposure parameters (e.g. aperture, white balance, ISO) were not manually fixed and were automatically adjusted by the device.

Image import and preprocessing

Each sample image was imported, cropped to remove peripheral regions, and rotated to align the tape direction with the vertical axis. These steps standardised image orientation for further processing.

All images were converted to 8-bit grayscale to ensure compatibility with binarisation and enable consistent grayscale-based signal extraction.

Image binarisation

After grayscale conversion, a global threshold was applied to produce a binary black-and-white image (Fig. 4.8). This step defines the region between fibre-rich and matrix-rich regions. Binarisation was performed using the Otsu thresholding method.

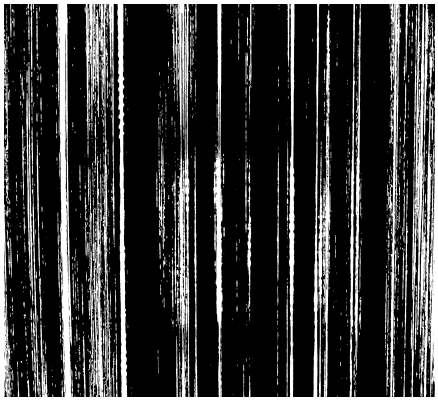


Figure 4.8: This example (T18) shows image binarisation in ImageJ using a global threshold. The grayscale image is converted to black and white to enhance contrast between fibre-rich and matrix-rich regions before extracting grayscale signals.

Definition of the region of interest

Before extracting the grayscale signal, a region of interest (ROI) was defined and analyses were restricted to the central region of the mid tape as shown in Figure 4.9. This approach focused on the representative area used for the entire analyses during this work. A single line profile was avoided due to its sensitivity to local heterogeneities. Instead, a rectangular ROI centred on the tape was used, allowing spatial averaging over a finite width while remaining focused on the central region (Fig. 4.9).

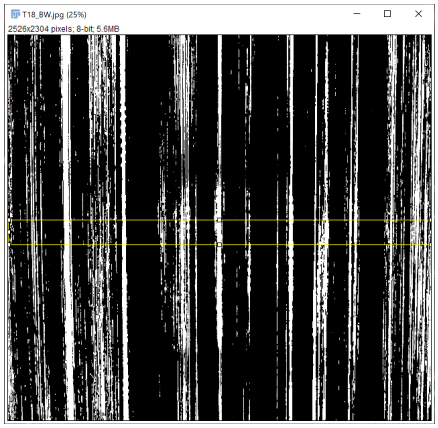


Figure 4.9: The rectangular region of interest (ROI) represented in yellow is centred on the tape width. It is chosen to ensure spatial averaging over a representative central area and to minimise bias from local heterogeneities.

The position and dimensions of the region is fixed in the middle of the tape by measuring the total length of the image in pixels. Then, the rectangle's height is set to 216 px, and the image's width is defined by the tape's width.

Gray scale signal extraction

The extracted grayscale profile (Fig. 4.10) represents the average pixel intensity over the ROI height (216 px) at each position across the tape width. Although the source image is binarised (black–white), the resulting signal is not binary. For each horizontal pixel position, the grayscale value corresponds to the average of the binary pixel intensities along the ROI height. As an example, if approximately 50% of the pixels within the ROI height are white (255) and 50% are black (0), the resulting averaged grayscale value is close to 128 on the 8-bit intensity scale. Consequently, the signal reflects the local proportion of white and black pixels in the binarised image, providing a continuous representation of lateral variations across the tape width.

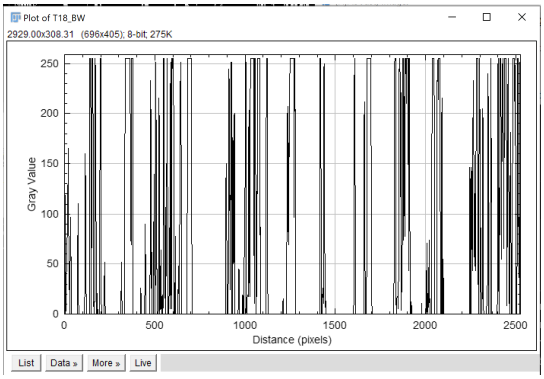


Figure 4.10: Example of grayscale intensity profile extracted from the binarised image within the defined ROI. The profile represents spatial variations in grayscale intensity across the tape width.

The raw grayscale data were exported for processing outside ImageJ.

Heatmap construction from grayscale profiles

The exported grayscale profile (`Gray_Value` in 8-bit, 0–255) was used to generate a one-dimensional heatmap representation along the tape width. For each pixel position x across the ROI, the grayscale value was normalised into a contrast variable $v \in [0, 1]$ defined as

$$v = \frac{\texttt{Gray_Value}}{255}, \tag{4.8}$$

with v clipped to the range $[0, 1]$. Based on fixed thresholds, each position was classified into one of three classes:

- composite-rich: $0 \leq v \leq 0.2$,
- PEEK-rich: $0.8 \leq v \leq 1$,
- intermediate: $0.2 < v < 0.8$.

In practice, these thresholds correspond to grayscale limits of approximately 204 and 51 in 8-bit intensity. The resulting class sequence was displayed as a colour-coded heatmap (composite-rich: yellow, intermediate: green, PEEK-rich: blue) to enable visual comparison of lateral morphology across trials.

These two thresholds were defined empirically by visually inspecting representative tape images and selecting values that gave a consistent qualitative separation between composite-rich and PEEK-rich regions across the dataset. This choice is limited by visual judgement and the range of grayscale intensities in the analysed images; therefore, the thresholds should be seen as a pragmatic, dataset-specific definition rather than a universal criterion.

Quality metrics from the heatmap (Signal Processing)

The heatmap class sequence was quantified using three groups of metrics. First, phase fractions were computed as the fraction of positions classified as composite-rich, intermediate, and PEEK-rich over the analysed width. Second, axial alternation was quantified using the transition rate, defined as the number of class changes along the sequence, normalised per 1000 pixels. Third, run-length statistics were extracted from the sequences of composite-rich and PEEK-rich classes to quantify the typical persistence length of each class. The mean and maximum run lengths were reported in pixels for composite-rich and PEEK-rich classes. The terms composite-rich and PEEK-rich refer to an image-based classification at the analysed scale. They do not directly quantify fibre–matrix homogeneity or through-thickness impregnation.

Chapter 5

Results & Discussion

5.1 Tape quality after production for Kiss-roller

Before detailing the kiss-roller results, measurement uncertainties are introduced here once, as they apply identically to both Kiss-roller and Nip-roller datasets presented in Sections 5.1 and 5.2.

Measurement uncertainties for FVF and slurry PEEK mass fraction

Measurement uncertainties were estimated using first-order linear error propagation. Only the resulting uncertainty magnitudes are reported in the results; full derivations and assumptions are included in the appendices D.2 and D.3. The following sections focus on experimental trends, as their amplitudes significantly exceed the estimated uncertainties.

Table 5.1: Representative measurement uncertainties for FVF and slurry PEEK mass fraction.

Sample	Quantity	Measured value	Estimated uncertainty
T1 Nip-roller	FVF V_f	0.714	± 0.003
T46 Kiss-roller	FVF V_f	0.505	± 0.002
T25 Kiss-roller	FVF V_f	0.610	± 0.003
250930_N01	Slurry PEEK wt%	27.41 wt%	± 0.125 wt%
250930_N05	Slurry PEEK wt%	32.20 wt%	± 0.125 wt%
251001_N06	Slurry PEEK wt%	32.97 wt%	± 0.125 wt%

Given the limited variation in estimated uncertainties across representative samples, measurement uncertainty is considered approximately constant for all datasets. Conservative constant of $\pm 0.3\%$ for FVF and ± 0.125 wt% uncertainty are used in subsequent analyses, since observed experimental variations are one to two orders of magnitude greater than the measurement uncertainty.

5.1.1 Influence of slurry PEEK weight fraction on FVF

As discussed in Section 4.2.3, continuous water evaporation during processing increases the PEEK weight fraction in the slurry. This context is shown by the black curves in Figures 5.1, 5.2, and 5.3, which illustrate the temporal evolution of PEEK concentration in the slurry. These curves do not indicate the matrix content in the final composite tape. The red curves show the FVF measured in the produced tapes, as indicated on the right vertical axis. For all three production campaign, FVF varies in correlation with changes in slurry PEEK wt%. Table 4.1 in section 4.1 shows the Trials corresponding to the campaign for the Kiss-roller.

On Campaign 1 (Fig 5.1), the FVF changes with slurry PEEK weight fraction in a non-monotonic pattern, displaying several local fluctuations. From Trial T18 to T20, FVF decreases as slurry PEEK wt% increases. Between T20 and T16, FVF rises sharply, peaking at T17, while slurry PEEK wt% drops significantly during this period. In the final 20 minutes, slurry PEEK wt% increases sharply, while FVF at sample T21 decreases markedly.

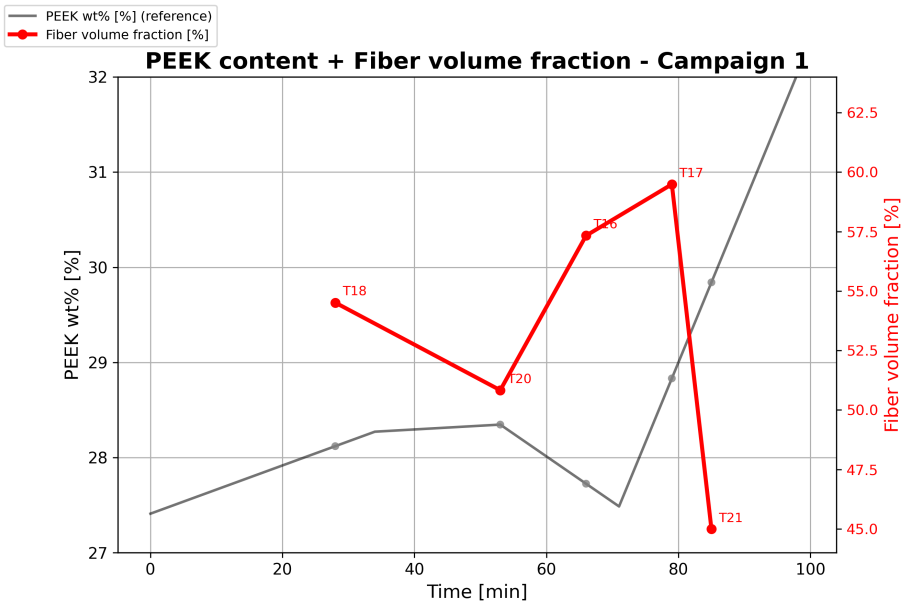


Figure 5.1: FVF as a function of PEEK weight fraction - Campaign 1 (Kiss-roller impregnation).

On Campaign 2 (Fig 5.2), the FVF evolves differently than on Campaign 1. From samples T22 to T26, both FVF and slurry PEEK wt% increase. From T26 to T28, both decrease. Disregarding short-term fluctuations, a longer-term trend emerges between samples T28 and T41: FVF decreases overall, while slurry PEEK wt% progressively increases.

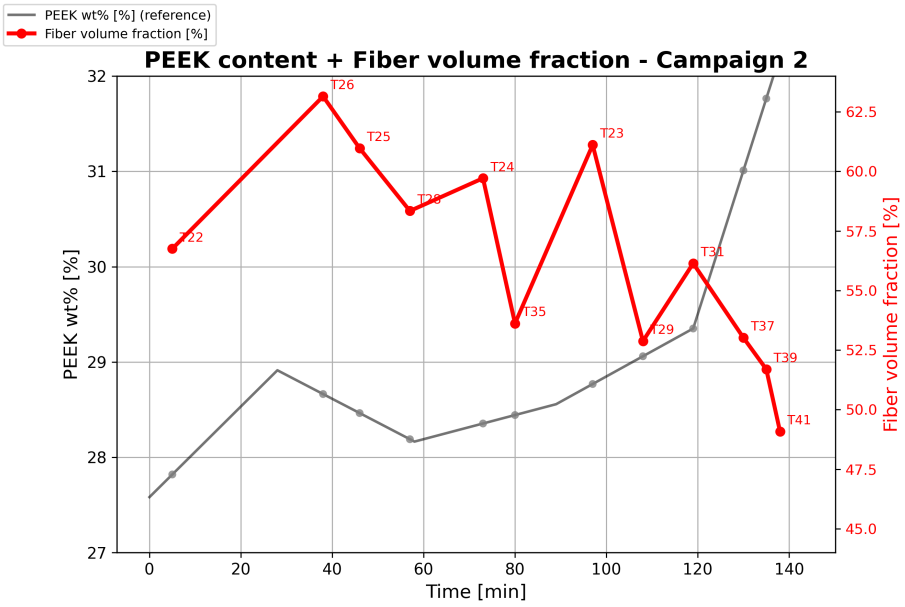


Figure 5.2: FVF as a function of PEEK weight fraction - Campaign 2 (Kiss-roller impregnation).

On Campaign 3 (Fig 5.3), although the slurry PEEK wt% values are interpolated rather than directly measured, a clear trend is evident. The FVF decreases as the slurry PEEK wt% increases. This pattern aligns with the longer-term trend observed on Campaign 1 and Campaign 2, where increasing slurry PEEK wt% corresponds to a decrease in FVF.

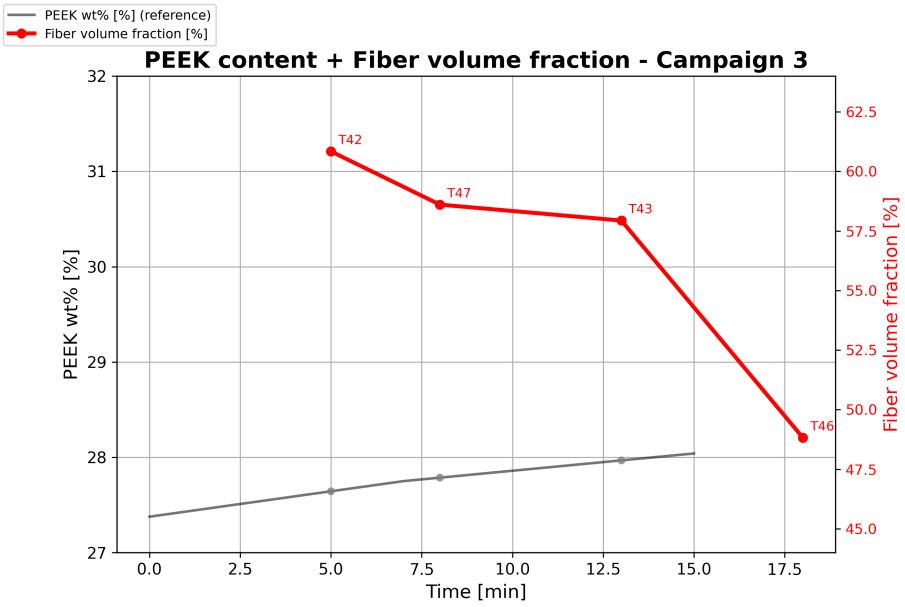


Figure 5.3: FVF as a function of PEEK weight fraction - Campaign 3 (Kiss-roller impregnation).

The results indicate that FVF during Kiss-roller impregnation is sensitive to the PEEK weight fraction in the slurry. The increase in slurry PEEK wt% is due to water evaporation, a known process drift.

Two types of fluctuations are evident in the FVF data. The data indicate that changes in slurry composition affect impregnation, as reflected by FVF variations. Over time, FVF generally decreases as slurry PEEK wt% increases during processing. This trend suggests that slurry composition drift acts as a long term first-order contributor governing the impregnation outcomes.

Variation in FVF at similar PEEK wt% levels highlights the influence of additional process-dependent such as factors changes in machine parameters, local slurry inhomogeneities, changes in slurry film thickness function of viscosity from the Kiss-roller, transient reservoir level fluctuations. Consequently, actual impregnation conditions may differ from those predicted by average slurry composition. These factors can cause transition improvements or degradations in impregnation, explaining the short-term peaks and drops in FVF.

Campaign 3 (Fig 5.3) was the most stable, as it was conducted with a single parameter (calender pressure) and consistent manufacturing conditions, both of which had a significant impact. The test duration was also short. Additionally, the tray was not refilled during this campaign, which may have contributed to the stable evaporation trend. The effect of manufacturing parameters will be adressed in the section 5.1.

Overall, these results show that slurry PEEK wt% is a key parameter for FVF, but its effect depends on process stability and local flow conditions. FVF in the final tape is determined by both slurry composition and dynamic impregnation conditions.

To limit bias associated with this monotonic drift, the order of Trials was randomised during manufacturing. Each Trial can nevertheless be positioned on a global time axis. Each experimental point is unique (no replicates). The experimental uncertainty on FVF (FVF) is estimated at $\pm 0.3\%$ (absolute).

Because slurry PEEK wt% does not fully account for FVF variability, PSD was also tracked to assess powder dispersion stability over time. This approach aims to identify whether changes in dispersion, such as agglomeration or sedimentation during evaporation, contribute to local differences in impregnation results.

5.1.2 Particle size distribution evolution for Kiss-roller

Figure 5.4 and 5.6 show the average particle size distributions (PSD) measured at different sampling times during Campaign 1 and Campaign 2. To highlight small variations, differential curves relative to the initial state are reported (Fig. 5.5,5.7). For a quantitative overview, Table 5.2 presents the numerical values.

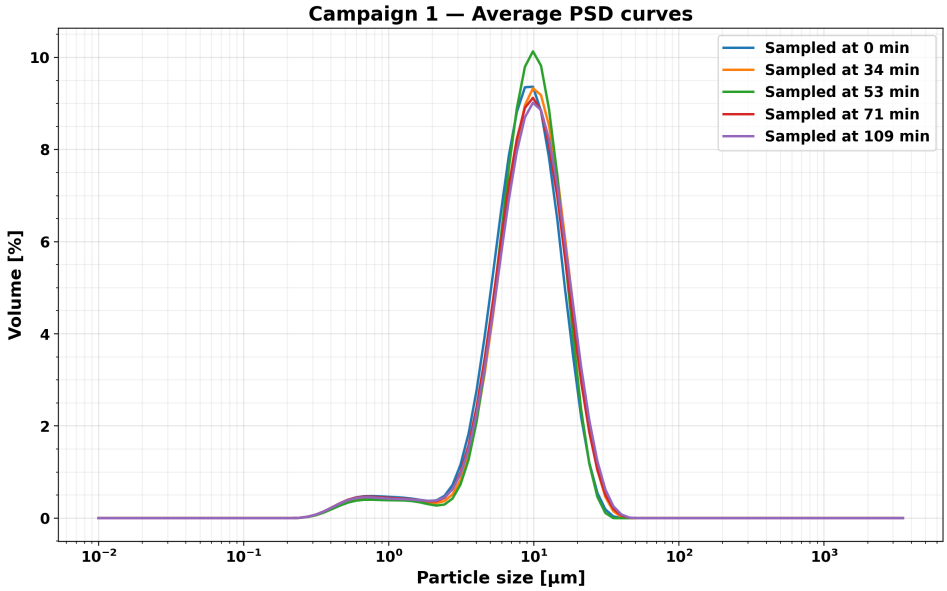


Figure 5.4: Average PSD measured at different sampling times.

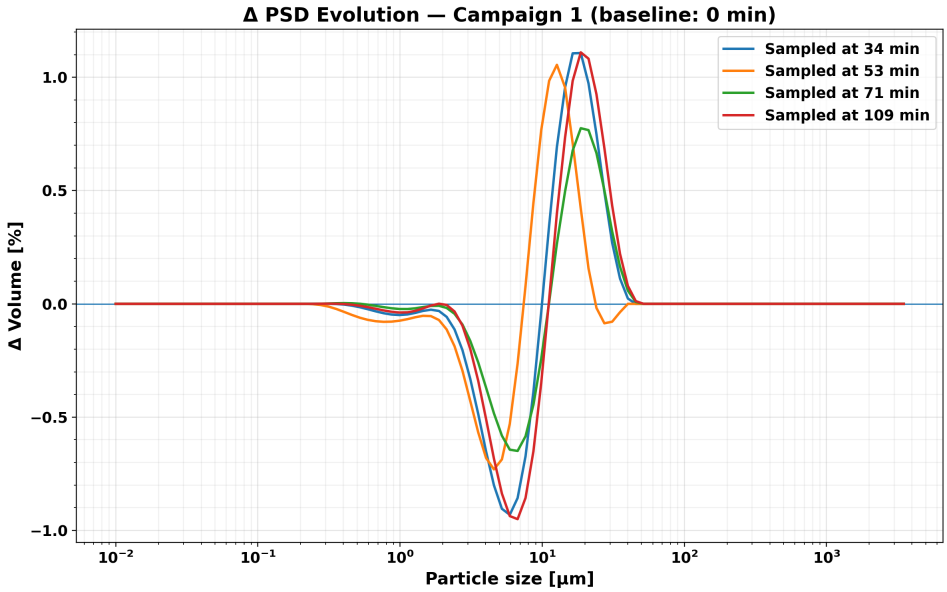


Figure 5.5: Differential PSD evolution relative to the initial state ($t = 0$(D50=∼9.28 µm)). Positive and negative values indicate respectively an increase or decrease in volume fraction for a given size class.

Figure 5.4 shows that the PSD remains similar over time and is dominated by a main mode centred at ∼10 µm. The differential curves relative (Fig. 5.5) indicate a redistribution around the main mode, with a decrease in the intermediate size range (about 5–9 µm) and an increase in a larger range (about 12–25 µm). The observed variations are small but consistent (order of ∼1% in volume).

Similarly, the average PSD curves of Campaign 2 remain dominated by a main mode around ∼10 µm (Fig. 5.6).

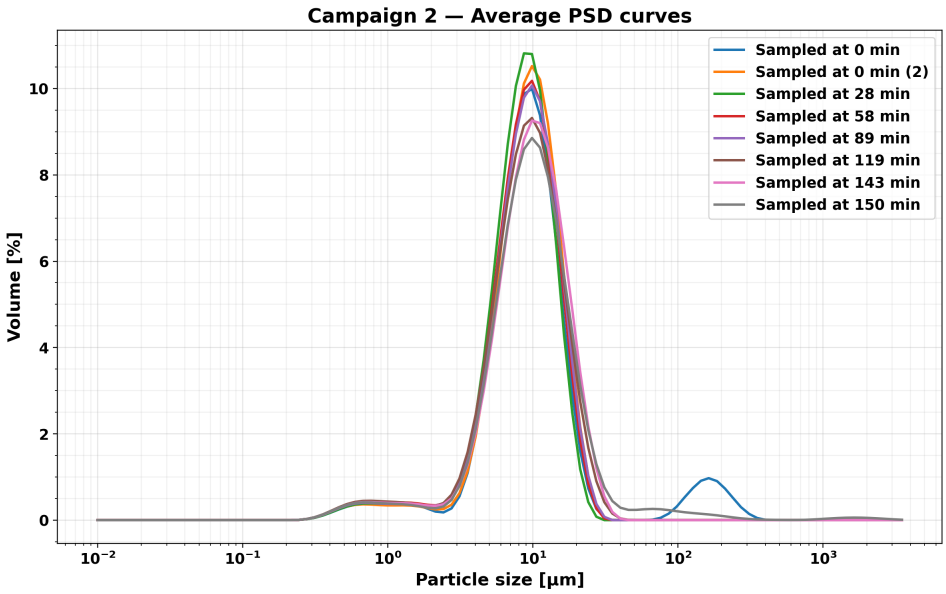


Figure 5.6: Average PSD measured at different sampling times.

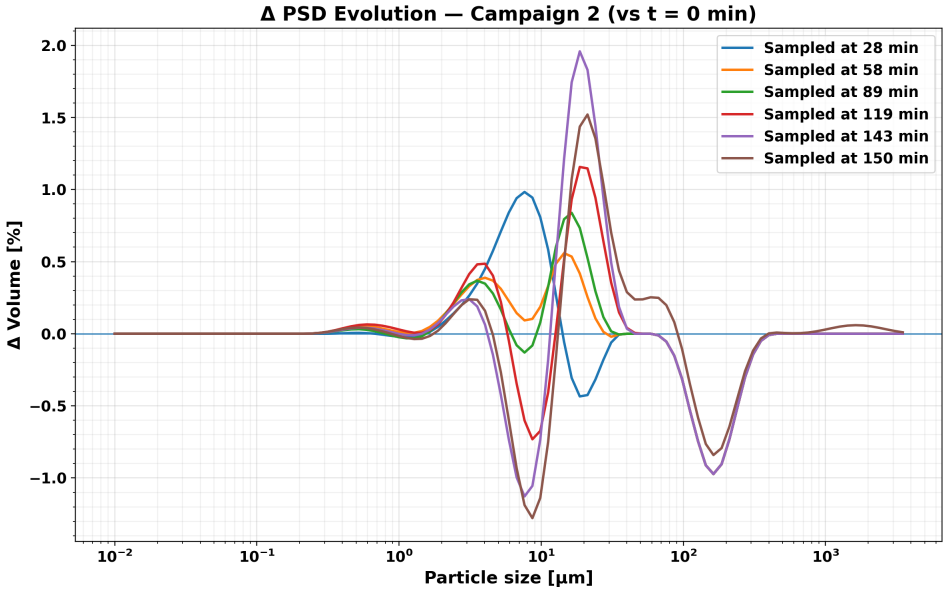


Figure 5.7: Differential PSD evolution relative to the initial state ($t = 0$(D50=∼10.00 µm)). Positive and negative values indicate respectively an increase or decrease in volume fraction for a given size class.

The ΔPSD curves (Fig. 5.7) display multiple peaks across the main-mode region. Early-time behaviour (e.g., 28 min) shows an opposite trend to later samples. Pronounced coarse-size contributions (order ∼100–300 µm) observed for the 143 and 150 min curves come from samples collected from sedimented powder at the bottom of the reservoir and do not

represent a homogeneous bulk slurry state and may contain impurities such as fragmented broken fibres.

Table 5.2: Summary of particle size distribution (PSD) averages for slurry samples.

Campaign	Sampled at (min)	D_{10} (μm)	D_{50} (μm)	D_{90} (μm)
1	0	4.26	9.28	16.54
1	34	4.73	10.18	18.35
1	53	4.98	9.92	16.76
1	71	4.46	9.86	18.19
1	109	4.53	10.12	18.77
2	0	5.21	10.01	16.42
2	0	4.88	9.26	14.92
2	28	4.67	9.56	16.01
2	58	4.75	9.74	16.41
2	89	4.57	9.76	17.76
2	119	4.84	10.41	18.85
2	143	5.21	9.94	18.66
2	150	4.91	10.45	21.76

Across both campaigns, the PSD differences relative remain limited in amplitude and are mostly small redistributions around the main mode. A tentative common feature is that the differential curves often show paired negative and positive peaks, consistent with a transfer of volume between neighbouring size classes.

Several physical factors may contribute to such shifts. First, evaporation during processing was observed and can increase solids content and viscosity, which may promote time-dependent changes in the dispersion state (e.g., flocculation/agglomeration) and modify suspension microstructure. Second, the Kiss pick-up mechanism may be size-selective: the transferred film is governed by local rheology, wetting and film thickness, and may not be representative of the bulk reservoir. Campaign 2 also shows that spatial heterogeneity can develop, as evidenced by sedimentation-related coarse fractions in bottom samples. These mechanisms are proposed to contextualise the observations, but they cannot be separated with the available measurements.

These PSD and PEEK wt% observations offer context on slurry stability but do not identify the source of FVF scatter. The next section examines how manufacturing parameters influence FVF during Kiss-roller impregnation.

5.1.3 Influence of Machine Parameters on FVF Kiss-roller

In this analysis, the mid measurement is used as the representative value because it reflects the steady-state operating conditions. The begin and end measurements are used to assess the process's temporal stability by quantifying the variation observed during production. Table 5.3 presents the mid value and its associated variation amplitude. The horizontal bar above T31 indicates the FVF study range, from 55% to 65%.

Table 5.3: Summary of FVF values. The variation amplitude reflects the temporal stability.

Campaign	Trial	FVF_{mid} [%]	ΔFVF (max−min) [%]
1	T21	45.0	7.05
3	T46	48.8	5.65
2	T41	49.1	5.40
1	T20	50.8	1.92
2	T39	51.7	3.10
2	T29	52.9	2.78
2	T37	53.0	1.15
2	T35	53.6	3.26
1	T18	54.5	9.38
2	T31	56.1	2.17
2	T22	56.7	2.23
1	T16	57.3	3.59
3	T43	57.9	4.62
2	T28	58.3	3.04
3	T47	58.6	2.50
1	T17	59.5	4.76
2	T24	59.7	6.75
3	T42	60.8	9.68
2	T25	61.0	2.29
2	T23	61.1	4.98
2	T26	63.2	9.56

Effect of line speed

Figures 5.8, 5.11, 5.13 and 5.15 show how FVF varies with line speed from 3 to 5 m/min for three creel tension configurations in the campaigns studied.

– Campaign 1 (fixed $L = 500$ cN)

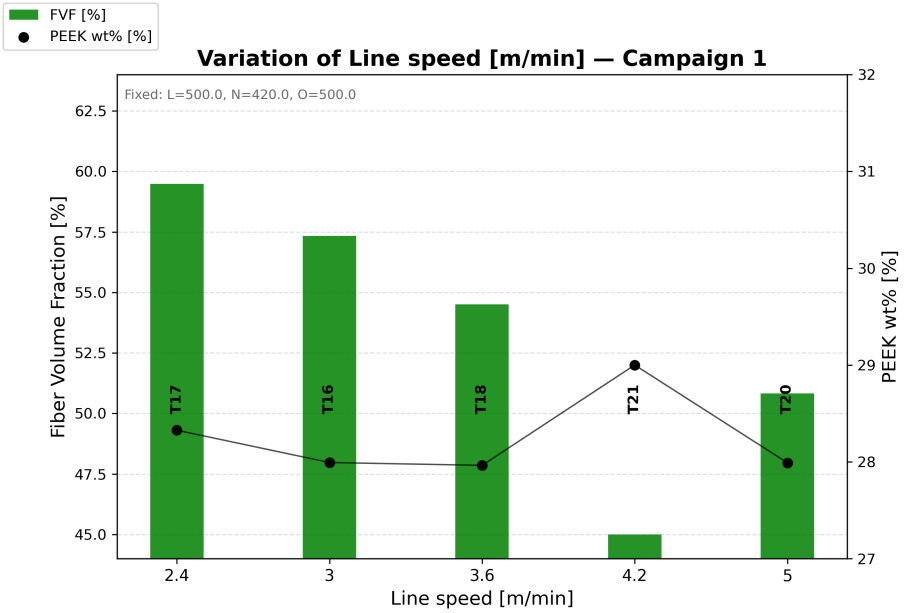


Figure 5.8: Effect of line speed on FVF during Campaign 1 at fixed creel tension, impregnation temperature, and calendar pressure. $\Delta\text{PEEKcontent(abs)} = 1.04\%$

In Campaign 1 (Fig. 5.8), both FVF and PEEK wt% decrease as line speed increases. This trend is consistent throughout the dataset, except for Trial T21, which deviates in both FVF and its position within the dataset.

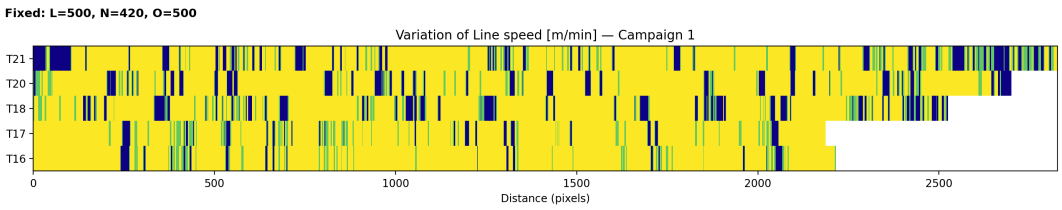


Figure 5.9: Effect of line speed on tape morphology during Campaign 1 at fixed creel tension, impregnation temperature, and calendar pressure. Composite-rich: yellow, intermediate: green, PEEK-rich: blue

Table 5.4: Line speed (Campaign 1): Quality metrics

Trial	Line speed [m/min]	FVF [%]	Fractions (comp / int / PEEK) [-]	Transitions [/1000 px]	Mean run (comp.) [px]	Max run (comp.) [px]	Max run (PEEK) [px]
T21	4.2	45.0	0.695 / 0.138 0.167	59.8	23.1	221	57
T20	5.0	50.8	0.782 / 0.093 0.125	43.0	36.4	238	28
T18	3.6	54.5	0.715 / 0.129 0.156	57.0	25.1	188	28
T17	2.4	59.5	0.824 / 0.114 0.062	56.7	28.6	209	20
T16	3.0	57.3	0.870 / 0.084 0.046	46.5	37.1	241	23

The heatmap (Fig. 5.9 and metrics (Tab. 5.4) highlight distinct morphological differences between Trials. The term transition is assessed using the transition rate/1000px. T16 is primarily composite-rich with moderate interruptions. T18 and T21 alternate frequently between composite-rich and PEEK-rich segments. T20 is more composite-dominated than T18 and T21, with lower axial transition. T17 is composite-rich but exhibits frequent interruptions and shorter continuous composite-rich segments. T21 contains the longest PEEK-rich segment among the Trials. Morphology-based indicators only partially align with the FVF ranking in Campaign 1 (Fig. 5.8).

– Campaign 2 ($L = 500$ cN)

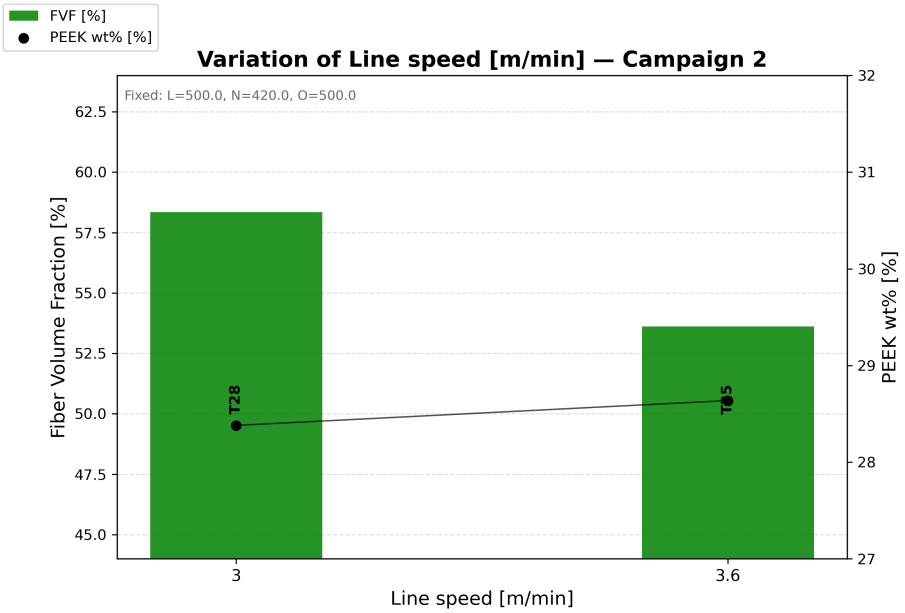


Figure 5.10: Effect of line speed on FVF during Campaign 2 at fixed creel tension, impregnation temperature, and calendar pressure.

In Campaign 2 at $L = 500$ cN (Fig. 5.10), increasing the line speed from 3.0 to 3.6 m/min reduces the FVF. This aligns with the long-term trend observed in this study, where higher slurry PEEK wt% corresponds to lower FVF.

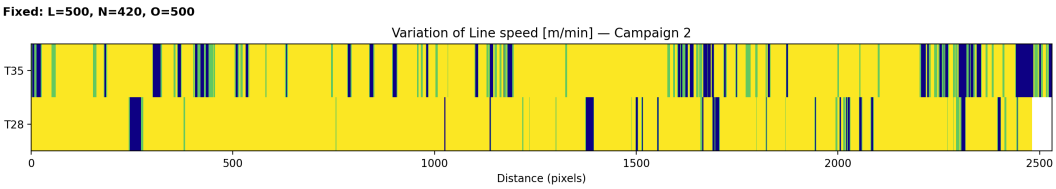


Figure 5.11: Effect of line speed on tape morphology during Campaign 2 at $L = 500$ cN, with fixed impregnation temperature and calendar pressure.

Table 5.5: Line speed (Campaign 2, L = 500): quality metrics

Trial	Line speed [m/min]	FVF [%]	Fractions (comp / int / PEEK) [-]	Transi-tions [/1000 px]	Mean run (comp.) [px]	Max run (comp.) [px]	Max run (PEEK) [px]
T35	3.6	53.6	0.732 / 0.142 0.126	51.3	28.5	249	43
T28	3.0	58.3	0.913 / 0.038 0.049	25.8	68.6	373	29

Figure 5.11 and Table 5.5 highlight T28 is primarily composite-rich with minimal interruptions. In contrast, T35 frequently shifts between composite-rich, intermediate, and PEEK-rich segments. At higher line speeds, T35 displays greater axial transition, less composite-rich continuity, and a higher proportion of PEEK-rich segments, with longer PEEK-rich interruptions than T28.

– Campaign 2 ($L = 700$ cN)

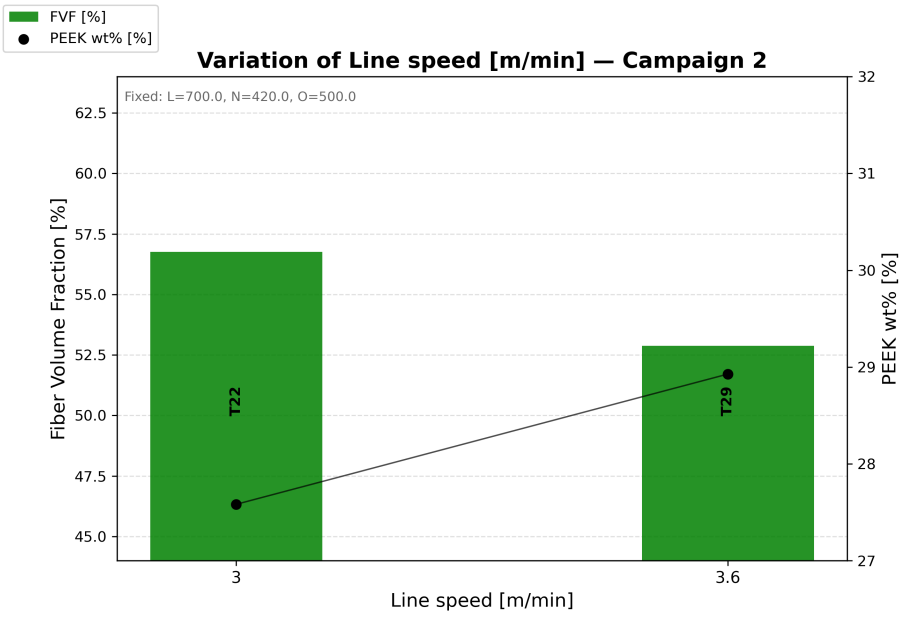


Figure 5.12: Effect of line speed on FVF during Campaign 2 for a higher creel tension. $\Delta\text{PEEKcontent(abs)} = 1.35\%$

In Campaign 2 at $L = 700$ cN (Fig. 5.12), increasing the line speed from 3.0 to 3.6 m/min is associated with a decrease in FVF.

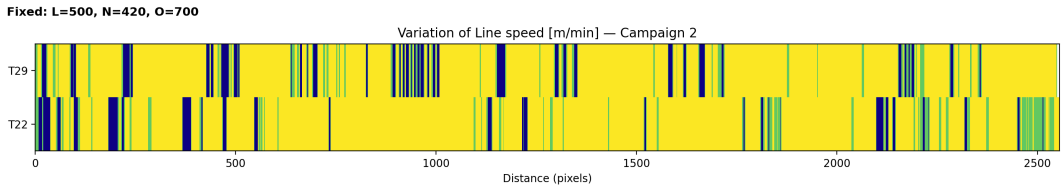


Figure 5.13: Effect of line speed on tape morphology during Campaign 2 for a medium creel tension.

Table 5.6: Line speed (Campaign 2, L = 700): quality metrics

Trial	Line speed [m/min]	FVF [%]	Fractions (comp / int / PEEK) [-]	Transi-tions [/1000 px]	Mean run (comp.) [px]	Max run (comp.) [px]	Max run (PEEK) [px]
T29	3.6	52.9	0.784 / 0.111 0.105	44.7	35.1	188	20
T22	3.0	56.8	0.801 / 0.120 0.079	41.9	37.9	356	23

Figure 5.13 and Table 5.6 show that both Trials exhibit a composite-rich morphology with transition PEEK-rich regions. The higher line speed configuration (T29) is slightly more fragmented than T22 and contains fewer long, continuous composite-rich areas. In both Trials, PEEK-rich regions remain small, indicating brief interruptions rather than extended zones.

– Campaign 2 ($L = 1000$ cN)

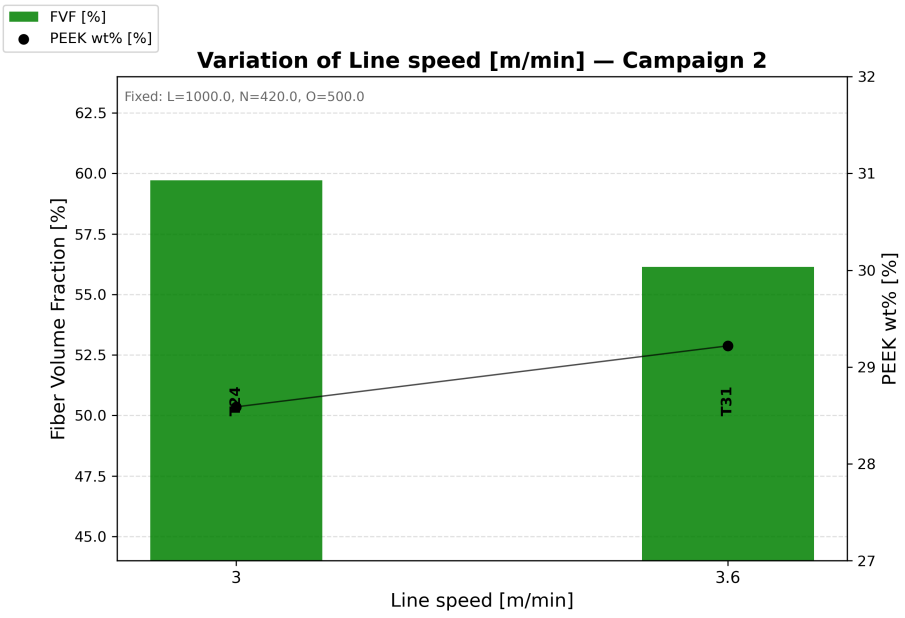


Figure 5.14: Effect of line speed on FVF during Campaign 2 for a higher creel tension investigated. $\Delta\text{PEEKcontent(abs)} = 0.63\%$

In Campaign 2 at $L = 1000$ cN (Fig. 5.14), increasing the line speed from 3.0 to 3.6 m/min is also associated with a decrease in FVF.

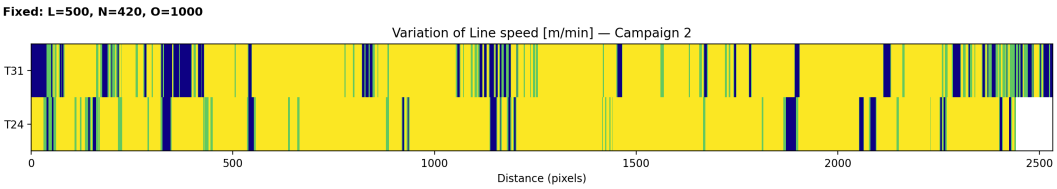


Figure 5.15: Effect of line speed on tape morphology during Campaign 2 at $L = 1000$ cN, with fixed impregnation temperature and calendar pressure.

Table 5.7: Line speed (Campaign 2, L = 1000): quality metrics

Trial	Line speed [m/min]	FVF [%]	Fractions (comp / int / PEEK) [-]	Transitions [/1000 px]	Mean run (comp.) [px]	Max run (comp.) [px]	Max run (PEEK) [px]
T31	3.6	56.1	0.711 / 0.146 0.143	50.5	28.2	216	39
T24	3.0	59.7	0.849 / 0.089 0.061	30.7	54.6	224	25

Figure 5.15 and Table 5.7 show that both Trials exhibit a composite-rich morphology with transition PEEK-rich regions. The higher line speed configuration (T29) is slightly more fragmented than T22 and contains fewer long, continuous composite-rich areas. In both Trials, PEEK-rich regions remain small, indicating brief interruptions rather than extended zones. T24 is mainly composite-rich with occasional PEEK-rich streaks. In contrast, T31 exhibits more frequent transitions and a greater presence of intermediate and PEEK-rich segments. At higher line speeds, T31 shows increased axial transition and reduced composite-rich continuity, although the length of continuous composite-rich regions remains similar. T31 also has longer PEEK-rich interruptions and a higher proportion of PEEK-rich segments than T24.

– Synthesis: line speed across creel tensions and campaign comparison

Across Campaign 2, increasing the line speed from 3.0 to 3.6 m/min consistently reduces FVF at all creel tension levels (Tab 5.8).

Table 5.8: Line-speed-induced change in FVF from 3.0 to 3.6 m/min.

Creel tension	FVF(3.0) [%]	FVF(3.6) [%]	ΔFVF_{abs} [pp]	ΔFVF_{rel} [%]
500 cN	58.3	53.6	4.72	8.09
700 cN	56.7	52.9	3.87	6.82
1000 cN	59.7	56.1	3.57	5.98

In Campaign 2, morphology-based indicators align with FVF trends. The most significant difference between 3.0 and 3.6 m/min appears at $L = 500$ cN, where higher line speed increases axial transition, reduces composite-rich continuity, and produces more PEEK-rich segments. At $L = 700$ cN, the effect is less pronounced, with only slightly more fragmented morphology at 3.6 m/min and few PEEK-rich . At $L = 1000$ cN, higher line speed again increases axial transition, reduces composite-rich continuity, and leads to more frequent and extensive PEEK-rich segments.

A direct comparison at $L = 500$cN highlights differences between Campaign 1 and Campaign 2. Despite variations in PEEK content, both campaigns show similar FVF at the same tension, although the PEEK wt% trend is reversed. In Campaign 2, increasing line speed from 3.0 to 3.6 m/min reduces FVF (T28 to T35) and alters morphology, resulting in higher axial transition and more PEEK-rich segments. In Campaign 1, FVF also decreases as line speed increases, but morphology-based indicators only partially correspond to FVF, as the high-FVF Trial T17 still exhibits fragmented morphology. Overall, Campaign 2 demonstrates a more consistent relationship between FVF and morphology, while Campaign 1 suggests that additional factors beyond line speed influence the results.

From a process perspective, increasing line speed reduces the residence time of the fibre bundle in contact with the slurry film, which is expected to limit impregnation efficiency and decrease FVF.

A key limitation of these experiments is that line speed variations were not performed under strictly constant slurry conditions. The slurry PEEK content changes during processing and acts as a confounding parameter, partially masking the isolated effect of line speed.

The pronounced deviation in Trial T21 may be due to transient process conditions, local slurry inhomogeneities during sampling, or measurement error. A second analysis of this tape is recommended. Given the number of Trials, treating T21 as an outlier is appropriate at this stage. Future work seeking to isolate the influence of line speed would benefit from improved control of slurry composition. This would allow the respective contributions of residence time and slurry state to be separated.

The interaction between line speed and creel tension will be developed in a subsequent chapter.

Effect of creel tension

Figures 5.16 and 5.18 show how FVF varies with creel tension from 250 to 1300 cN for two line speed configurations in the campaigns studied.

– Campaign 2 ($M = 3.0$ m/min)

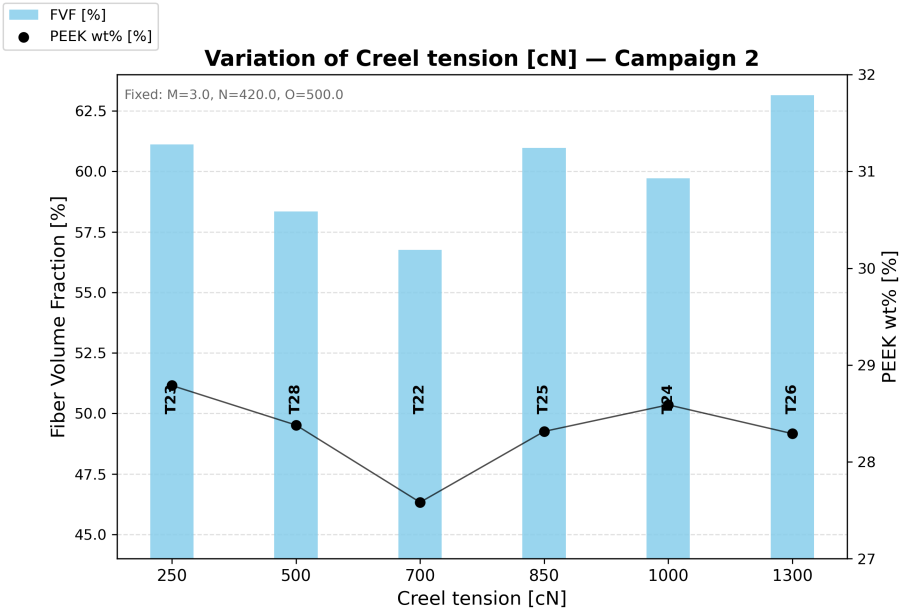


Figure 5.16: FVF as a function of creel tension during Campaign 2, with fixed line speed, impregnation temperature, and calendar pressure. $\Delta\text{PEEKcontent(abs)} = 1.21\%$

Table 5.9: Creel-tension-induced change in FVF at fixed line speed ($M = 3.0$ m/min).

Tension step	ΔFVF_{abs} [pp]	ΔFVF_{rel} [%]
500 → 700 cN	1.59	2.73
700 → 1000 cN	2.96	5.22
500 → 1000 cN	1.37	2.35

At 3.0 m/min (Fig. 5.16), increasing creel tension from 500 to 700 cN decreases FVF, while a further increase to 1000 cN raises it. Table 5.10 shows the absolute and relative variations between three tensions.

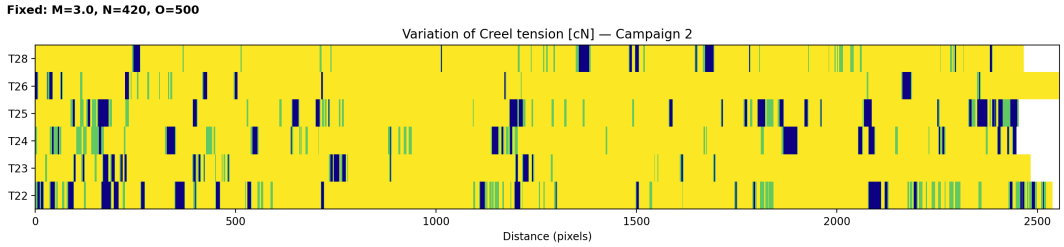


Figure 5.17: Tape morphology as a function of creel tension during Campaign 2, with fixed line speed, impregnation temperature, and calendar pressure.

Table 5.10: Creel tension (Campaign 2, M = 3.0): quality metrics

Trial	Creel tension [cN]	FVF [%]	Fractions (comp / int / PEEK) [-]	Transitions [/1000 px]	Mean run (comp.) [px]	Max run (comp.) [px]	Max run (PEEK) [px]
T28	500	58.3	0.915 / 0.048 0.037	26.0	68.4	272	25
T26	1300	63.1	0.946 / 0.025 0.029	14.5	127.2	861	21
T25	850	61.0	0.811 / 0.090 0.099	33.0	48.5	322	25
T24	1000	59.7	0.836 / 0.100 0.065	31.0	53.8	241	35
T23	250	61.1	0.917 / 0.041 0.043	22.5	78.5	786	13
T22	700	56.8	0.779 / 0.129 0.091	44.5	34.7	371	30

The heatmap 5.17 and Table 5.10 show distinct morphological differences across creel tension levels, although composite-rich regions dominate all Trials. T26 and T23 have the highest composite-rich fractions and the lowest axial transition, characterised by long, continuous composite-rich segments. In contrast, T22 displays the most alternated morphology, with the highest transition rate, a lower composite-rich fraction, and shorter composite-rich continuity. T28, T24, and T25 exhibit intermediate behaviour, with higher axial transition and reduced composite-rich continuity compared to the most stable cases. Across all Trials, PEEK-rich remain moderate in size, indicating frequent interruptions rather than large PEEK-rich zones.

– Campaign 2 ($M = 3.6$ m/min)

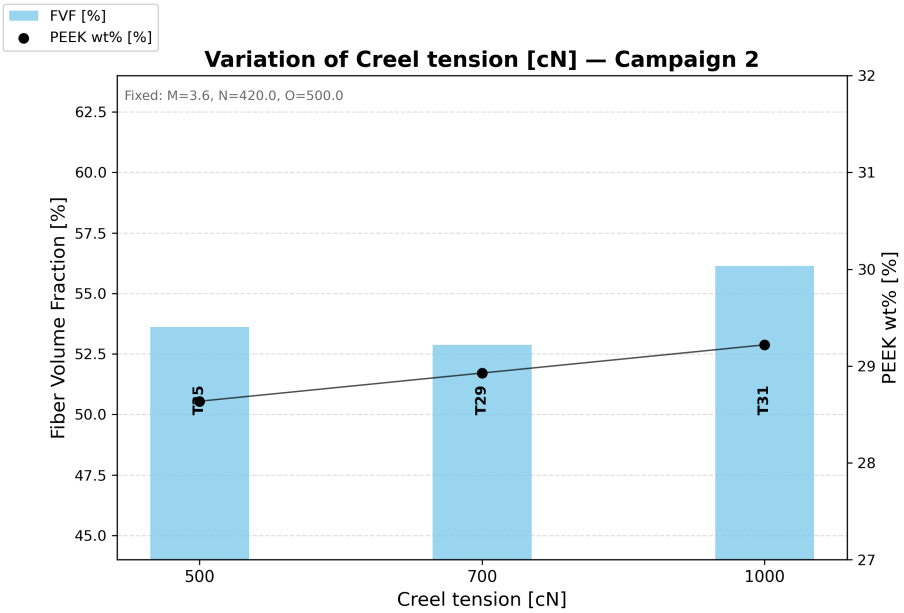


Figure 5.18: FVF as a function of creel tension during Campaign 2 for an alternative fixed line speed configuration. $\Delta\text{PEEKcontent(abs)} = 0.58\%$

Table 5.11: Creel-tension-induced change in FVF at fixed line speed.

Tension step	ΔFVF_{abs} [pp]	ΔFVF_{rel} [%]
500 → 700 cN	0.74	1.38
700 → 1000 cN	3.26	6.17
500 → 1000 cN	2.52	4.70

A similar non-monotonic pattern appears at 3.6 m/min (Fig. 5.18). FVF changes little between 500 and 700 cN, then varies more significantly from 700 to 1000 cN. Table 5.12 shows the absolute and relative variations between three tensions.

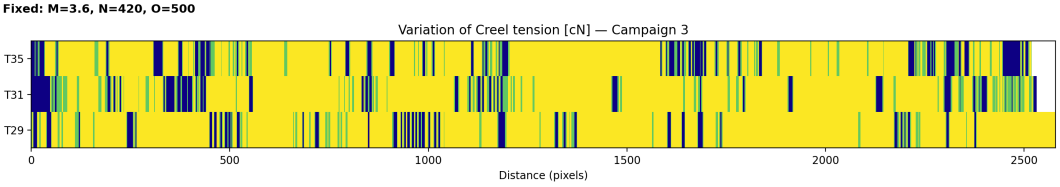


Figure 5.19: Tape morphology as a function of creel tension during Campaign 2 for an alternative fixed line speed configuration.

Table 5.12: Creel tension (Campaign 2, $M = 3.6$): quality metrics

Trial	Creel tension [cN]	FVF [%]	Fractions (comp / int / PEEK) [-]	Transitions [/1000 px]	Mean run (comp.) [px]	Max run (comp.) [px]	Max run (PEEK) [px]
T35	500	53.6	0.719 / 0.135 0.146	54.8	26.3	379	44
T31	1000	56.1	0.738 / 0.149 0.113	54.5	27.1	216	48
T29	700	52.9	0.816 / 0.093 0.091	47.7	34.0	342	16

The heatmap 5.19 and Table 5.12 show all three Trials are composite-rich, with frequent interruptions across the tape width. T29 has the highest composite-rich fraction, while T31 and T35 have higher intermediate and PEEK-rich fractions. The transition rate is high in all Trials. T31 and T35 exhibit longer PEEK-rich interruptions than T29.

– Synthesis: creel tension at $M = 3.0$ vs $M = 3.6$ m/min

For both line speeds, the FVF response to creel tension is non-monotonic. At $M = 3.0$ m/min, FVF decreases between 500 and 700 cN, then increases at higher tensions, reaching its minimum at 700 cN and maximum at 1300 cN. At $M = 3.6$ m/min, FVF also has a local minimum at 700 cN and rises from 700 to 1000 cN, with only minor changes from 500 to 700 cN. At both speeds, FVF varies more from 700 to 1000 cN than from 500 to 700 cN.

Morphology-based indicators reflect this non-monotonic trend. At $M = 3.0$ m/min, the lowest FVF aligns with the most alternated morphology and a reduced composite-rich fraction. The highest FVF corresponds to the lowest axial transition and the longest continuous composite-rich runs. At $M = 3.6$ m/min, all Trials show a highly fragmented regime, with tension differences mainly affecting phase fractions.

Line speed - creel tension interaction

The effect of line speed on FVF depends on creel tension. As creel tension increases from 500 to 1000 cN, the speed-induced variation in FVF decreases from $\Delta\text{FVF} = 4.72\%$ to $\Delta\text{FVF} = 3.57\%$. This 1.15-point, or 24% reduction, indicates that higher creel tension can mitigate the negative effects of increased line speed. Creel tension is therefore a key parameter controlling the sensitivity of the impregnation process to line speed changes.

Morphology-based indicators provide additional context for this interaction. In Campaign 2, increasing line speed produces a more alternated and PEEK-rich morphology at all tension levels, which aligns with the FVF trends. The significance of morphology change varies with tension: the contrast between 3.0 and 3.6 m/min is most pronounced at $L = 500$ cN, moderate at $L = 700$ cN, and still present at $L = 1000$ cN.

This interaction demonstrates that mechanical and rheological effects during slurry-based impregnation are interconnected, so process parameters should be considered together. However, adjusting multiple parameters at once is challenging in manufacturing because real-time optimisation is complex.

In Campaign 2, a line speed of 3.0 m/min and a creel tension of 1000 cN yield a FVF near 60% with a slurry containing about 28.6 wt% PEEK. These conditions define an operating

window within the tested parameter range and slurry composition. Adjusting the slurry PEEK content is expected to shift this window.

Although no strict replicates were performed, consistent trends across Trials support identifying an operational rather than a statistical optimum. This optimum arises from the interaction between line speed and creel tension, not from optimising each parameter independently.

This optimisation focuses only on FVF. Heatmaps provide complementary information. In Table 5.10, Trials such as T23 and T26 show lower transition rates and longer maximum composite-rich runs than T24, while also exhibiting different FVF levels. This may indicate a more laterally continuous morphology in the analysed width profile for these tensions within this dataset, but it does not invalidate the FVF-based operating window defined above.

The reduced sensitivity of FVF to line speed at high creel tension indicates greater process robustness near the identified operating point, within the limitations of this dataset. However, this interpretation is specific to the investigated parameter window and slurry state. The morphology descriptors are extracted from a limited region of interest and should be interpreted as comparative indicators within this dataset, not as general quality criteria.

Effect of calendar pressure

Figures 5.20 and 5.22 illustrate the variation in FVF with calendar pressure from 500 to 3000 N for two melting temperature configurations. The corresponding morphologies are shown in Figs. 5.21 and 5.23, and in Tables 5.13 and 5.14.

– Campaign 2 ($N = 420°C$)

In Campaign 2 (Fig. 5.20), FVF changes only slightly across 500–3000 N, and no clear monotonic relationship with calendar pressure is observed. During these Trials, a decrease in FVF aligns with an increase in slurry PEEK wt%, consistent with the long-term trend identified in this study.

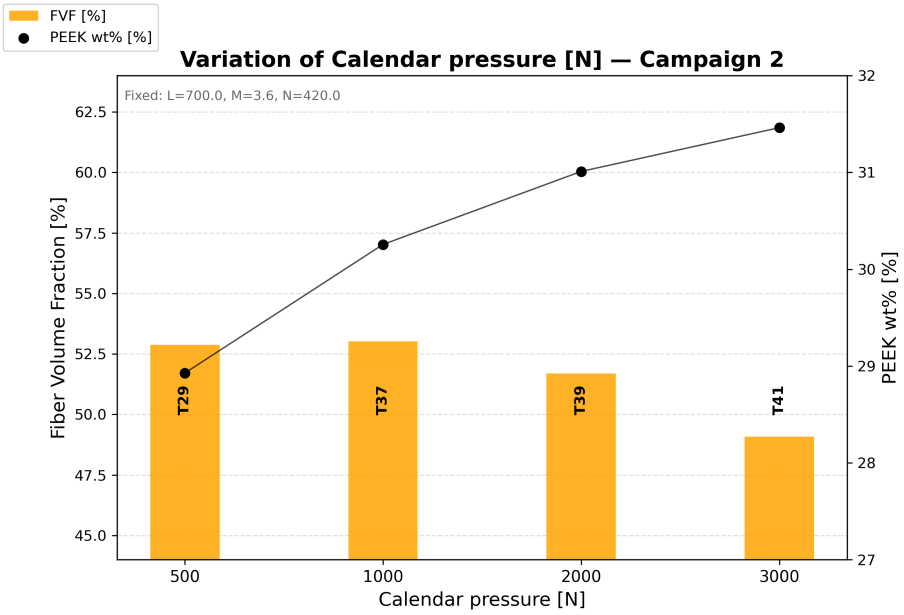


Figure 5.20: Influence of calendar pressure on FVF during Campaign 2 at fixed creel tension, line speed, and impregnation temperature. $\Delta\text{PEEKcontent(abs)} = 2.54\%$

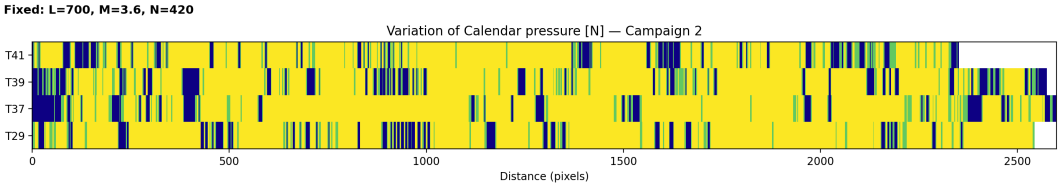


Figure 5.21: Effect of calendar pressure on tape morphology during Campaign 2 at fixed creel tension, line speed, and melting temperature ($N = 420°C$).

Table 5.13: Calendar pressure (Campaign 2, $N = 420°C$): quality metrics.

Trial	Calendar pressure [N]	FVF [%]	Fractions (comp / int / PEEK) [-]	Transi-tions [/1000 px]	Mean run (comp.) [px]	Max run (comp.) [px]	Max run (PEEK) [px]
T41	3000	49.1	0.705 / 0.153 0.142	57.8	24.4	162	19
T39	2000	51.7	0.693 / 0.145 0.162	61.4	22.6	214	42
T37	1000	53.0	0.765 / 0.109 0.126	39.2	39.0	522	56
T29	500	52.9	0.767 / 0.112 0.122	52.7	29.1	182	22

The heatmap (Fig.5.21) and metrics (Tab5.13 indicate Trial-to-Trial differences in lateral morphology across calendar pressures, mainly due to axial transition and the peek-rich region. However, these changes do not follow a consistent trend as pressure increases, which aligns with the limited and non-monotonic FVF variations shown in Fig. 5.20.

– Campaign 3 ($N = 450°C$)

In Campaign 3 (Fig. 5.22), FVF does not visibly depend on calendar pressure between 500 and 3000 N in this configuration. The variations are non-monotonic.

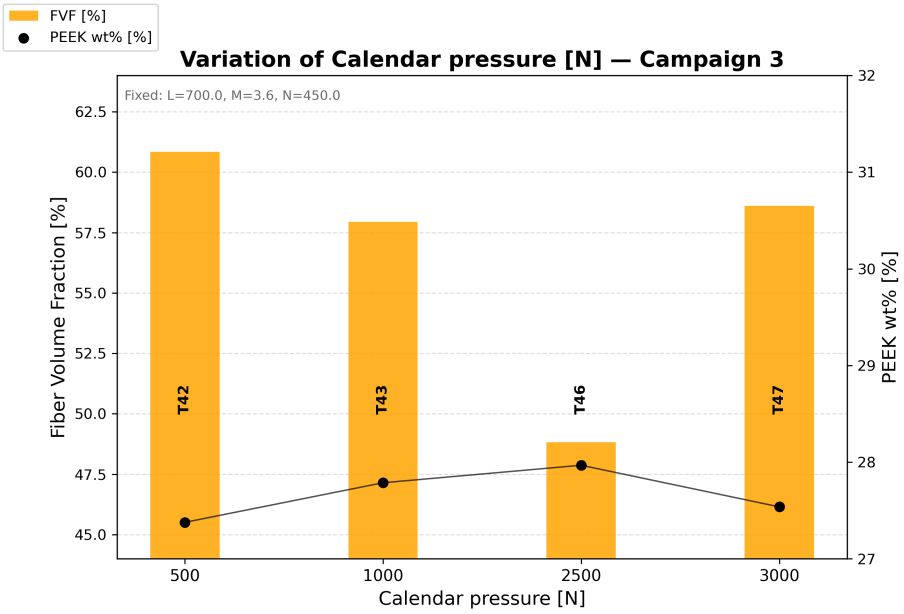


Figure 5.22: Influence of calendar pressure on FVF during Campaign 3 at fixed creel tension, line speed, and melting temperature. $\Delta\text{PEEKcontent(abs)} = 0.59\%$

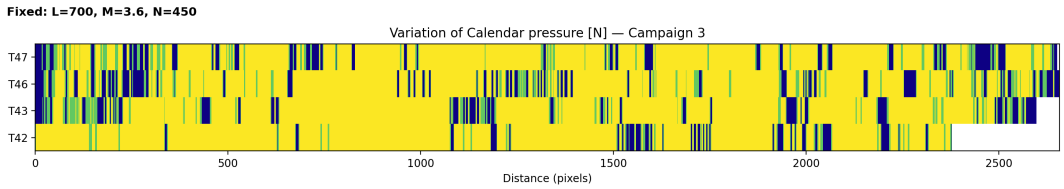


Figure 5.23: Effect of calendar pressure on tape morphology during Campaign 3 at fixed creel tension, line speed, and melting temperature (N = 450°C).

Table 5.14: Calendar pressure (Campaign 3, N = 450°C): quality metrics

Trial	Calendar pressure [N]	FVF [%]	Fractions (comp / int / PEEK) [-]	Transitions [/1000 px]	Mean run (comp.) [px]	Max run (comp.) [px]	Max run (PEEK) [px]
T47	3000	58.6	0.726 / 0.133 0.140	47.5	30.6	171	39
T46	2500	48.8	0.706 / 0.144 0.149	62.5	22.6	270	31
T43	1000	57.9	0.744 / 0.127 0.129	45.4	32.8	441	27
T42	500	60.8	0.838 / 0.079 0.082	37.8	44.3	313	21

The quality metrics show a clear contrast between Trials. T46 (2500 N) has the lowest FVF and highest axial transition in Table 5.14, despite a composite-rich fraction similar to T47 and T43. This may indicate stronger lateral transition associated with reduced FVF in T46.

For both melting temperature configurations, the barplots indicate no clear monotonic effect of calendar pressure on FVF. In contrast, the heatmaps show measurable Trial-to-Trial differences in axial transition and topology, but no consistent directional change with increasing pressure. These findings suggest that morphology variations do not result in a clear monotonic trend in FVF.

The limited sensitivity of FVF to calendar pressure aligns with the calendering stage's function in the process. Calendar pressure is applied after slurry impregnation and water evaporation, when the tape is already consolidated, even though the process occurs above the glass transition temperature of PEEK. Therefore, calendar pressure mainly influences consolidation features such as thickness uniformity, width stability, surface quality, and local polymer matrix redistribution, rather than the overall fibre-to-matrix ratio measured by mass-based FVF. To better evaluate the effects of calendar pressure, complementary characterisation methods are recommended, including quantitative microscopy for local microstructural analysis and qualitative optical observations for surface and thickness uniformity. These methods will provide more relevant insights into the role of calendar pressure during tape consolidation.

To assess what these heatmap signatures do (and do not) represent in terms of internal impregnation state, selected tapes were cross-checked by qualitative in process observations (Fig.5.24 and 5.25) and also by optical microscopy (Fig.5.26).

5.1.4 In-Process Qualitative Observations

To contextualise the observed variability, in-process pictures were used to document transient impregnation instabilities (e.g., intermittent percolation of the aqueous phase versus slurry transport), which cannot be fully controlled.

Figure 5.24 shows three typical impregnation states during manufacturing. The coloured regions represent distinct local flow states. The blue box highlights steady impregnation with faster slurry infiltration where the tow is split. The green box marks the transition from steady slurry transport on the right to complete particle filtration on the left. This results in a water-rich, particle-depleted flow, visible as strong water reflections on the left. This effect occurs when the tow becomes too thick because of poor spread or excessive overlap. This area is expected to become matrix-poor after drying. The orange box indicates full slurry breakthrough with local excess and backflow in the opposite direction to the main transport. This effect occurs when the tow is too thin or too spread. As a result, all the slurry passes through the tows, reaches the surface, and leaves the tape dry in the center. The pink box identifies a sharp boundary between dry fibres (left), fibres wetted mainly by water (middle), and fully soaked fibres (right).

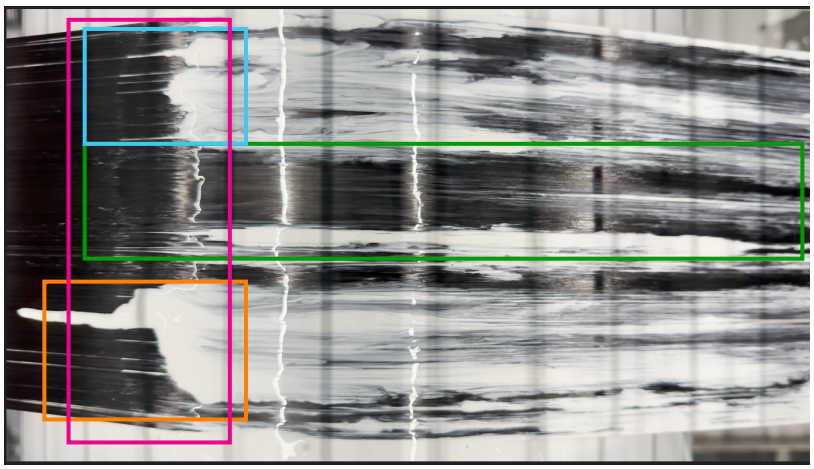


Figure 5.24: In-process photograph of the Kiss-roller impregnation zone shows spatial transition of impregnation and filtration states along the tow. Colored boxes indicate key regions referenced in the text.

Another in-process image after the drying bridge (Fig.5.25) shows a seemingly uniform surface impregnation, but a gap is already visible at the tow edge (orange). This demonstrates that proper tow alignment and overlap, established by the dry-spreading module, are essential for consistent tape formation, even if surface wet-out appears uniform.

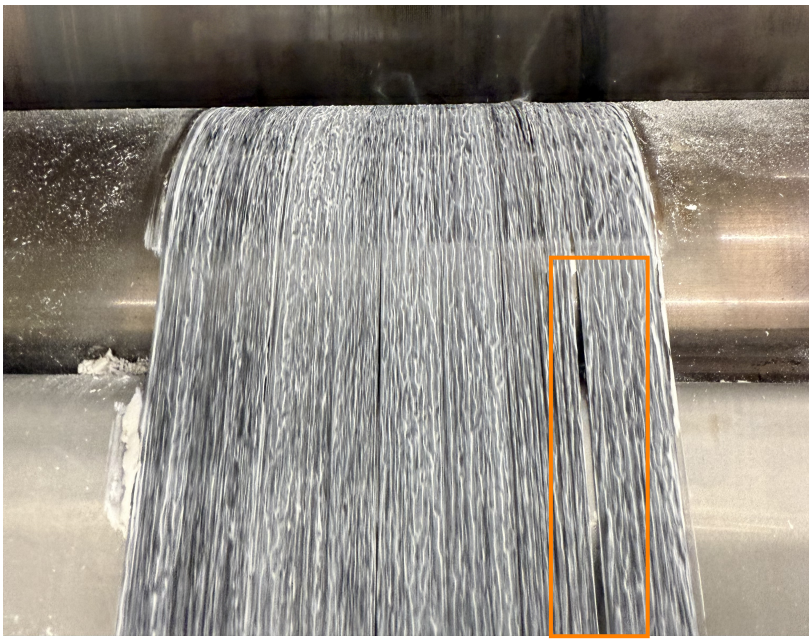
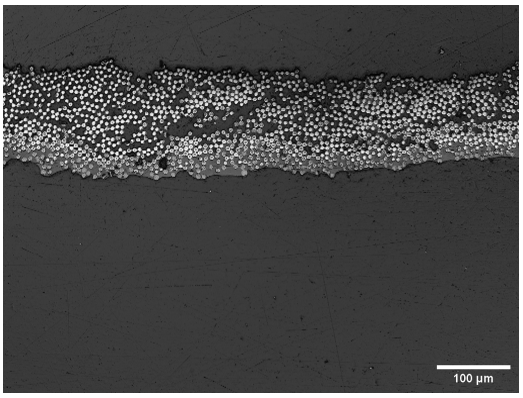


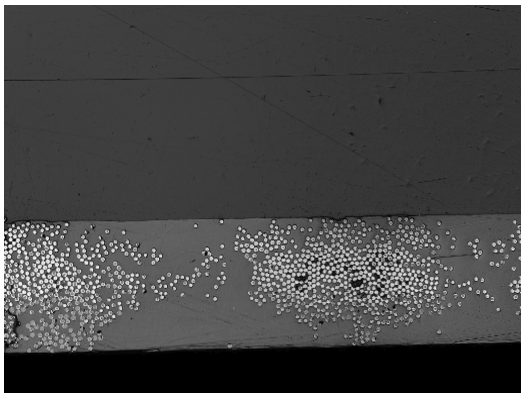
Figure 5.25: In-process picture after drying bridge showing a gap between tapes is already visible at the tape edge (orange).

5.1.5 Optical cross-section microscopy (microstructural cross-check)

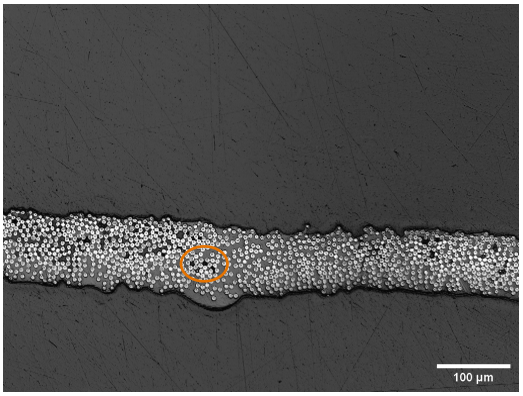
The following micrographs illustrate typical microstructural states and defects that may not be captured by heatmap metrics alone. The darker area around the image represents the coating resin. The light grey area is the solid PEEK and the white dots are individual carbon fibres with a diameter of 7 µm.



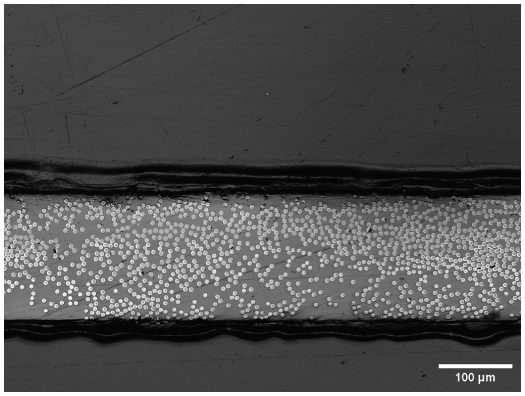
(a) Representative poorly impregnated tape, a typical case caused by bad impregnation (green box in Fig5.24



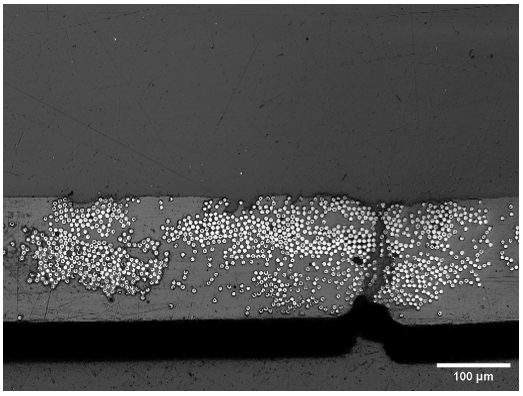
(b) Macroscopically uniform tape thickness, yet micro-scale fibre-/matrix-rich heterogeneities remain present. Despite that, This part of the tape still will be measured as composite rich (yellow).



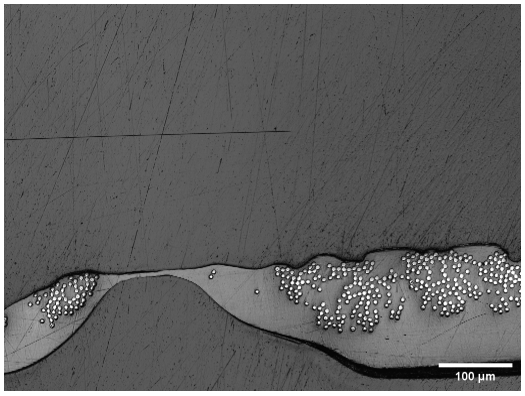
(c) Well impregnated with voids defect (orange) and thin thickness of 80um.



(d) Similar impregnation quality, but a thickness of 170um (illustrating thickness variability among "good" tapes).



(e) Local tape interruption: discontinuity of the impregnated region associated with a tape break.



(f) Local tape interruption: the impregnated region is discontinuous and only a thin PEEK ligament bridges the gap. This part of the tape will be measured as peek rich (blue). A typical case caused by a gap between tows (orange box in Fig5.25

)

Figure 5.26: Optical cross section microscopy highlighting limitations of the heatmap-based *composite-rich*/*PEEK-rich* classification.

5.2 Tape quality after production for Nip-roller

5.2.1 Slurry PEEK wt% variability at sampled positions and PSD signatures

Figure 5.27 and Table 5.15 summarise the measured slurry PEEK wt% at the sampled positions. As mentioned in section 4.2.3, the term T here is not related to trials conducted during campaigns. To avoid confusion in these results, the term "sample" will be used for this section. The representation and meaning of the sample are presented in the Figure 4.3.

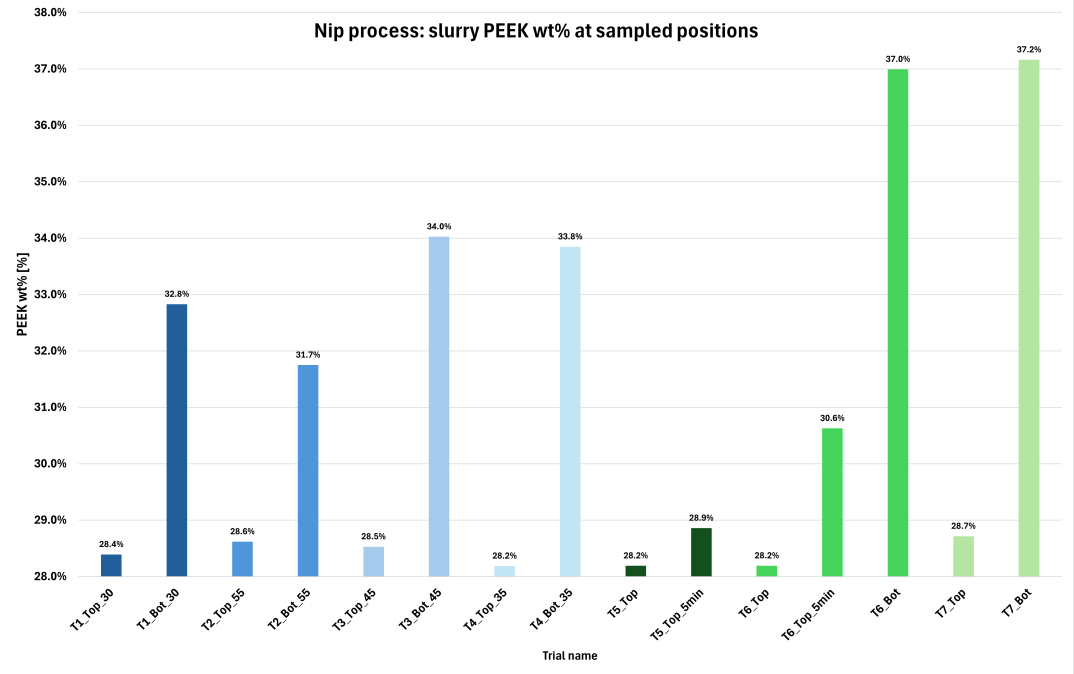


Figure 5.27: Slurry PEEK wt% at sampled positions

The *top* samples are clustered in a narrow range (28.2–28.7 wt%), indicating stable slurry composition at the top sampling height at the beginning of each run. Under the T1–T4 protocol (fixed $M = 3.6$ m/min, varying gap), the *bot* samples are consistently higher than the corresponding *top* samples. This pattern is observed and consistent with a local enrichment of the slurry collected at the bottom of the Nip when approaching a near-empty, starved condition where eddies were visually observed [33]. Across T1–T4, the *bot* values vary, but no monotonic trend with gap is observed in this dataset.

For the short-term *top* monitoring (T5 and T6), *top_5min* is higher than *top*. The *bot* values measured in T6 and T7 are higher than the *bot* range observed in T1–T4. However, comparisons involving T5–T7 are confounded by run-to-run differences such as refill, run-out, and missing *top_5min*, so they should be interpreted cautiously. Overall, the sampling results document spatial and temporal variability of slurry composition around the Nip in this dataset. PSD measurements are used next to assess whether the starved, eddy-forming condition preferentially retains specific particle populations within the nip.

Table 5.15: Summary of slurry sampling positions and measured PEEK weight fraction

Sample	**Gap [0.01 mm]**	M **[m/min]**	**Position**	**PEEK wt% [%]**
T1_Top_30	30	3.6	top	28.4
T1_Bot_30	30	3.6	bot	32.8
T2_Top_55	55	3.6	top	28.6
T2_Bot_55	55	3.6	bot	31.7
T3_Top_45	45	3.6	top	28.5
T3_Bot_45	45	3.6	bot	34.0
T4_Top_35	35	3.6	top	28.2
T4_Bot_35	35	3.6	bot	33.8
T5_Top	35	5.0	top	28.2
T5_Top_5min	35	5.0	top_5min	28.9
T6_Top	35	4.2	top	28.2
T6_Top_5min	35	4.2	top_5min	30.6
T6_Bot	35	4.2	bot	37.0
T7_Top	35	4.2	top	28.7
T7_Bot	35	4.2	bot	37.2

To assess whether the starved, eddy-forming *bot* condition is associated with a locally distinct particle population (beyond a pure concentration change), particle size distributions were compared using differential curves computed relative to the *top* sample of each run:

Across the analysed runs (Fig. 5.29), the *bot* samples show small but structured ΔPSD signatures with paired negative and positive minima/maxima around the main mode (order 10–30 µm). The magnitude remains limited (sub-percent in volume). Coarser signatures in the 100–300 µm range appear in specific *bot* samples. These deviations are treated as a potential measurement artefact because fibre residues were systematically present in the bottom slurry and could locally bias the detected large-size tail.

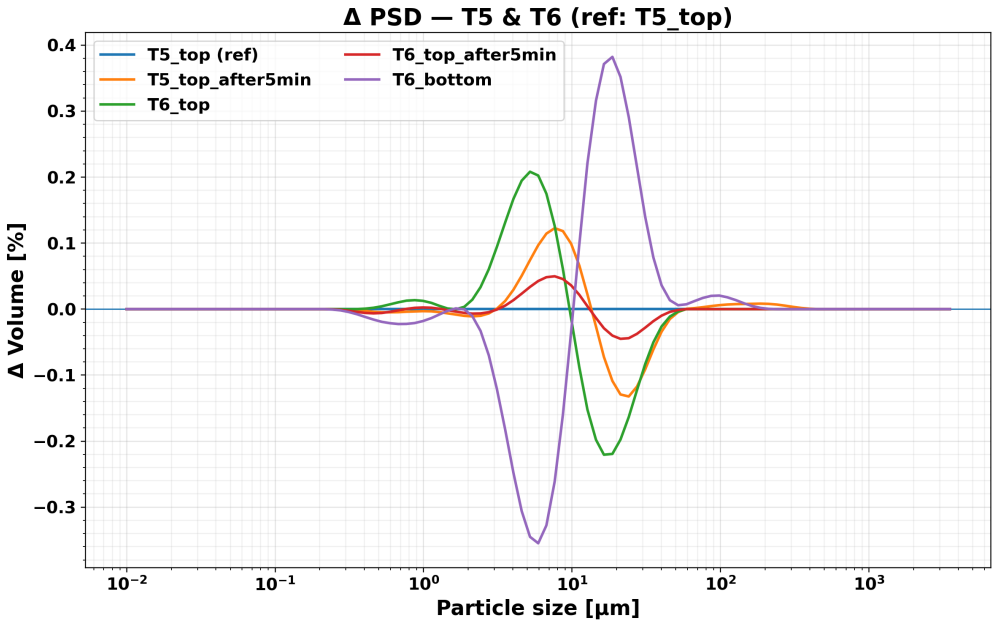
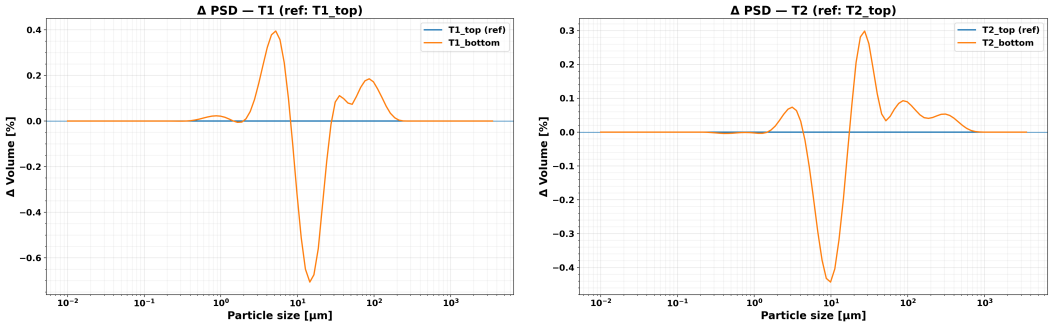
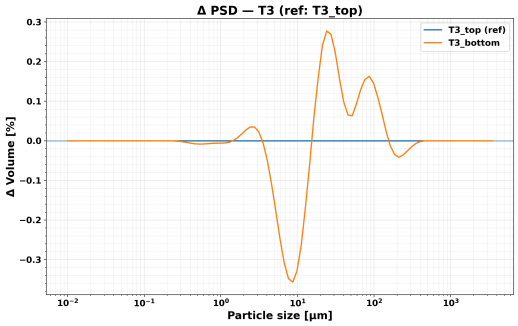


Figure 5.28: ΔPSD comparison for T5 and T6.

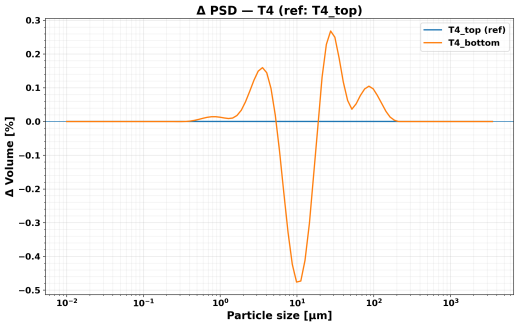


(a) T1

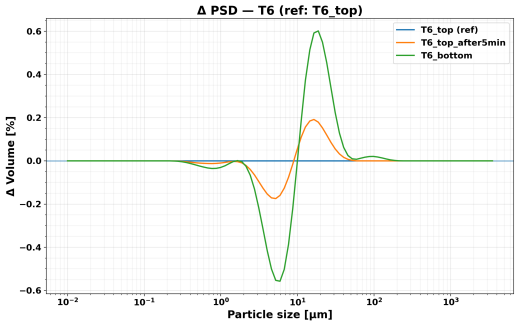
(b) T2



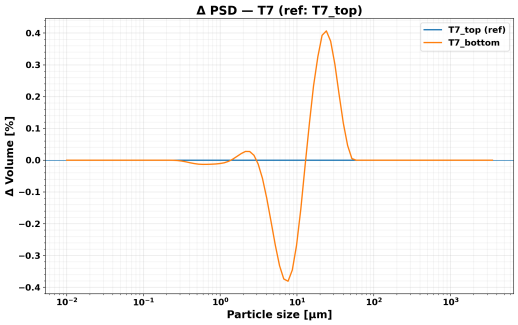
(c) T3



(d) T4



(e) T6



(f) T7

Figure 5.29: ΔPSD comparison with the *top* reference of each run.

The *bot* samples show higher slurry PEEK wt% than the corresponding *top* samples and exhibit structured (non-random) ΔPSD signatures. Taken together, this suggests that *bot* sampling can capture a locally distinct slurry state, rather than reflecting only a uniform concentration increase of the reservoir.

Because slurry viscosity increases with PEEK wt%, the higher PEEK wt% measured in the *bot* samples likely corresponds to a locally more viscous slurry. In a starved Nip with local recirculation, a more viscous slurry could retain particles more easily and favour the presence of coarser particles or agglomerates. This remains a tentative explanation because the ΔPSD changes are small, PSD was not repeated for each condition, and the *bot* samples are sensitive to local sampling effects.

In the Nip-roller dataset, short-term increases in slurry PEEK wt% are observed even when the *top* sampling height is constant, consistent with visually observed thickening during production. While evaporation may contribute, a plausible mechanism over 10–20 min

runs is rapid dewatering. The dry carbon tow entering the Nip may preferentially uptake the aqueous phase, locally increasing the solids fraction and viscosity without a clear change in reservoir level. Overall, conclusions are limited by single PSD measurements per condition and the uncertain representativeness of *bot* samples under starved-flow conditions. As an improvement, PSD tracking should be extended to the material after impregnation and drying to determine whether the observed ΔPSD signatures translate into persistent particle populations or are filtered during impregnation and drying.

5.2.2 Influence of machine parameters on FVF – Nip-roller

This subsection evaluates how the FVF varies with machine settings during nip-roller slurry impregnation. In all Nip Trials, $N = 420$ and $O = 1500$ were kept constant, while creel tension L and line speed M were varied. The Trial suffix _35 indicates the nominal nip-gap setting in tenths of a millimetre (e.g., _35 corresponds to 0.35 mm). The suffix V denotes a segment collected after a visually observed increase in slurry viscosity in the same run, and NS indicates that no dry-spreading bar was used. Table 4.3 in section 4.1 shows the Trials corresponding to the campaign for the Nip-roller.

Effect of line speed at creel tension $L = 0$ cN.

Figure 5.30 shows FVF as a function of line speed for the subset at creel tension $L = 0$ cN. No clear monotonic relationship between FVF and line speed M is observed across the dataset, partly because the Nip gap also varies between Trials (colour-coded bars). To allow a more consistent comparison, Table 5.16 reports the most comparable subset (gap 35). In this subset, the spread between repeated measurements at the same speed is similar to the differences between speed levels, which limits interpretation of a speed effect in this dataset.

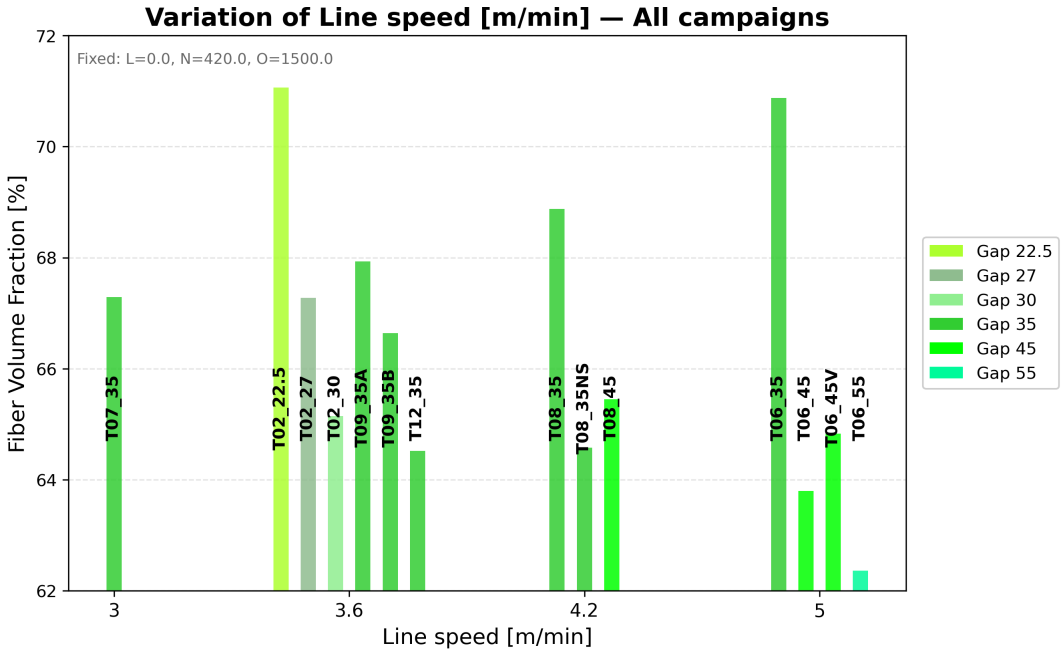


Figure 5.30: FVF as a function of line speed M for $L = 0$ cN. Bar colours indicate the nip-gap setting.

Table 5.16: Subset summary at fixed $L = 0$ cN and gap 35: FVF range (min–max) as a function of line speed M. n is the occurrence.

M (m/min)	n	FVF (min–max) [%]
3.0	1	67.3–67.3
3.6	3	64.5–67.9
4.2	2	64.6–68.9
5.0	1	70.9–70.9

The v annotation shows that FVF can change in a run after a visually observed increase in slurry viscosity. However, only one paired case is available, so this effect cannot be generalised.

Effect of creel tension at $M = 3.6$ m/min.

Figure 5.31 reports FVF as a function of creel tension at $M = 3.6$ m/min. FVF values remain scattered and no monotonic trend with L is apparent.

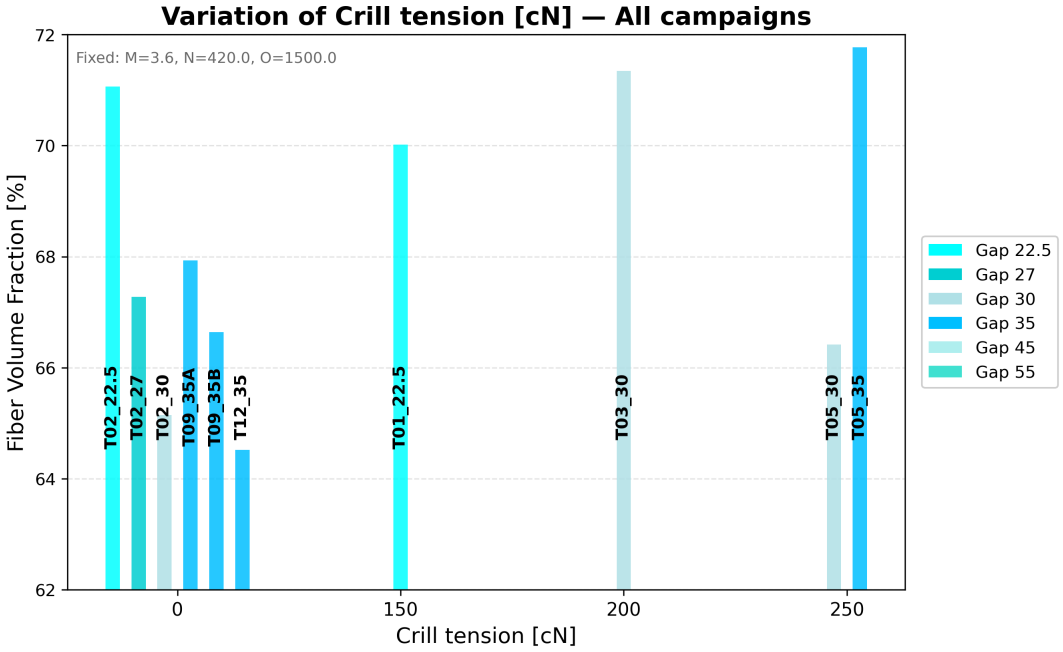


Figure 5.31: FVF as a function of creel tension L at fixed $M = 3.6$ m/min. Bar colours indicate the nip-gap setting.

Heatmaps are reported alongside the FVF bar plots to visualise lateral morphology and compute quantitative indicators. Figures 5.32 and 5.33 show the heatmaps for the line-speed and creel-tension, while the qaulity metrics table are available on Appendix C.3.

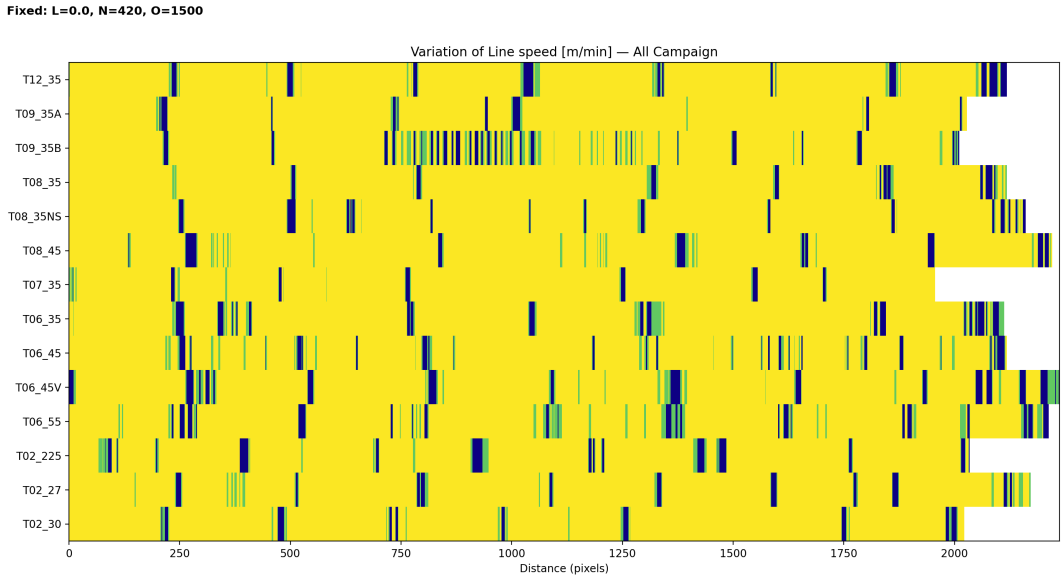


Figure 5.32: Lateral heatmap plot of tape morphology as a function of line speed (subset at $L = 0$ cN).

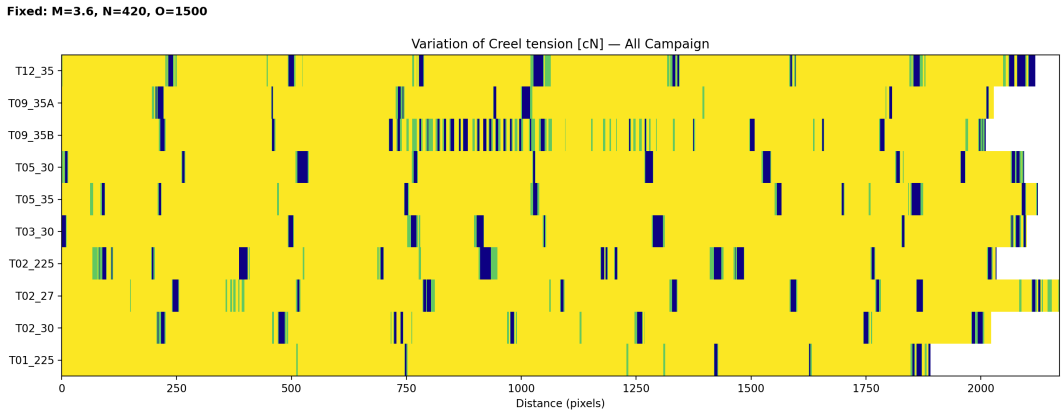
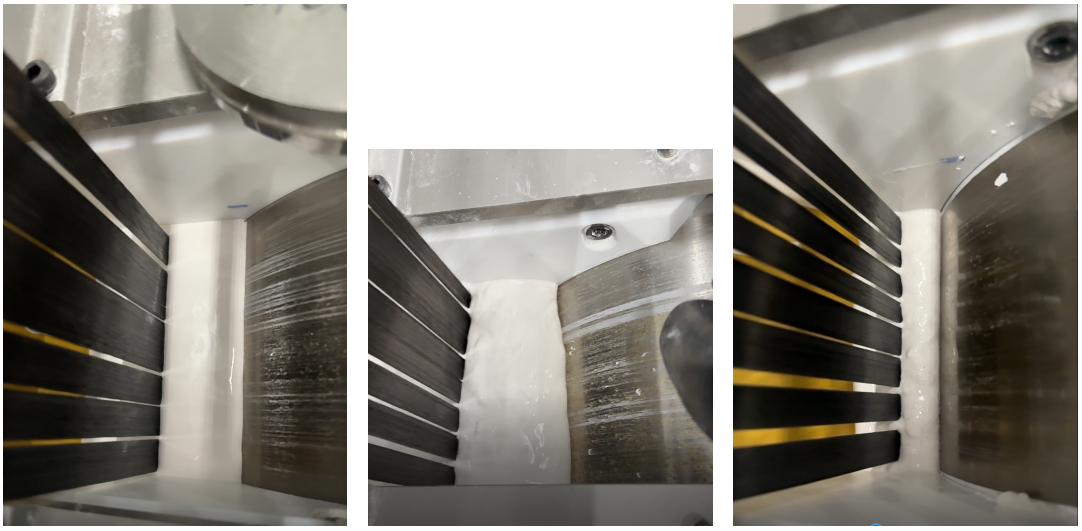


Figure 5.33: Lateral heatmap plot of tape morphology as a function of creel tension (subset at $M = 3.6$ m/min).

Overall, the morphology metrics provide limited additional insight beyond the FVF plots. The analysed tapes are predominantly composite-rich, but morphology varies substantially between Trials, even under nominally similar conditions (e.g., repeated gap 35 Trials in Table 5.16). Phase fractions, transition rates, and run-length statistics change notably from one Trial to another, consistent with the scatter in FVF and the absence of a clear parameter dependency in this dataset. The NS suffix records a processing condition, but it does not indicate a viscosity change. Because of limited repeats and confounding by nip-gap variations, the heatmap analysis mainly reflects experimental scatter rather than systematic dependencies on creel tension or line speed in this dataset. To assess what these heatmap signatures do or do not represent in terms of internal impregnation state, selected tapes were cross-checked by qualitative in process observations (Fig.5.34 and 5.36) and also by optical microscopy (Fig.5.26).

5.2.3 In-Process Qualitative Observations

To contextualise the Trial-to-Trial scatter and limited parameter sensitivity in the Nip dataset, in-process photographs, Figure 5.34 documented rapid changes in slurry state during a run. These observations show that the Nip can transition quickly from a smooth, fully flooded flow to a locally thickened, aggregate-rich and starved condition, consistent with the V annotations and the *bot* PEEK wt% values.



(a) Fresh slurry at the start of a run: smooth, uniform free surface (fully flooded).

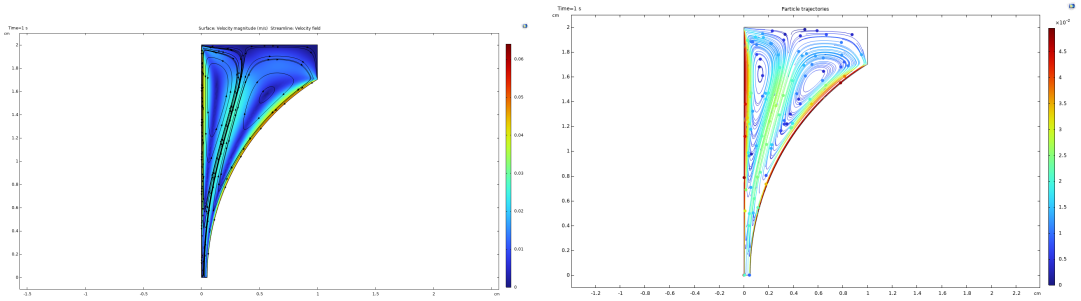
(b) After ∼10–15 min: thickened surface with recirculating powder agglomerates.

(c) Starved Nip condition: locally stagnant, highly viscous slurry with visible eddies/accumulation.

Figure 5.34: In-process photographs illustrating rapid changes in slurry state in the Nip (from fully flooded to thickened/starved conditions).

A simplified COMSOL model was developed to assess the plausibility of powder recirculation near the Nip and its potential role in particle retention and agglomeration. The purpose is not quantitative prediction, but a conceptual, hypothesis-testing model to support interpretation of in-process observations. Despite deliberate simplifying assumptions in geometry, rheology, and boundary conditions, the simulation qualitatively reproduces several key flow features observed experimentally, such as recirculation structures and stagnant zones. This lends mechanistic support to the proposed interpretation. The model should be seen as showing qualitative agreement rather than serving as a predictive tool. Reliable predictions would require further refinement, calibration, and validation against dedicated measurements.

The representation is a 2D half-model used for qualitative interpretation. The vertical wall on the left represents the carbon tows, while the curved boundary on the right represents one of the Nip rollers; the inlet is at the top and the outlet at the bottom. The tows are mechanically driven through the nip, and a no-slip condition is imposed at the tape/roller interface, so that the local relative velocity at the contact is zero. The simulation considers a single-phase slurry flow; particle paths are visualised using passive, non-interacting tracers (no agglomeration model). In addition, tows are modelled as solid and not porous media. The model is illustrative and not calibrated for quantitative prediction. Complementary images of the transient state of particles behaviour between 0 to 1 sec. are available in Appendix C.4.

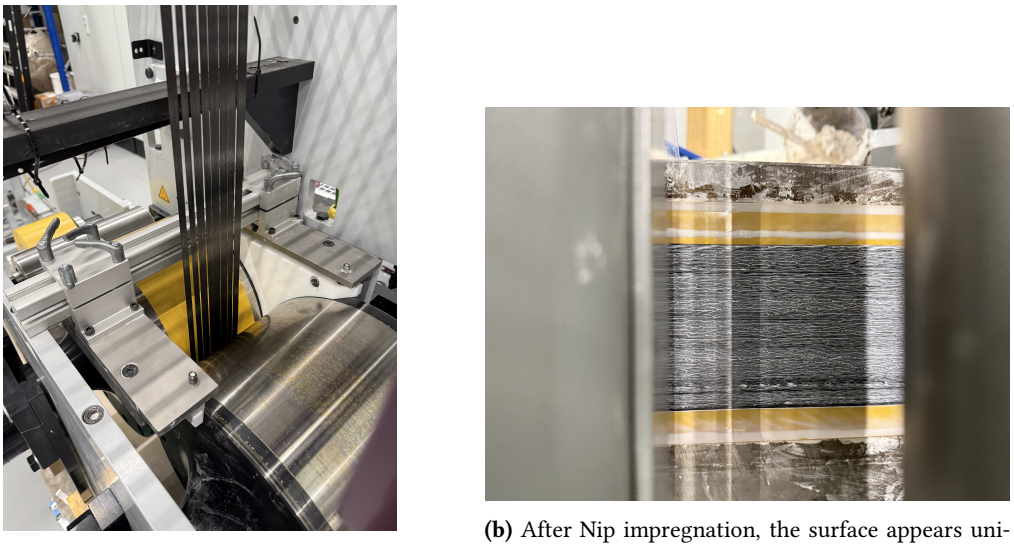


(a) Qualitative COMSOL result for the Nip inlet (2D half-model): velocity magnitude (colour map) with streamlines (black). The flow field shows recirculation cells and extended low-velocity regions, supporting the plausibility of particle retention near the inlet.

(b) Particles tracer trajectories in the same qualitative COMSOL model (snapshot at $t = 1$ s). Several trajectories remain trapped in recirculation loops, indicating increased residence time in the inlet region. Tracers are non-interacting and do not represent agglomeration.

Figure 5.35: Qualitative Comsol model

In addition to slurry-state changes, the Nip route appears sensitive to tow spreading and overlap, with a more "binary" behaviour (well-spread tow without overlap) (Fig.5.36). This provides a qualitative explanation for the regularly spaced banding observed in heatmaps such as T12_35 or T02_27 (Fig5.33), where individual tow remain visible as alternating *composite-rich*/*PEEK-rich* stripes.



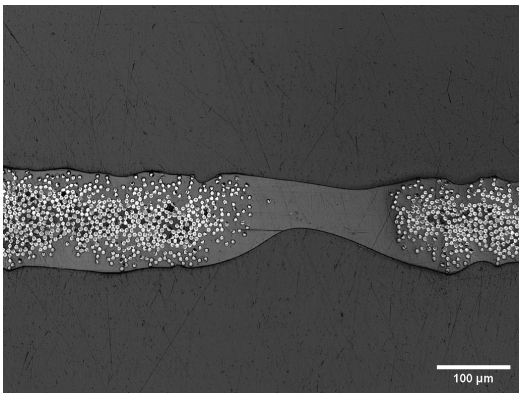
(a) Tows entering the nip: limited spreading and incomplete overlap between adjacent tows.

(b) After Nip impregnation, the surface appears uniform, yet tow boundaries remain visible, indicating persistent tow transitions.

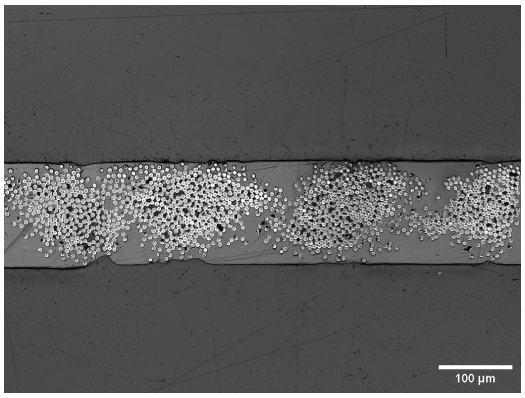
Figure 5.36: In-process pictures illustrating tow spreading/overlap sensitivity and its link to banded tape morphology in the Nip-roller route.

5.2.4 Optical cross-section microscopy

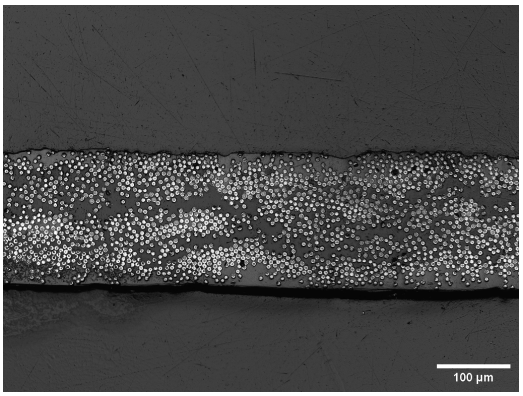
The following micrographs illustrate typical microstructural states and defects that may not be captured by heatmap metrics alone.



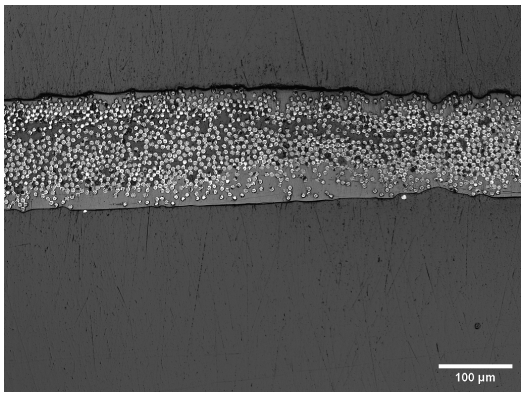
(a) Representative PEEK-rich region (polymer-enriched zone with distinct contrast, in represented in blue on the heatmap).



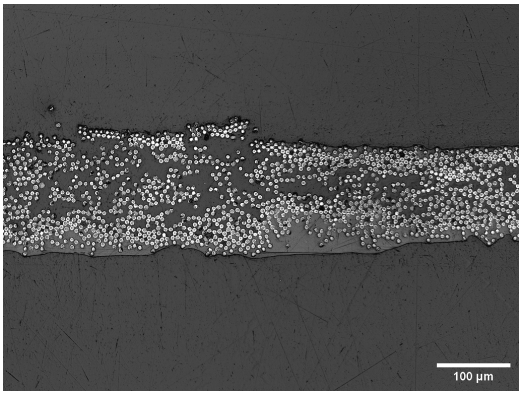
(b) Macroscopically uniform tape thickness, yet micro-scale fibre-/matrix-rich heterogeneities remain present.



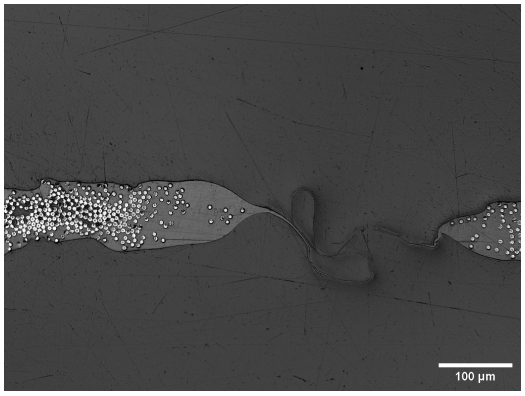
(c) Constant tape thickness with poor through-thickness impregnation: matrix concentrated near the surfaces and a dry core. Despite that, This part of the tape still will be measured as composite rich (yellow).



(d) Same macroscopic appearance, but locally insufficient impregnation persists (surface-rich matrix and dry core).



(e) Extremely dry/under-impregnated tape, associated with high brittleness and mechanical fragility.



(f) Local tape interruption: the impregnated region is discontinuous and only a thin PEEK ligament bridges the gap.

Figure 5.37: Optical cross section microscopy cross-check highlighting limitations of the heatmap-based *composite-rich*/*PEEK-rich* classification.

Chapter 6

Conclusion & Recommendations

6.1 Kiss-roller vs Nip-roller: reading framework, key results, and implications

6.1.1 Comparison framework and interpretation cautions

This work compares two slurry-based impregnation routes to manufacture ultrathin UD carbon/PEEK tapes: kiss-roller and nip-roller. In this dataset, the kiss-roller process shows clear parametric trends in fibre volume fraction and lateral quality metrics. The nip process, however, is dominated by inter-trial variability that masks the effects of line speed and creel tension when conditions are not strictly repeated. (Fig. 5.10–5.18, Tab. 5.8, Fig. 5.30–5.31, Tab. 5.16)

The comparison is structured around a shared causal chain: machine parameters → slurry state/deposition mechanics → lateral quality metrics → FVF. The methodology concerning lateral metrics is identical for both processes: phase fractions (composite-rich / intermediate / PEEK-rich). The transition rate (transitions/1000 px) is the primary metric of lateral transition for its readability and robustness as a global indicator. Run-length statistics are reported as complementary descriptors to capture segment structure (means and maxima). The objective is not to rank the processes, but to clarify trade-offs in controllability, robustness, and reproducibility across FVF and lateral transition.

Two cautions bound the conclusions. First, FVF is an integrated mass-based quantity and can remain high despite local heterogeneities. Second, heatmap-derived metrics quantify lateral transition within the ROI but alone do not prove through-thickness impregnation. Cross-section validation is required for any conclusion about core impregnation. (Fig. 5.26, 5.37]

6.1.2 Kiss-roller process: dominant sensitivities and the lateral transition-FVF link

In the kiss-roller process, deposition is governed by a slurry film carried by the roller and transferred to the tow at the Kiss contact. Line speed controls the adequate tow film contact time and the opportunity for transfer or wetting. Creel tension modulates the mechanical and geometrical state of the tow, such as spreading or compaction, at the moment of transfer (2.4.1).

In Campaign 2, increasing line speed from 3.0 to 3.6 m/min systematically reduces FVF for the tested tensions (Tab. 5.8). For the detailed conditions, this FVF decrease is associated

with increased lateral transition: at $L = 500$ cN, the transition rate increases, while phase fractions shift towards more intermediate and PEEK-rich (Tab. 5.5). A similar pattern is observed at $L = 1000$ cN (Tab. 5.7).

Within the explored window, these observations support the idea that increasing speed is associated with higher lateral transition and lower FVF. This matches reduced tow-film contact time or lower transfer efficiency as speed increases. However, these mechanisms are not directly measured here and should be considered interpretive hypotheses.

An important interaction concerns creel tension: the magnitude of the FVF decrease induced by increasing M becomes smaller as L increases (from 4.7 pp to 3.5 % between 500 and 1000 cN) (Tab. 5.8). In this dataset, this suggests that higher tension reduces the speed sensitivity of FVF. A second campaign is needed to validate or invalidate this trend, taking into account smaller tension variations between 500 and 1000 cN. Finally, increasing calendar pressure does not show an apparent monotonic effect on FVF within the tested ranges; a conservative reading is that FVF is weakly sensitive to local redistribution effects and/or that variability related to slurry state dominates the expected effect.

6.1.3 Nip- roller process: scatter, inlet regimes, and limits of parametric isolation

In the Nip-roller dataset, FVF is scattered and shows no exploitable monotonic trend with creel tension (at fixed M) or with line speed (at $L = 0$) (Fig. 5.31, Fig. 5.30). This lack of trend aligns with the low number of repetitions and the co-variation of other factors, especially inlet conditions and slurry state, across non-identical trials (Tab. 5.16).

Focusing on the most comparable subset (gap 35, $L = 0$), FVF spans 64.5–67.9% at $M = 3.6$ m/min ($n = 3$) and 64.6–68.9% at $M = 4.2$ m/min ($n = 2$) (Tab. 5.16). The spread within a given speed is similar to the difference between speeds, so a monotonic effect of M cannot be reliably resolved in this window. Consistently, the lateral metrics also differ markedly between nominally similar repeats (e.g., transition rate at $M = 3.6$m/min, gap 35), suggesting the observed scatter reflects different deposition states rather than minor measurement noise (Tab. C.3).

Beyond this, the Nip-roller process provides in-process observations. Rapid state transitions are observed at the inlet, shifting from a fully flooded state to a thickened or aggregate-rich state, then to a starved condition (Fig. 5.34). This dynamic plausibly explains inter-trial dispersion and intra-run sensitivity annotated with V (T06_45 vs T06_45V) (Tab. C.3 and Chap. 2.4.1). Several cases also show sensitivity to tow spreading quality, such as overlap, which can lead to a regularly spaced banded morphology, as shown in chapter 5.2.3).

Finally, microstructural validation highlights a major methodological limitation: macroscopic appearance and heatmap classification are not sufficient to ensure internal impregnation, as shown in Figures 5.37 and 5.26.

6.1.4 Comparable vs non-transferable: scope of the comparison

FVF and lateral metrics (fractions, transition rate, run lengths) are comparable across processes because they are defined and computed consistently. They allow evaluation, for both routes, of how the matrix distributes laterally and how this transition is associated with FVF variations.

In contrast, interpreting machine parameters is not directly transferable. In Kiss-roller, increasing line speed is associated, in Campaign 2, with a systematic decrease in FVF and an increase in lateral transition; in Nip-roller, the effect of line speed is masked by scatter and by inlet state transitions observed in-process. (Fig. 5.10 and 5.30. Similarly, creel tension modulates speed sensitivity in Kiss-roller but does not produce an exploitable trend in Nip-roller within this dataset (Tab. 5.8 and Fig. 5.31).

6.2 Limitations and robustness considerations

The conclusions of this chapter should be interpreted within the context of process and analysis limitations. Possible slurry-state drift during a campaign (composition/viscosity), along with the lack of strict repetitions at identical parameters for several points, reduces the strength of "parameter $\rightarrow$ response" inferences when the expected effect matches inter-trial variability (Sec. 2.6). Also, FVF is an integrated quantity and is not a qualification criterion for local uniformity. Finally, heatmap-derived metrics should be interpreted as ROI-level diagnostics of lateral transition, which limits the scope of comparisons when a through-thickness conclusion is desired.

For Nip-roller in particular, the main limitation is identifiability. When inlet conditions switch between regimes (flooded/flooded more viscous) and trials are not strictly repeated, the isolated effect of Line speed M or Creel tension L can be masked by more dominant slurry state changes (Fig 5.27).

A final limitation concerns transferability across manufacturing scales. Since morphing performance is assessed at the laminate level, the present conclusions should be considered tape- or feedstock-level indicators. Consolidating a laminate by methods such as hot-press forming may reconfigure fibre distribution, void content, alignment, thickness variations, and crystallinity, so the link between tape-level indicators and laminate response is not straightforward.

6.3 Perspectives and recommendations

The perspectives follow directly from the results and limitations. Making the processes optimisable requires controlling the slurry state and, for Nip-roller, locking the inlet regime before interpreting the effect of line speed M and creel tension L.

For kiss-roller, the data support or suggest joint optimisation of line speed and creel tension, provided slurry state is stabilised and tracked during parametric mapping. For calendar pressure, the absence of a monotonic trend in FVF suggests shifting evaluation to metrics sensitive to local effects such as redistribution, surface state, or thickness, rather than relying on FVF.

For Nip-roller, the priority is to control and systematically document the inlet regime (flooded or starved) and the quality of spreading or overlap. Then, repeat strictly identical trials to quantify residual dispersion before concluding Line speed M or Creel tension L (App. C.1, 2.4.1). For qualification, lateral quality metrics as ROI-level diagnostics of lateral transition, and complement them with targeted microstructural validation when core impregnation governs mechanical reliability.

To improve tow spreading upstream of the Nip impregnation, a detensioning mechanism can be implemented. Detensioning can be achieved by using a cam to impose a controlled, approximately sinusoidal modulation of the effective tow path length. This creates periodic slack phases during which the tension can approach zero. These low-tension windows are expected to promote filament redistribution on the spreader, reducing overlap and improving inlet stability. Lower tow tension is also expected to enhance Nip-induced spreading. Under high axial tension, the tow is mechanically constrained: filament mobility and lateral slip are limited, and the normal pressure in the Nip is more likely to produce compaction than lateral opening. By periodically relaxing this axial constraint through the rotating-cam slack phases, the Nip pressure may translate more effectively into lateral filament rearrangement and tow opening. The implications for impregnation quality remain a working hypothesis that should be validated experimentally.

In summary, Kiss-roller shows relatively robust sensitivity to line speed between 3.0 and 3.6 m/min, depending on L). In Nip-roller, the scatter at similar parameters (for example, 64.5 to 68.9% at gap 35, $L = 0$) indicates that, in this dataset, inlet-regime stability and repeatability dominate identifiability of the effects of Line speed M and Creel tension L. Finally, in the outlook of future thin ply morphing applications, control relies on keeping the FVF at about 60%, limiting lateral transition in the region of interest, and using targeted microstructural validation when core impregnation affects mechanical reliability.

Appendix A

Materials Data Sheets

A.1 Toray Carbon Fibers

T700S datasheet: https://www.toraycma.com/wp-content/uploads/T700S-Data-Sheet-4.22.2025.pdf

T800S datasheet: https://www.toraycma.com/wp-content/uploads/T800S-Technical-Data-Sheet-1.pdf

TORAYCA Carbon Fibre for Applications: https://www.toraycma.com/products/carbon-fiber/

A.2 PEEK Matrix (Vicote 700 Series)

Datasheet: https://www.victrex.com/en/downloads/datasheets/vicote-700-series

A.3 Additives

PEG-10000: https://www.sigmaaldrich.com/NL/en/product/sial/p6667

Xanthan gum : https://www.bol.com/nl/nl/p/van-beekum-specerijen-xanthaangom-strooibus-69300000082028425/?s2a=&bltgh=lFKDQuSxo7FNmVcFBThMhQ.4_31_32.33.FeatureOptionButton#productTitle

Triton X-100: https://www.sigmaaldrich.com/NL/en/product/sial/x100

Appendix B

Processing and equipment

B.1 Test plan for tape line manufacturing

The test plans presented here are those used for manufacturing. Changes were made during the process. This is why the parameters must be checked in the Fibre_Volume_Fraction Excel file available in the analysis folder, Fibre_Volume_fraction_FVF on GitHub (link available in the Imprint). The paper test plans with modifications are available in the tape lab binder.

B.2 Test plan - Kiss roller

Tapeline Test Plan

Date: 2025-09-30
Prepared by: Shailee Upadhyay, Joël Monney

Test Overview

Field	Details
Test Name	300925-DPR-CF-PEEK-1
User(s)	Shailee Upadhyay, Joël Monney
Main Operator	Sharon Chu
Project Name	LiT / STC
Project Code	L20305
Machine Configuration	DPR - short belt
Planned Dates	Start: __2025-09-30__ End: ___2025-10-09____
Experiment Goal	Baseline DPR + Manufacturing CF/PEEK tapes with different parameters

Machine Configuration Diagram

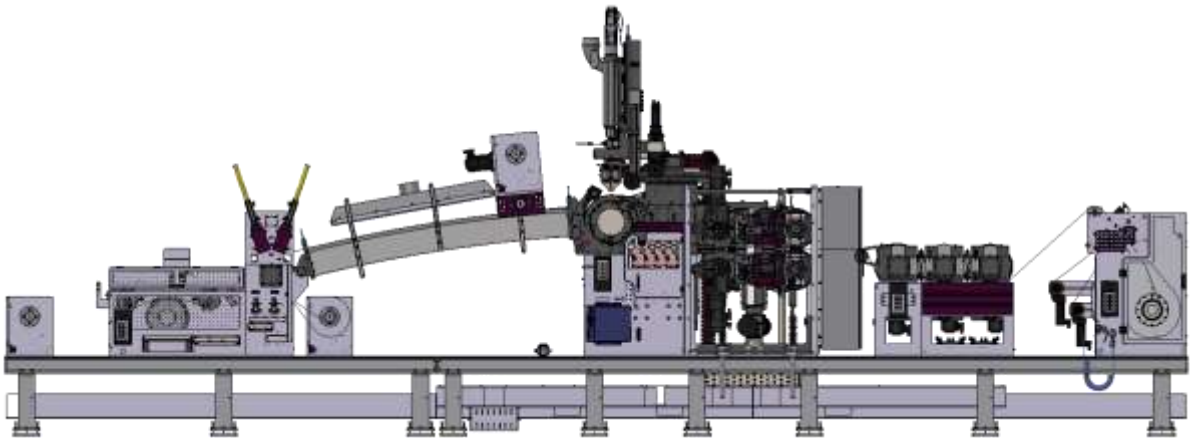


Figure 1: TPR Tapeline Configuration

Machine Setup Parameters

1. **Materials**

Type	Name	Tex (g/km)	Sizing	Density (g/cm^3)	Number roving	Melting temperature (°C)

Fiber	CF – T700-12K 60E	12000	Epoxy	1,8	8	-
Polymer	Victrex PEEK 150G	-	-	1,38	-	335-345

2. Creel Setup

- Spool Placement in Creel:

7,8,9,10 B and 5,7,8,10 C → to be discussed with Sharon

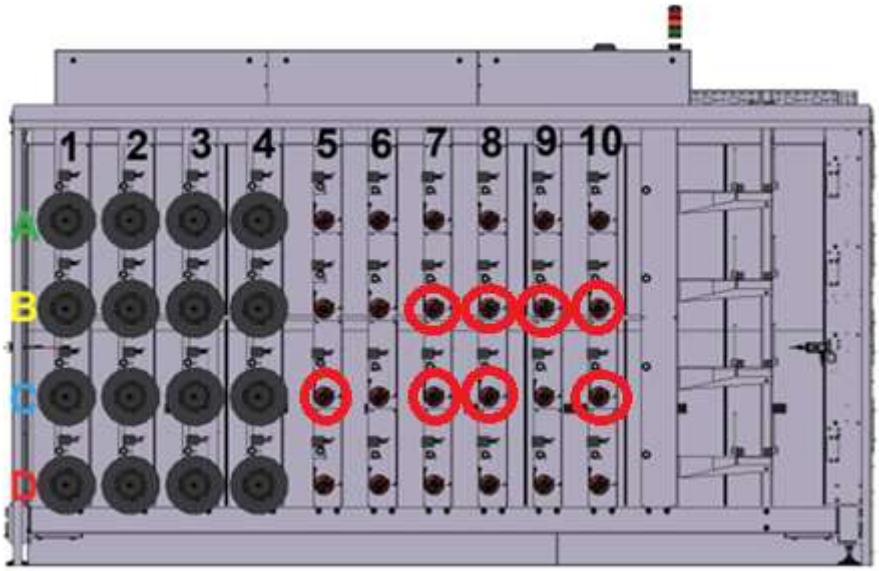


Figure 2: Spool placement

- Tension Settings per Spool:

500cN – at the start of trial

- Notes on Handling:

Make sure no there is no twist on the fibers from the spool to the spreading bars.

3. Spreading Bars

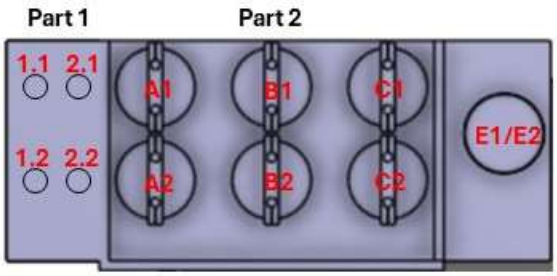


Figure 3: Tow spreading bars. Part 1 for roving spacing. Part 2 for roving spreading.

- Positioning (part1):
  Roving will be stacked as 2 layer
  4 roving on the top bar and 4 roving on the bottom bar.
  Roving pass from the top of bar 1.1 and 1.2, then on bottom of bar 2.1 and 2.2.
- Spacing (part1): Need for spacers to be verified based on staggering

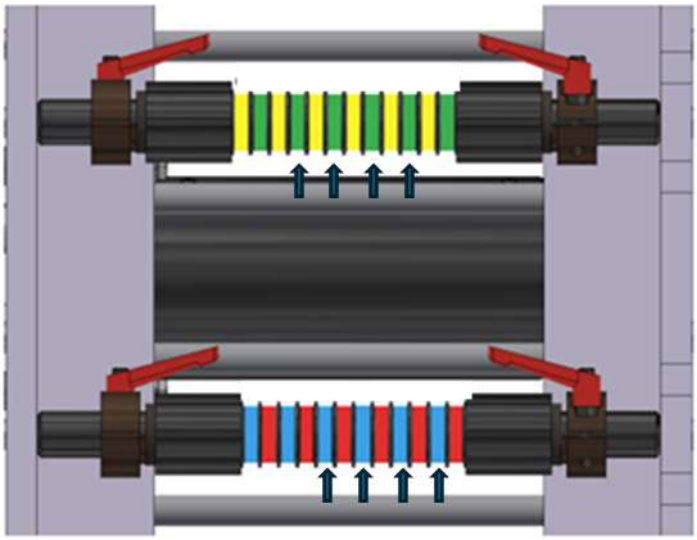


Figure 4: Placement and spacing of roving on bars 1.1 and 2.1

- Spreading Angles (part2):

SETUP 1: Start with no dry-spreading for Baseline + spreading through just kiss-roller. (Baseline)

SETUP 2: After initial trial, change the angles as follows:

Sections	Spreading angle
A1 & A2	320
B1 & B2	140
C1 & C2	320 & 50
E1 & E2	140

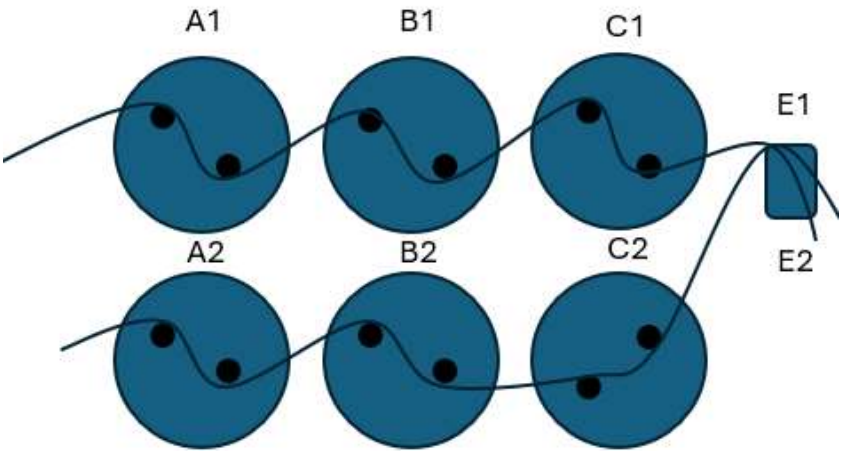


Figure 5: Roving direction on the spreading bars (part 2)

4. Temperature Control Zones

Zone	Set Temperature (°C)
Spreading bars: E1 & E2	200 (to be verified)
F1	250
Extruder: T1	NA
Extruder: T2	NA
Extruder: T3	NA
Extruder: T4	NA
Melt Pipe: K	NA
Die: N	NA
Impregnation Roll: M	420
Post spreading: I	420
Calander	110

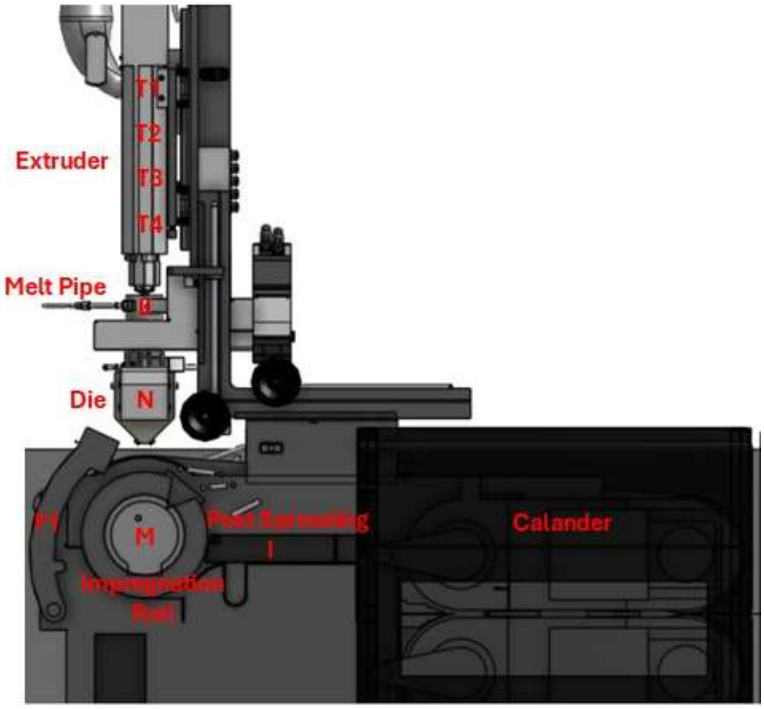


Figure 6: Temperature control Zones

5. **Other parameters**

- Calander pressure: 500Nm (initial)
    - Note change if done:_____
- Pulling speed: 1.8m/min (at the start)
- Kiss-roller speed: No offset

Stabilization Time Procedure

- **Stabilization Checks**:
    - Creel tension stability
    - Fiber pulling without twisting
- **Initial Stabilization**: 30 minutes before any changes
- **Parameter Change Stabilization**: 15 minutes
- **Observation Time After Stabilization**: 15 minutes
- **Notes on Stabilization *:***
    - Measured temperatures (every 10min):_____
    - Tape visualization:_____

Experimental Plan

Spreading and Tension would be measured during all experiments.

Variable Parameters

- Fiber tension (cN): 1000, 500, 250, 150
- Pulling speed m/min: 1.2, 1.8, 2.4, 3, 3.6,4.2, 5

Plan 1:

After Baseline, change dry spreading angles. Below observations to be made with dry spreading:

Trial	Dry spreading	Fiber tension (cN)	Line speed (m/min)	Impregnation roller temperature	Calendar pressure
1	Setup 1 (BL)	500	1.8	420	500
2	Setup 1 (BL)	500	3	420	500
3	Setup 1 (BL)	500	2.4	420	500
4	Setup 1 (BL)	500	3.6	420	500
5	Setup 1 (BL)	500	1.2	420	500
6	Setup 1 (BL)	500	5	420	500
7	Setup 1 (BL)	500	4.2	420	500
8	Setup 1 (BL)	700	Speed # 1 (selected from above)	420	500
9	Setup 1 (BL)	250	Speed # 1	420	500
10	Setup 1 (BL)	1000	Speed # 1	420	500
11	Setup 1 (BL)	850	Speed # 1	420	500
12	Setup 1 (BL)	1300	Speed # 1	420	500
13	Setup 1 (BL)	400	Speed # 1	420	500
14	Setup 1 (BL)	500	Speed # 1	420	500
15	Setup 2	500	1.8	420	500
16	Setup 2	500	3	420	500
17	Setup 2	500	2.4	420	500

18	Setup 2	500	3.6	420	500
19	Setup 2	500	1.2	420	500
20	Setup 2	500	5	420	500
21	Setup 2	500	4.2	420	500
22	Setup 2	700	Speed # 1	420	500
23	Setup 2	250	Speed # 1	420	500
24	Setup 2	1000	Speed # 1	420	500
25	Setup 2	850	Speed # 1	420	500
26	Setup 2	1300	Speed # 1	420	500
27	Setup 2	400	Speed # 1	420	500
28	Setup 2	500	Speed # 1	420	500
29	Setup 2	700	Speed # 2	420	500
30	Setup 2	250	Speed # 2	420	500
31	Setup 2	1000	Speed # 2	420	500
32	Setup 2	850	Speed # 2	420	500
33	Setup 2	1300	Speed # 2	420	500
34	Setup 2	400	Speed # 2	420	500
35	Setup 2	500	Speed # 2	420	500
36	Setup 2	Best for setup 2	Best for setup 2	450	500
37	Setup 2	Best for setup 2	Best for setup 2	Best of 420/450	1000
38	Setup 2	Best for setup 2	Best for setup 2	Best of 420/450	1500
39	Setup 2	Best for setup 2	Best for setup 2	Best of 420/450	2000
40	Setup 2	Best for setup 2	Best for setup 2	Best of 420/450	2500

41	Setup 2	Best for setup 2	Best for setup 2	Best of 420/450	3000

Notes: Any changes based on tapeline observations will be updated in this document.

B.3 Test plan - Nip roller

Tapeline Test Plan

Date: 2025-09-30

Prepared by: Shailee Upadhyay, Joël Monney

Test Overview

Field	Details
Test Name	101125-NR-CF-PEEK-1
User(s)	Shailee Upadhyay, Joël Monney
Main Operator	Sharon Chu
Project Name	LiT / STC
Project Code	L20305
Machine Configuration	NR - short belt
Planned Dates	Start: __2025-11-10__ End: ___2025-11-17____
Experiment Goal	Manufacturing CF/PEEK tapes with different parameters

Machine Configuration Diagram

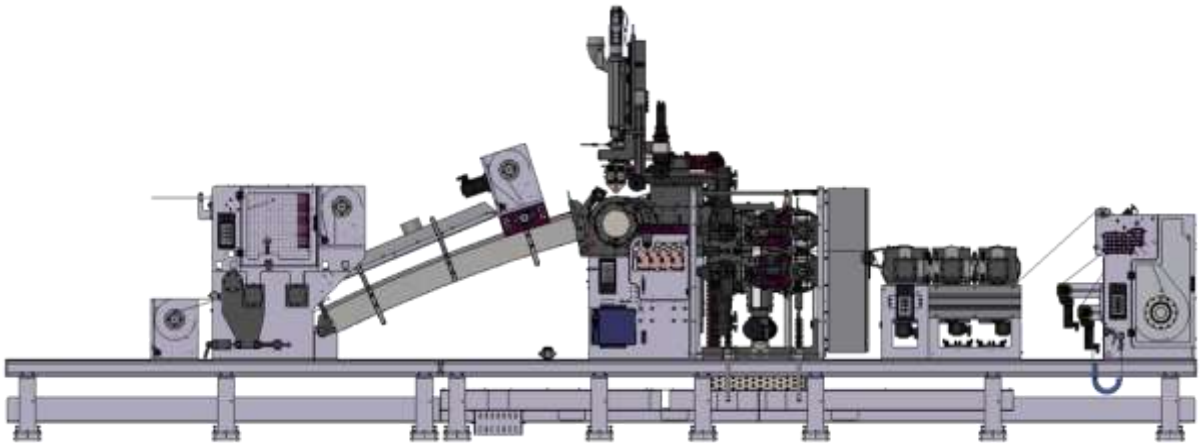


Figure 1: NRR Tapeline Configuration

Machine Setup Parameters

1. **Materials – 27% and 30% wt PEEK slurry, no thickener**

Type	Name	Tex (g/km)	Sizing	Density (g/cm^3)	Number roving	Melting temperature (°C)

Fiber	CF – T700-24K 60E	24000	Epoxy	1,8	8	-
Polymer	Victrex PEEK 150G Slurry composition initial: 30% PEEK + 0.5 g/L Xanthan gum	-	-	1,38	-	335-345

2. Creel Setup

- Spool Placement in Creel:

7,8,9,10 B and 5,7,8,10 C → to be discussed with Sharon

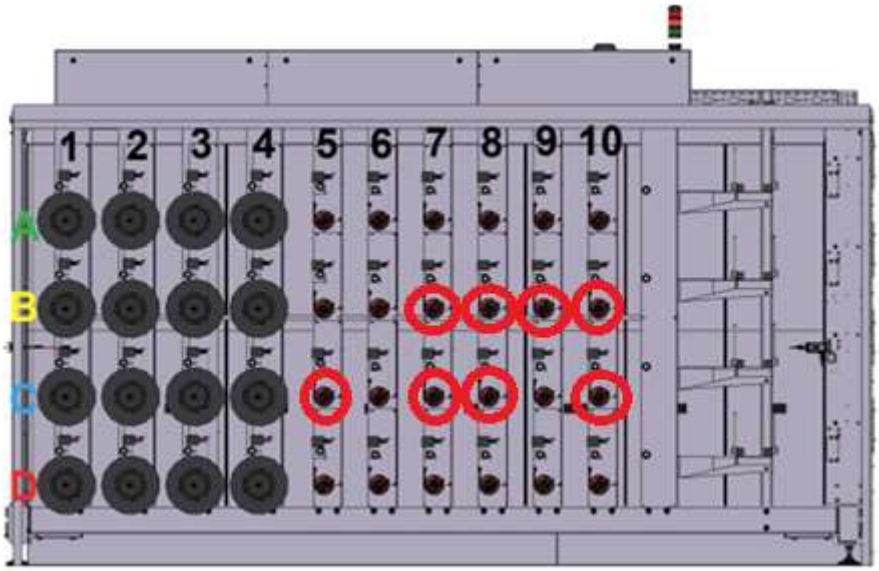


Figure 2: Spool placement

- Tension Settings per Spool:

50cN – at the start of trial

- Notes on Handling:

Make sure no there is no twist on the fibers from the spool to the spreading bars.

3. Spreading Bars

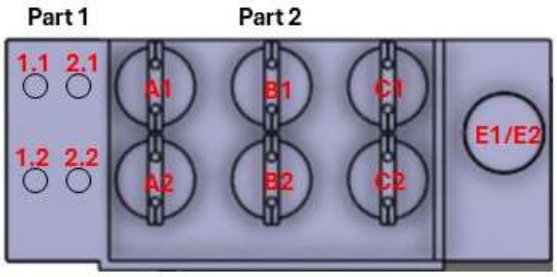


Figure 3: Tow spreading bars. Part 1 for roving spacing. Part 2 for roving spreading.

- Positioning (part1):
  Roving will be stacked as 2 layer
  4 roving on the top bar and 4 roving on the bottom bar.
  Roving pass from the top of bar 1.1 and 1.2, then on bottom of bar 2.1 and 2.2.
  The adjustments will be made as needed.
- Spacing (part1): Need for spacers to be verified based on staggering

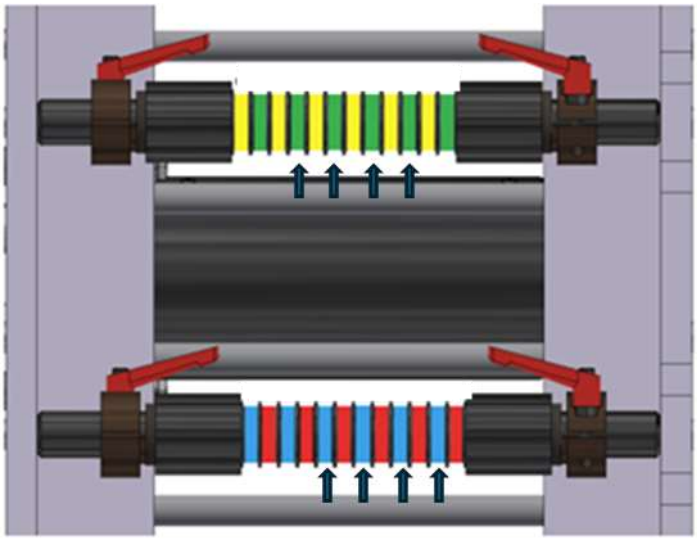


Figure 4: Placement and spacing of roving on bars 1.1 and 2.1

- Spreading Angles (part2):

SETUP 1: After initial trial, change the angles as follows:

Sections	Spreading angle
A1 & A2	0
B1 & B2	170
C1 & C2	350 & 80

E1 & E2	170

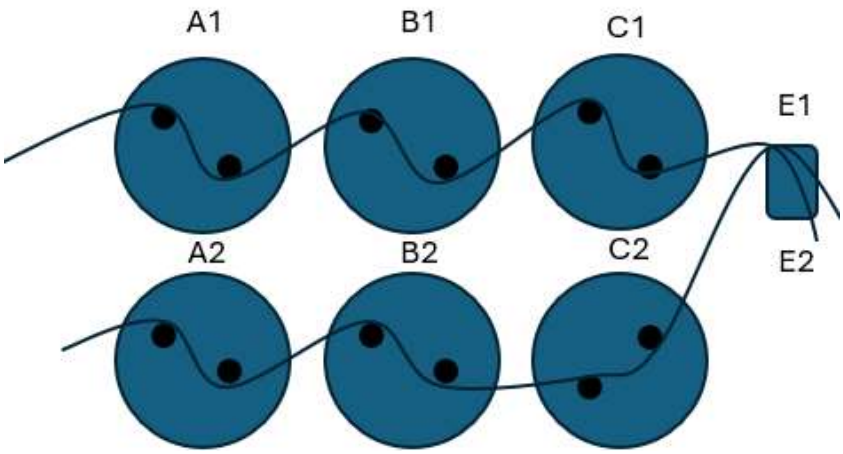


Figure 5: Roving direction on the spreading bars (part 2)

Setup 2: No dry spreading

4. Temperature Control Zones

Zone	Set Temperature (°C)
Spreading bars: E1 & E2	200 (to be verified)
F1	250
Extruder: T1	NA
Extruder: T2	NA
Extruder: T3	NA
Extruder: T4	NA
Melt Pipe: K	NA
Die: N	NA
Impregnation Roll: M	420
Post spreading: I	420
Calander	110

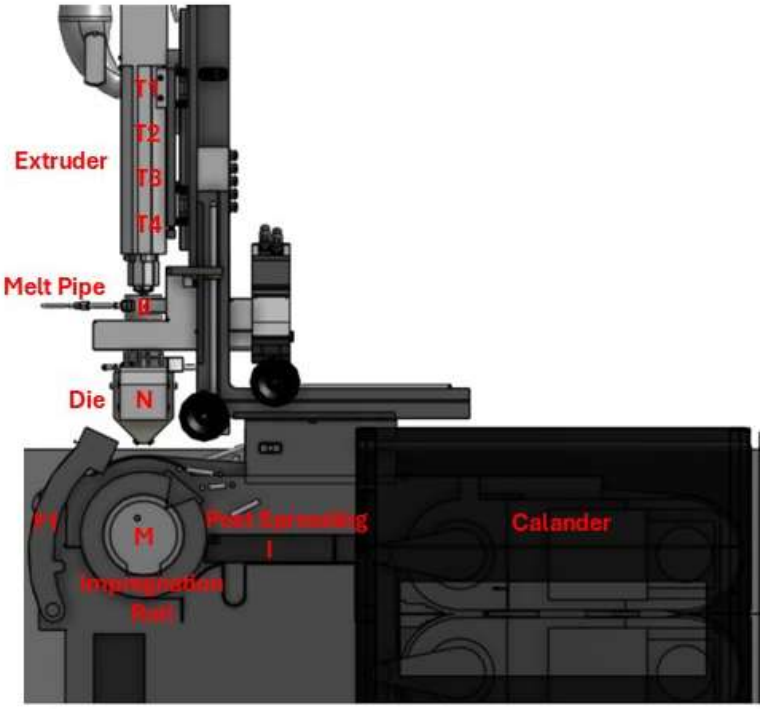


Figure 6: Temperature control Zones

5. **Other parameters**

- Calander pressure: 1500Nm (initial)
    - Note change if done:_____
- Pulling speed: 3.6 m/min (at the start)
- Nip-roller speed: No offset initially, to be checked
- Initial gap:

Stabilization Time Procedure

- **Stabilization Checks**:
    - Creel tension stability
    - Fiber pulling without twisting
- **Initial Stabilization**: 30 minutes before any changes
- **Parameter Change Stabilization**: 15 minutes
- **Observation Time After Stabilization**: 15 minutes
- **Notes on Stabilization *:***
    - Measured temperatures (every 10min):_____
    - Tape visualization:_____

Experimental Plan

Spreading and Tension would be measured during all experiments.

Variable Parameters

- Fiber tension (cN): 0, 50, 100, 150 cN
- Pulling speed m/min: 3, 3.6, 4.2, 5 m/min

Plan 1:

The slurry recipe will be verified during the trials. The gap will be finalized at beginning of each speed The following parameters will be studied

Trial	Dry spreading	Fiber tension (cN)	Line speed (m/min)	Impregnation roller temperature	Nip roller gap
1	Setup 1	150	3.6	420	
2	Setup 1	0	3.6	420	
3	Setup 1	100	3.6	420	
4	Setup 1	50	3.6	420	
5	Setup 1	250	3.6	420	
6	Setup 1	Best of above	5	420	
7	Setup 1	Best of above	3	420	
8	Setup 1	Best of above	4.2	420	
9	Setup 1	Best of above	3.6	420	
10	Setup 1	Best of above	Best of above	450	
11	Setup 2	150	3.6	420	
12	Setup 2	0	3.6	420	
13	Setup 2	100	3.6	420	
14	Setup 2	50	3.6	420	
15	Setup 2	250	3.6	420	

16	Setup 2	Best of above	5	420
17	Setup 2	Best of above	3	420
18	Setup 2	Best of above	4.2	420
19	Setup 2	Best of above	3.6	420
20	Setup 2	Best of above	Best of above	450

Notes: Any changes based on tapeline observations will be updated in this document.

Appendix C

Additional results

C.1 Methodology of viscosity mapping for different thickener and PEEK wt%

/

This section presents the experimental basis used to define the initial slurry formulations and the functional viscosity ranges for the impregnation processes.

The viscosity currently used and validated for kiss roller impregnation was initially selected based on findings from previous work by Eloi [38]. This selection was justified by the lack of a systematic investigation into slurry viscosity specifically for the nip roller process at that time. Although Eloi's research focused on tape manufacturing with the kiss roller, the distinct viscosity requirements of the kiss and nip roller processes required further examination to confirm the suitability of previously validated values.

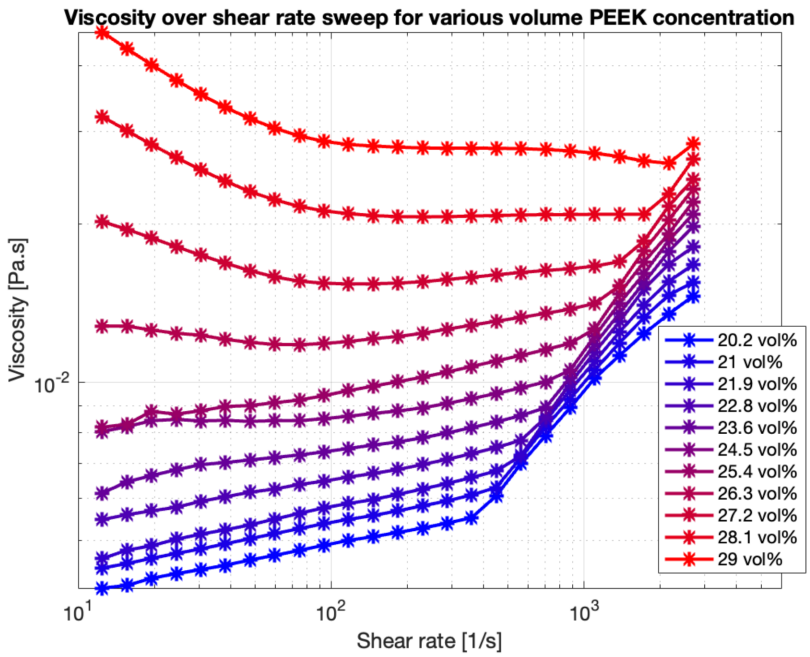


Figure C.1: Slurries viscosity over shear rate range (10 to 2700 [1/s]) with small PEEK concentration increments.[38]

An initial trial using a formulation with 10 wt% PEG resulted in a functional viscosity, as the slurry did not flow through the system at a given nip roller gap. However, the high PEG content was problematic. Evaporation of PEG, combined with processing temperatures above its ignition point, caused combustion of the tape. To improve safety and process robustness, it was necessary to investigate the functional viscosity range of the nip roller with reduced PEG content.

The reduction of PEG content was investigated using two complementary approaches:

- Variation of the PEEK content (wt%) in the slurry,
- Use of xanthan gum (XG) as a thickening agent, which is also more environmentally friendly than PEG.

The primary objective of the rheological experiments was to reproduce a viscosity equivalent to that achieved with 10 wt% PEG, using these alternative methods.

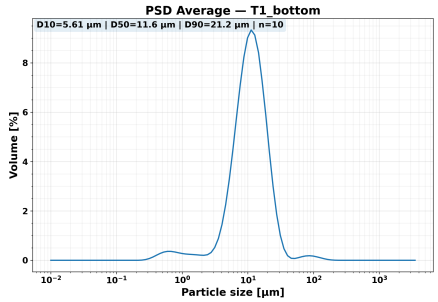
Subsequently, mapping the rheological behaviour of the slurry as a function of PEEK, PEG, and XG concentrations was necessary to understand the individual and combined effects of these constituents. Preliminary measurements were conducted on XG–water and PEG–water mixtures to characterise the influence of concentration on viscosity by identifying the domains of shear thinning, Newtonian plateau, and shear thickening. These tests provided initial insights into the effects of each additive at varying concentrations.

Previous manufacturing trials primarily used PEEK contents of 27 wt% and 30 wt%, so these values were selected as base formulations, with an additional composition at 33 wt%. These three concentrations (27, 30, and 33 wt%) provide a representative mapping across different solid loadings.

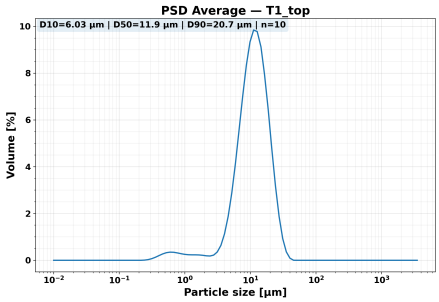
Yong Li et al. ([8]) reported that a concentration of 1 g/L XG significantly enhances viscosity. Therefore, a concentration range of XG from 0.25 g/L to 1.5 g/L, in increments of 0.25 g/L, was selected to cover a broad spectrum of viscosities.

These results, together with the definition of representative shear rate ranges for the process, enabled the development of a detailed mapping of the coupled effects of the slurry constituents. This data will be used to define a functional viscosity window for tape manufacturing with the nip roller.

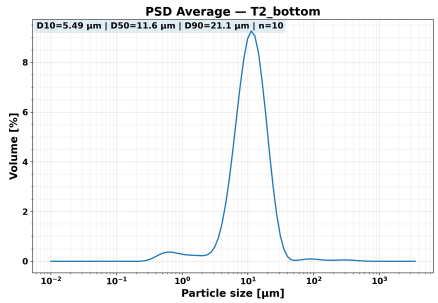
C.2 Extra PSD plot, Nip roller



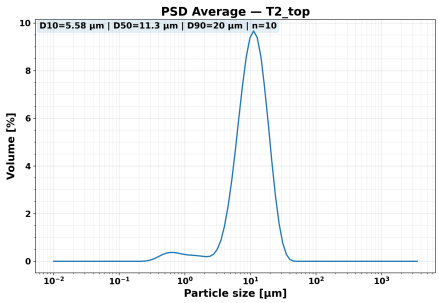
(a) T1_bottom



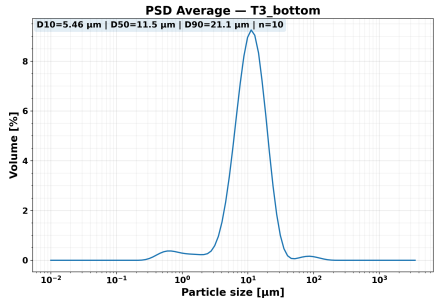
(b) T1_top



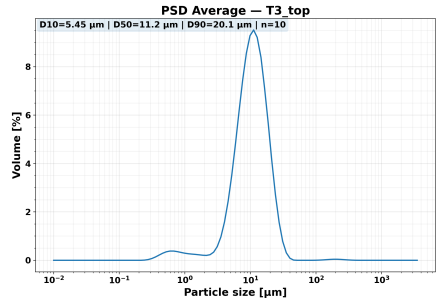
(c) T2_bottom



(d) T2_top



(e) T3_bottom



(f) T3_top

Figure C.2: PSD average curves (Nip route) — additional plots.

C.3 Quality metrics heatmap, Nip roller

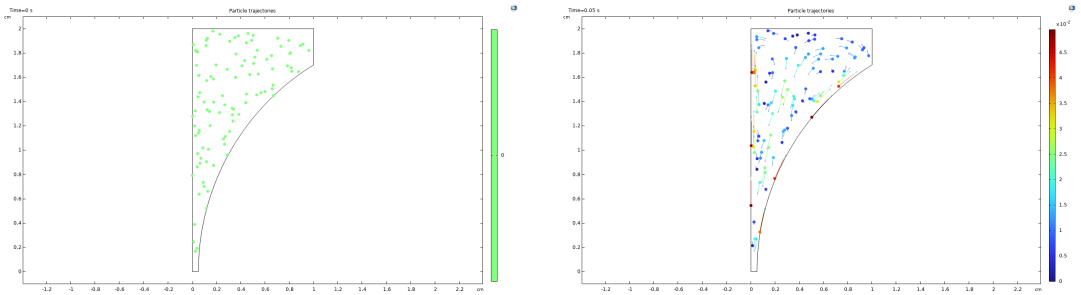
Table C.1: Quantitative heatmap metrics (creel tension).

Trial	Creel tension [cN]	FVF [%]	Fractions (comp / int / PEEK) [-]	Transi-tions [/1000 px]	Mean run (comp.) [px]	Max run (comp.) [px]	Max run (PEEK) [px]
T12_35	0	64.52	0.894 / 0.049 0.058	21.72	82.3	253	21
T09_35A	0	67.93	0.951 / 0.020 0.029	9.86	175.3	394	17
T09_35B	0	66.64	0.831 / 0.100 0.069	43.28	38.0	246	10
T05_30	250	66.42	0.922 / 0.026 0.052	11.46	160.9	269	23
T05_35	250	71.77	0.940 / 0.026 0.034	11.77	153.5	512	19
T03_30	200	71.35	0.932 / 0.024 0.044	10.00	178.0	515	22
T02_225	0	71.06	0.888 / 0.050 0.061	18.19	95.1	275	23
T02_27	0	67.28	0.914 / 0.044 0.042	18.88	94.5	265	13
T02_30	0	65.15	0.927 / 0.034 0.039	16.82	104.2	476	14
T01_225	150	70.02	0.965 / 0.018 0.017	10.05	182.4	511	11

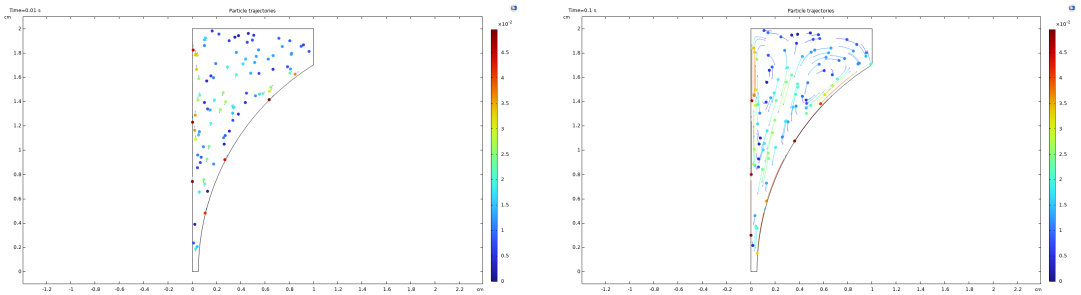
Table C.2: Quantitative heatmap metrics (line speed).

Trial	Line speed [m/min]	FVF [%]	Fractions (comp / int / PEEK) [-]	Transi-tions [/1000 px]	Mean run (comp.) [px]	Max run (comp.) [px]	Max run (PEEK) [px]
T12_35	3.6	64.52	0.894 / 0.049 0.058	21.72	82.3	253	21
T09_35A	3.6	67.93	0.951 / 0.020 0.029	9.86	175.3	394	17
T09_35B	3.6	66.64	0.831 / 0.100 0.069	43.28	38.0	246	10
T08_35	4.2	68.88	0.931 / 0.034 0.036	13.69	131.4	507	15
T08_35NS	4.2	64.58	0.928 / 0.027 0.044	17.13	105.5	274	18
T08_45	4.2	65.45	0.914 / 0.042 0.045	23.42	75.1	278	24
T07_35	3.0	67.29	0.952 / 0.022 0.026	12.78	143.2	470	11
T06_35	5.0	70.88	0.871 / 0.063 0.067	21.31	80.0	464	18
T06_45	5.0	63.80	0.882 / 0.068 0.051	35.88	47.9	309	17
T06_45V	5.0	64.83	0.857 / 0.062 0.081	21.45	79.9	251	21
T06_55	5.0	62.36	0.849 / 0.085 0.066	31.19	53.7	236	15
T02_225	3.6	71.06	0.888 / 0.050 0.061	18.19	95.1	275	23
T02_27	3.6	67.28	0.914 / 0.044 0.042	18.88	94.5	265	13
T02_30	3.6	65.15	0.927 / 0.034 0.039	16.82	104.2	476	14

C.4 Complementary Comsol transient images

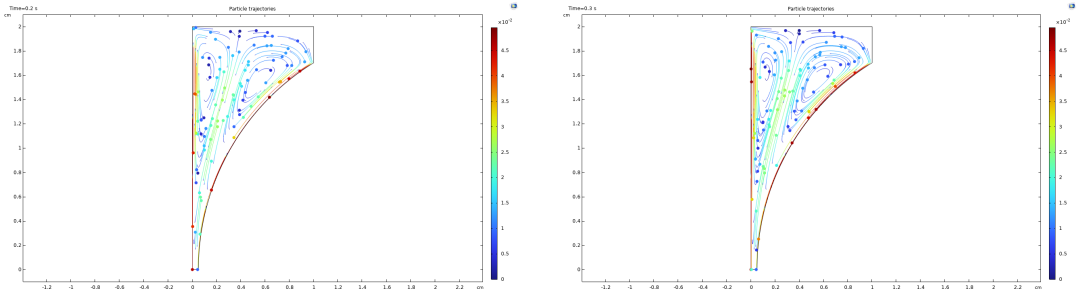


(a) $t = 0\,\mathrm{s}$ **(b)** $t = 0.01\,\mathrm{s}$

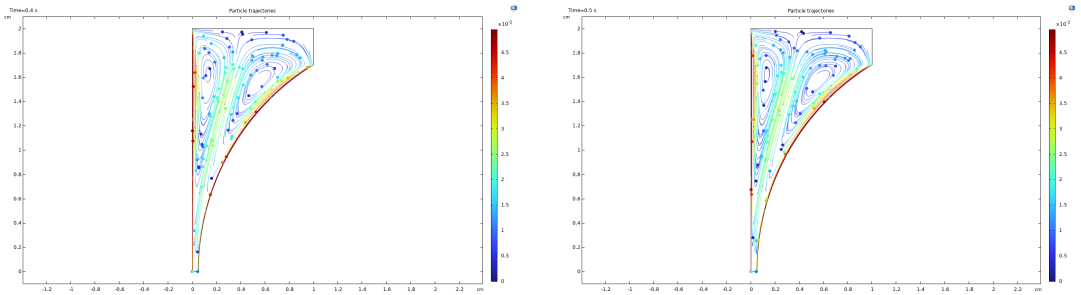


(c) $t = 0.05\,\mathrm{s}$ **(d)** $t = 0.1\,\mathrm{s}$

Figure C.3: COMSOL snapshots (early timesteps).

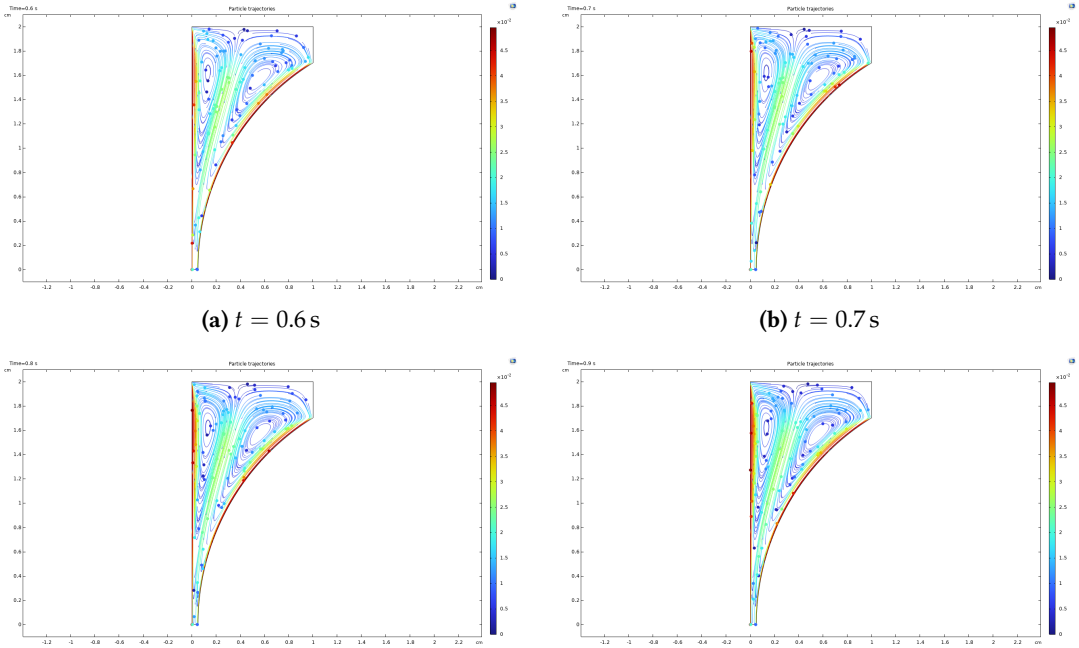


(a) $t = 0.2\,\mathrm{s}$ **(b)** $t = 0.3\,\mathrm{s}$



(c) $t = 0.4\,\mathrm{s}$ **(d)** $t = 0.5\,\mathrm{s}$

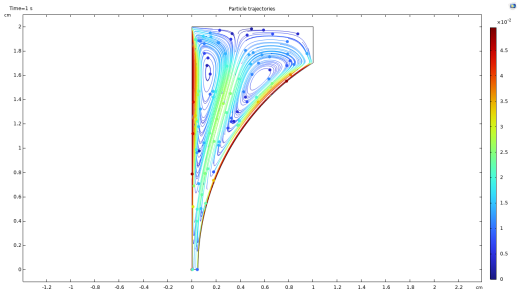
Figure C.4: COMSOL snapshots (mid timesteps).



(a) $t = 0.6\,\mathrm{s}$ **(b)** $t = 0.7\,\mathrm{s}$

(c) $t = 0.8\,\mathrm{s}$ **(d)** $t = 0.9\,\mathrm{s}$

Figure C.5: COMSOL snapshots (late timesteps).



(a) $t = 1.0\,\mathrm{s}$

Figure C.6: COMSOL snapshot at $t = 1.0\,\mathrm{s}$.

Appendix D

Models and Derivations

D.1 Viscosity Model for Nip-Roller Impregnation

Nip Roller (Reverse, Premetered): Couette–Poiseuille Model and Estimation of the Active Length L

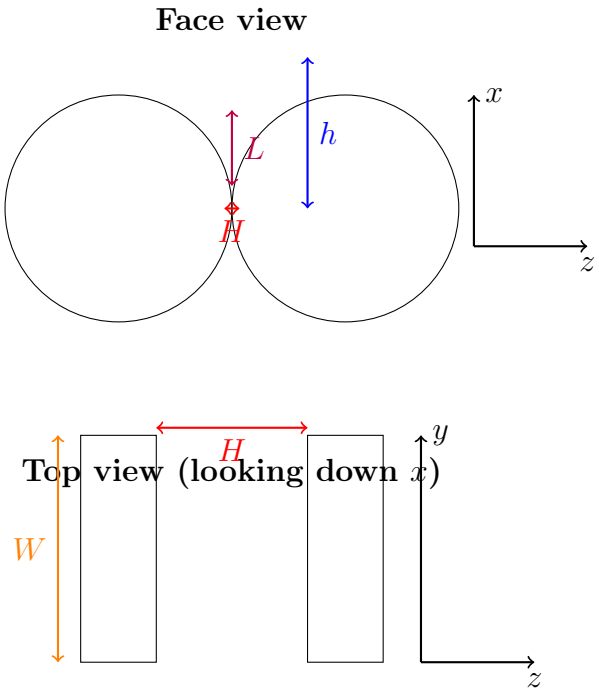


Figure 1: Definition of the main geometrical parameters and axes: bead height h, nip length L, gap size H, and roller width W.

1 Introduction (basic idea)

We start from the **Navier–Stokes equations** for incompressible fluids. In the **lubrication regime** (thin film, negligible inertia), they reduce to the **Stokes equations** and yield analytically the classical **Couette** (moving walls) and **Poiseuille** (pressure-driven) profiles [4, 5].

Axis orientation. Axis x: along the roll (main flow direction). Axis z: across the film thickness (perpendicular to rolls). Pressure is assumed to be *quasi-uniform* in z ($p = p(x)$) in this framework.

2 Glossary of terms

- H: gap thickness (m).

- L: length of the quasi-parallel region (m).
- W: effective width (m).
- V_1, V_2: roll surface velocities ($\mathrm{m\,s^{-1}}$).
- $U_{\mathrm{out}} = |V_1 - V_2|/2$: characteristic convective velocity ($\mathrm{m\,s^{-1}}$).
- h: average bead height (m).
- ρ: slurry density ($\mathrm{kg\,m^{-3}}$).
- η: dynamic viscosity (Pa s).
- $\dot{\gamma}$: shear rate ($\mathrm{s^{-1}}$); $\dot{\gamma}_\star \approx |V_1 - V_2|/H$.
- Q: volumetric flow rate ($\mathrm{m^3/s}$).
- $q = Q/W$: flow rate per unit width ($\mathrm{m^2/s}$).
- $\frac{dp}{dx}$: longitudinal pressure gradient (Pa/m).
- $Re = \rho U_{\mathrm{out}} H/\eta$: Reynolds number (—).
- $Bo = \rho g h^2/\sigma$: Bond number (—).

3 Couette–Poiseuille model (planar channel)

3.1 Validity assumptions

Thin film $H/L \ll 1$, laminar, negligible inertia ($Re \ll 1$), pressure uniform in z.

3.2 Stokes equation and velocity profile

$$\mu \frac{\partial^2 u}{\partial z^2} = \frac{\partial p}{\partial x}, \qquad \frac{\partial p}{\partial z} = 0.$$

With $u(0) = V_2$, $u(H) = V_1$, the velocity profile is:

$$u(z) = \underbrace{\frac{V_1 - V_2}{H}\, z + V_2}_{\text{Couette}} \underbrace{- \frac{1}{2\eta}\frac{dp}{dx}\, z(H - z)}_{\text{Poiseuille}}.$$

3.3 Flow rate per unit width

$$\boxed{q = -\frac{H^3}{12\,\eta}\frac{dp}{dx} + \frac{H}{2}(V_1 + V_2)}$$

Reverse quasi-symmetric case. If $V_1 \approx -V_2$, then $V_1 + V_2 \approx 0$ (Couette term vanishes):

$$q \approx -\frac{H^3}{12\,\eta}\frac{dp}{dx}.$$

4 Hydrostatic gradient (bead) and Bond criterion

The bead of average height h provides a hydrostatic head $\Delta p \simeq \rho g h$, distributed along the active length L:

$$\boxed{\left|\frac{dp}{dx}\right| \approx \frac{\rho g h}{L}}$$

4.1 Clarification between bead height h and nip length L

A frequent source of confusion is the distinction between the bead height h and the nip length L, since both are oriented along the same axis x (direction of the flow). These two quantities, however, play very different roles:

- The **bead height** h represents the hydrostatic column of slurry feeding the nip. It determines the available pressure difference at the entrance, which can be approximated as
$$\Delta p \approx \rho g h.$$
- The **nip length** L corresponds to the effective distance that the slurry must travel through the narrow gap between the rollers. It is fixed by the roller geometry (radius and gap size) and typically lies in the millimeter to centimeter range. It is not a free parameter like h.

In lubrication theory, the pressure field inside the nip is assumed to vary mainly along x, while being nearly uniform across the gap H and across the width W. The hydrostatic overpressure at the entrance $\Delta p \simeq \rho g h$ is thus *distributed* over L:

$$\left|\frac{dp}{dx}\right| \approx \frac{\Delta p}{L} \approx \frac{\rho g h}{L}.$$

This explains why h and L cannot be interchanged: h sets the driving pressure, while L sets the distance over which this pressure drop is applied.

5 Definition of L (geometric approach)

5.1 Reduced radius

For two cylinders of radii R_1, R_2:

$$\frac{1}{R'} = \frac{1}{R_1} + \frac{1}{R_2}.$$

Locally, $h(x) = H_0 + \frac{x^2}{2R'}$, but for small windows $h(x) \simeq H_0$.

5.2 Criteria

(a) Small slope.

$$\left|\frac{\partial h}{\partial x}\right| = \frac{|x|}{R'} \leq \beta \;\Rightarrow\; L_\beta = \beta R'.$$

(b) Small relative variation.

$$\frac{h(L)-H_0}{H_0} \approx \frac{L^2}{2R'H_0} \le \alpha \;\Rightarrow\; L_\alpha = \sqrt{2\alpha R' H_0}.$$

(c) Adopted definition.

$$L = \min(L_\alpha, L_\beta).$$

5.3 Recommended ranges

$$\alpha \in [0.10, 0.20], \quad \beta \in [0.05, 0.20].$$

5.4 Example

For $D = 300$ mm, $R' = 75$ mm, $H_0 = 1$ mm: $L_\alpha(0.1) \simeq 3.9$ mm, $L_\beta(0.1) \simeq 7.5$ mm $\Rightarrow L \simeq 4$ mm.

Quantitative justification of the tolerances α and β

Set-up. In the nip core, the true gap is parabolic,

$$h(x) = H_0 + \frac{x^2}{2R'}, \qquad |x| \le L,$$

while the local Couette–Poiseuille closure uses the constant-gap approximation $h(x) \approx H_0$ over a short window. Two engineering tolerances are introduced to keep this approximation consistent:

$$\alpha \;\triangleq\; \frac{h(L)-H_0}{H_0} = \frac{L^2}{2R'H_0}, \qquad \beta \;\triangleq\; \max_{|x|\le L}\left|\frac{\partial h}{\partial x}\right| = \frac{L}{R'}.$$

(i) Error bound linked to α

The pressure-driven (Poiseuille) term scales with the local permeability h^3. Replacing $h(x)$ by H_0 thus incurs a relative error that is governed by the average of h^3 over the window $[0, L]$:

$$\overline{h^3} = \frac{1}{L}\int_0^L \left(H_0 + \frac{x^2}{2R'}\right)^3 dx.$$

Expanding the cube and integrating term by term gives

$$\overline{h^3} = H_0^3 \left[1 + \underbrace{\frac{L^2}{2R'H_0}}_{=\,\alpha} + \underbrace{\tfrac{3}{5}\left(\tfrac{L^2}{2R'H_0}\right)^2}_{=\,\frac{3}{5}\alpha^2} + \underbrace{\tfrac{1}{7}\left(\tfrac{L^2}{2R'H_0}\right)^3}_{=\,\frac{1}{7}\alpha^3}\right].$$

The relative deviation from H_0^3 is therefore

$$\varepsilon_\alpha = \frac{\overline{h^3} - H_0^3}{H_0^3} = \alpha + \tfrac{3}{5}\alpha^2 + \tfrac{1}{7}\alpha^3.$$

To first order,

$$\varepsilon_\alpha \;=\; \alpha + O(\alpha^2).$$

Since $q_{\mathrm{Pois}} \propto h^3$ for a given pressure gradient, replacing $h^3(x)$ by H_0^3 overestimates the hydraulic resistance and thus underestimates η by a factor $\simeq 1/(1+\alpha) \approx 1-\alpha$. Choosing $\alpha \leq 0.1$ (resp. 0.2) caps the model bias at $\lesssim 10\%$ (resp. $\lesssim 20\%$). This provides a quantitative justification for selecting $\alpha \in [0.1,\, 0.2]$.

(ii) Small-slope consistency linked to β. The small-slope hypothesis required by lubrication theory is $|h'(x)| \ll 1$ (in radians). With the parabolic geometry, $|h'(x)| = |x|/R' \leq L/R' = \beta$. Taking $\beta \leq 0.1$–0.2 corresponds to a maximal local angle of $\approx 6°$–$11°$, consistent with a quasi-parallel film and the neglect of streamwise viscous diffusion. Note the leading-order slope error enters kinematics at $O(\beta^2)$, so keeping $\beta \lesssim 0.1$ keeps these corrections at the percent level.

(iii) Practical summary.

$$L_\alpha = \sqrt{2\alpha R' H_0}, \qquad L_\beta = \beta R', \qquad L = \min(L_\alpha, L_\beta).$$

Pick α from the *acceptable viscosity bias* (e.g. $10\% \Rightarrow \alpha = 0.1$) and β from the *acceptable non-parallelism* (e.g. $\beta = 0.1$). This makes the choice of L an explicit error-budget decision rather than an arbitrary rule of thumb.

6 Experimental viscosity formula

Weighing gives $Q = \Delta m/(\rho \Delta t)$, then $q = Q/W$. Insert hydrostatic gradient:

$$\boxed{\eta_{\mathrm{exp}} = \frac{H^3}{12 q_{\mathrm{eff}}} \frac{\rho g h}{L}, \quad q_{\mathrm{eff}} = q - \tfrac{H}{2}(V_1 + V_2)}$$

In symmetric case ($V_1 + V_2 \simeq 0$):

$$\eta_{\mathrm{exp}} \approx \frac{H^3}{12 q} \frac{\rho g h}{L}.$$

7 Consistency checks

- Shear rate: $\dot{\gamma}_\star \approx |V_1 - V_2|/H$.
- Convective velocity: $U_{\mathrm{out}} = |V_1 - V_2|/2$.
- Reynolds number: $Re = \rho U_{\mathrm{out}} H/\eta_{\mathrm{exp}}$.
- Bond number: $Bo = \rho g h^2/\sigma$.
- Exit film thickness: $t_2 \approx q/U_{\mathrm{out}}$.

8 Experimental procedure

1. Identify Newtonian plateau with rheometer.
2. Adjust V_1, V_2, H so $\dot{\gamma}_\star$ lies in window.
3. Fix bead height $h > h_{\text{crit}}$ (no vortices).
4. Measure $H, L, W, V_1, V_2, h, \Delta m, \Delta t, \rho$.
5. Compute η_{exp}.
6. Check $Re \ll 1$ and Bo.
7. Compare with η_{rheo}; if deviations, use non-Newtonian model.

References

References

[1] NASA Reference Publication, *Fundamentals of Fluid Film Lubrication*. https://ntrs.nasa.gov/api/citations/19910021217/downloads/19910021217.pdf

[2] K. L. Johnson, *Contact Mechanics*, Cambridge University Press, 1985. doi:10.1017/CBO9781139171731

[3] Q. Liu, *Theoretical and Experimental Studies of Elastohydrodynamic Lubrication Problems*, PhD Thesis, University of Twente, 2002. https://ris.utwente.nl/ws/portalfiles/portal/6079997/thesis_Qiang_Liu.pdf

[4] MIT OpenCourseWare, *Advanced Fluid Mechanics*, Couette–Poiseuille section. https://ocw.mit.edu/courses/2-25-advanced-fluid-mechanics-fall-2013/

[5] Wikipedia, *Lubrication Theory*. https://en.wikipedia.org/wiki/Lubrication_theory

D.2 Uncertainty estimation for PEEK content and fibre volume fraction

The PEEK mass fraction and fibre volume fraction (FVF) of the manufactured CF/PEEK tapes were determined using a mass balance approach. The composite mass was measured on a nominal 1000 mm tape segment, while the fibre mass contained in this segment was obtained by weighing carbon fibre tows over 1000 mm and scaling to the eight tows used in the tape.

Measured quantities and derived relations

The measured quantities are:

- m_c: mass of the composite tape segment
- m_f: mass of fibre contained in the segment (eight tows, 1000 mm each)
- ρ_f: fibre density ($\rho_f = 1.80\ \mathrm{g\,cm^{-3}}$, supplier value)
- ρ_m: PEEK density ($\rho_m = 1.32\ \mathrm{g\,cm^{-3}}$, supplier value)

The matrix (PEEK) mass is obtained by difference:

$$m_m = m_c - m_f. \tag{D.1}$$

The PEEK mass fraction is calculated as:

$$w_m = \frac{m_m}{m_c} = 1 - \frac{m_f}{m_c}. \tag{D.2}$$

The fibre volume fraction is computed from the measured masses and material densities:

$$V_f = \frac{m_f/\rho_f}{(m_f/\rho_f) + (m_m/\rho_m)}. \tag{D.3}$$

Uncertainty propagation

Uncertainties were propagated using first-order error propagation, assuming independent input quantities. The general form is:

$$\sigma_y = \sqrt{\sum_i \left(\frac{\partial y}{\partial x_i}\sigma_{x_i}\right)^2}. \tag{D.4}$$

For the fibre volume fraction, the propagated uncertainty is expressed as:

$$\sigma_{V_f} = \sqrt{\left(\frac{\partial V_f}{\partial m_c}\sigma_{m_c}\right)^2 + \left(\frac{\partial V_f}{\partial m_f}\sigma_{m_f}\right)^2}. \tag{D.5}$$

The analytical expressions of the partial derivatives are standard and are not developed here for clarity.

Assumptions and justification of input uncertainties

Composite mass m_c. The tape segment was cut to a nominal length of 1000 mm. A practical cutting tolerance of ± 2 mm was assumed. As the tape cross-section is approximately constant over this length, the composite mass is assumed to scale linearly with length. The relative uncertainty on the composite mass is therefore:

$$\frac{\sigma_{m_c}}{m_c} \approx \frac{2}{1000} = 0.002, \tag{D.6}$$

leading to:

$$\sigma_{m_c} \approx 0.002\, m_c. \tag{D.7}$$

Fibre mass m_f. The fibre mass corresponding to eight tows over 1000 mm was obtained by weighing two bundles of four tows:

$$m_f = m_{4,1} + m_{4,2}. \tag{D.8}$$

Only two measurements were available. To avoid underestimating the uncertainty, a conservative approach was adopted and the uncertainty on the fibre mass was taken as the full measurement spread:

$$\sigma_{m_f} \approx |m_{4,2} - m_{4,1}|. \tag{D.9}$$

This choice accounts for tow-to-tow variability, handling effects, and the limited statistical sample.

Material densities. Supplier values for the fibre and matrix densities were used and treated as constants. Their uncertainties are expected to be small compared with the dominant mass-related uncertainties and were therefore neglected.

Numerical examples

The uncertainty estimation procedure described above is illustrated using three representative tape samples covering a wide range of fibre volume fractions. Tape 1 is used as a reference case, while T46 and T25 are included to assess the robustness of the uncertainty magnitude for lower and intermediate FVF values.

Tape 1 (reference case). For Tape 1, the following values were used:

$$m_c = 16.7579 \text{ g}, \tag{D.10}$$

$$m_{4,1} = 6.4605 \text{ g}, \qquad m_{4,2} = 6.4960 \text{ g}, \tag{D.11}$$

$$m_f = 12.9565 \text{ g}. \tag{D.12}$$

The resulting fibre volume fraction is:

$$V_f = 0.714. \tag{D.13}$$

Based on the uncertainty propagation described above, the associated uncertainty is:

$$\sigma_{V_f} = 0.003. \tag{D.14}$$

Thus:

$$V_f = 0.714 \pm 0.003. \tag{D.15}$$

Tape T46 (low FVF). For Tape T46, the measured composite mass was:

$$m_c = 22.3226 \text{ g}, \tag{D.16}$$

leading to:

$$V_f = 0.5049 \ (50.49 \ \%). \tag{D.17}$$

Using the same uncertainty assumptions as for Tape 1, the propagated uncertainty is:

$$\sigma_{V_f} \approx 0.002. \tag{D.18}$$

Thus:

$$V_f = 0.505 \pm 0.002. \tag{D.19}$$

Tape T25 (intermediate FVF). For Tape T25, the measured composite mass was:

$$m_c = 19.0385 \text{ g}, \tag{D.20}$$

corresponding to:

$$V_f = 0.6097 \ (60.97 \ \%). \tag{D.21}$$

The resulting propagated uncertainty is:

$$\sigma_{V_f} \approx 0.0025. \tag{D.22}$$

Thus:

$$V_f = 0.610 \pm 0.003. \tag{D.23}$$

Summary These three numerical examples show that, despite significant variations in fibre volume fraction (approximately 50–71 %), the absolute uncertainty on V_f remains of the same order of magnitude. For all investigated tapes, the uncertainty lies between ± 0.002 and ± 0.003, depending mainly on the composite mass. This uncertainty is small compared to the process-induced variability observed in the experimental results and supports the use of a representative uncertainty value in the main analysis.

D.3 Uncertainty estimation for slurry PEEK mass fraction

The PEEK mass fraction in the slurry was determined using a gravimetric drying and calcination procedure based on successive mass measurements of the same glass vial. The uncertainty associated with this measurement was estimated using first-order error propagation.

Definition of the measured quantities

For each slurry sample, the following masses were measured:

- m_0: mass of the empty glass vial,
- m_1: mass of the glass vial filled with wet slurry,
- m_3: mass of the glass vial after oven drying and furnace treatment, corresponding to the remaining PEEK mass.

From these measurements, the slurry mass and the PEEK mass are defined as:

$$m_{\text{slurry}} = m_1 - m_0, \tag{D.24}$$

$$m_{\text{PEEK}} = m_3 - m_0. \tag{D.25}$$

The slurry PEEK mass fraction is then expressed as:

$$w_{\text{PEEK}} = \frac{m_{\text{PEEK}}}{m_{\text{slurry}}} = \frac{m_3 - m_0}{m_1 - m_0}. \tag{D.26}$$

Uncertainty propagation

The uncertainty on the slurry PEEK mass fraction was estimated by first-order propagation of the weighing uncertainties, assuming independent mass measurements:

$$\sigma_w = \sqrt{\left(\frac{\partial w}{\partial m_0}\sigma_{m_0}\right)^2 + \left(\frac{\partial w}{\partial m_1}\sigma_{m_1}\right)^2 + \left(\frac{\partial w}{\partial m_3}\sigma_{m_3}\right)^2}. \tag{D.27}$$

With $w = \frac{m_3 - m_0}{m_1 - m_0}$, the partial derivatives are:

$$\frac{\partial w}{\partial m_3} = \frac{1}{m_1 - m_0}, \tag{D.28}$$

$$\frac{\partial w}{\partial m_1} = -\frac{m_3 - m_0}{(m_1 - m_0)^2}, \tag{D.29}$$

$$\frac{\partial w}{\partial m_0} = \frac{m_3 - m_1}{(m_1 - m_0)^2}. \tag{D.30}$$

The uncertainty on the PEEK mass fraction expressed in weight percent is given by:

$$\sigma_{\%\text{PEEK}} = 100\,\sigma_w. \tag{D.31}$$

– Assumptions on weighing uncertainty

All mass measurements were performed using the same analytical balance. A uniform weighing uncertainty of:

$$\sigma_{m_0} = \sigma_{m_1} = \sigma_{m_3} = 0.1 \text{ mg} \tag{D.32}$$

was assumed. This value corresponds to the balance resolution and represents the dominant instrumental uncertainty. Additional procedural effects such as minor evaporation during handling are minimized by immediate weighing and are not explicitly included.

– Numerical examples

To illustrate the magnitude of the propagated uncertainty, three representative slurry samples were evaluated.

Sample 250930_N01. For this sample, the measured PEEK mass fraction was:

$$w_{\mathrm{PEEK}} = 27.41 \text{ wt\%}. \tag{D.33}$$

The propagated uncertainty is:

$$\sigma_{\%\mathrm{PEEK}} \approx 0.003 \text{ wt\%}. \tag{D.34}$$

Sample 250930_N05. This sample corresponds to a higher slurry PEEK content:

$$w_{\mathrm{PEEK}} = 32.20 \text{ wt\%}. \tag{D.35}$$

The associated uncertainty is:

$$\sigma_{\%\mathrm{PEEK}} \approx 0.0035 \text{ wt\%}. \tag{D.36}$$

Sample 251001_N06. At the end of the manufacturing period, the measured PEEK content was:

$$w_{\mathrm{PEEK}} = 32.97 \text{ wt\%}. \tag{D.37}$$

The propagated uncertainty remains of the same order:

$$\sigma_{\%\mathrm{PEEK}} \approx 0.0035 \text{ wt\%}. \tag{D.38}$$

– Discussion

These numerical examples demonstrate that the uncertainty associated with the gravimetric determination of slurry PEEK mass fraction is very small compared to the observed temporal variations of several weight percent. For all investigated samples, the uncertainty remains on the order of ± 0.003–0.004 wt% and therefore does not affect the interpretation of the slurry composition evolution during manufacturing.

– Adopted total uncertainty (method-dominated)

While the balance-resolution-based propagated uncertainty is negligible (on the order of 0.003–0.004 wt%), the overall uncertainty of the gravimetric method is expected to be dominated by procedural effects. In the absence of repeated measurements, a conservative equivalent mass deviation on the final residue of $\delta m_{\mathrm{PEEK}} = 5$ mg is assumed. For a typical slurry mass of $m_{\mathrm{slurry}} \approx 4$ g, this corresponds to:

$$\delta(\%\mathrm{PEEK})_{\mathrm{method}} \approx 100\,\frac{\delta m_{\mathrm{PEEK}}}{m_{\mathrm{slurry}}} = 100\,\frac{0.005}{4} = 0.125 \text{ wt\%}. \tag{D.39}$$

Adding the negligible balance-related contribution (approximately 0.003–0.004 wt%) yields an overall uncertainty of about 0.125–0.125 wt%, which is conservatively rounded to:

$$\Delta(\%\text{PEEK}) = \pm 0.125 \text{ wt\%}. \tag{D.40}$$

This constant uncertainty is adopted for all reported slurry PEEK mass fraction values.

Appendix E

New student, Read me

E.1 Project repository and continuation package

To facilitate reproducibility and support future students, the project deliverables are packaged in a GitHub repository (data, scripts, figures, and supporting material). The folder structure follows the practical workflow of the thesis and is designed to be directly navigable.

Access. Repository: `https://github.com/Dockait/TUDelft-Thesis`.

Folder overview and contents.

- **Analysis** — All analysis code used throughout the thesis, including workflows for FVF, microscopy image processing, PSD post-processing, PEEK content calculations, and slurry preparation files. Most scripts were developed in Visual Studio Code and are typically executed via a dedicated `main` entry point. The codebase is intentionally strict and relies on predefined file naming and folder conventions; users are therefore encouraged to read the local documentation and script headers before applying the pipeline to new datasets or renamed files.
- **CAD** — CAD models of the TapeLine, as well as additional CAD parts developed to simplify tape handling during experiments. In particular, the `unwinder` subfolder contains designs created to support tape unrolling and handling.
- **Lab_training** — General laboratory information and practical guidance relevant for working safely and consistently in the lab environment.
- **Preliminary_reading_info** — A curated set of key papers (typically 5–6) selected to help newcomers quickly understand the project context and the underlying physics of slurry-based impregnation.
- **Presentation** — Open presentation material from the lab (e.g., general introductions or non-confidential slide decks) that provides additional context around the platform and ongoing work.
- **Report** — Thesis report material, including the manuscript and an `images` folder containing figures and supporting visual assets used during writing.

Zürcher Hochschule
für Angewandte Wissenschaften

Life Sciences und
Facility Management

DECLARATION OF ORIGINALITY

Master's Thesis for the School of Life Sciences and Facility Management

By submitting this Master's thesis, the student attests of the fact that all the work included in the assignment is their own and was written without the help of a third party.

The student declares that all sources in the text (including Internet pages) and appendices have been correctly disclosed. This means that there has been no plagiarism, i.e. no sections have been partially or wholly taken from other texts and represented as the student's own work or included without being correctly referenced.

Any misconduct will be dealt with according to paragraphs 39 and 40 of the General Academic Regulations for Bachelor's and Master's Degree Courses at the Zurich University of Applied Sciences (dated 29 Januar 2008) and subject to the provisions for disciplinary action stipulated in the University regulations (Rahmenprüfungsordnung ZHAW (RPO)).

Town/City, Date: Signature:

Fribourg, 06.02.2026 .....

The original signed and dated document (no copies) must be included in the appendix of the ZHAW version of all Master's theses submitted.

Bibliography

[1] Claire Steggall-Murphy et al. "A model for thermoplastic melt impregnation of fiber bundles during consolidation of powder-impregnated continuous fiber composites". In: *Composites Part A: Applied Science and Manufacturing* 41.1 (Jan. 2010), pp. 93–100. ISSN: 1359835X. DOI: 10.1016/j.compositesa.2009.09.026.

[2] Bernard J Hamrock. *NASA Reference Publication Fundamentals of Fluid Film Lubrication.* Tech. rep. 1991. URL: https://ntrs.nasa.gov/api/citations/19910021217/downloads/19910021217.pdf.

[3] K. K.C. Ho et al. "Wet impregnation as route to unidirectional carbon fibre reinforced thermoplastic composites manufacturing". In: *Plastics, Rubber and Composites.* Vol. 40. 2. Mar. 2011, pp. 100–107. DOI: 10.1179/174328911X12988622801098.

[4] Composites Engineering MAterials and STructures (MAST) research group. *Composites Design and Manufacture (Plymouth University teaching support materials).* Feb. 2006.

[5] A. Texier et al. "Fabrication of PEEK/carbon fibre composites by aqueous suspension prepregging". In: *Polymer* 34.4 (Feb. 1993), pp. 896–906. ISSN: 0032-3861. DOI: 10.1016/0032-3861(93)90378-N. URL: https://www.sciencedirect.com/science/article/pii/003238619390378N.

[6] Thomas Köhler et al. "An Overview of Impregnation Methods for Carbon Fibre Reinforced Thermoplastics". In: *Key Engineering Materials* 742 (Sept. 2017), pp. 473–481. DOI: 10.4028/www.scientific.net/KEM.742.473.

[7] A M Vodermayer, J C Kaerger, and G Hinrichsen. *Manufacture of high performance fibre-reinforced thermoplastics by aqueous powder impregnation.* Tech. rep. 1993.

[8] Yanrui Li et al. "Study on polyetheretherketone prepreg manufactured by aqueous system of powder impregnation". In: *Polymer Composites* 43.5 (2022), pp. 2980–2991. DOI: https://doi.org/10.1002/pc.26592. URL: https://4spepublications.onlinelibrary.wiley.com/doi/abs/10.1002/pc.26592.

[9] R Talreja. "Studies on the failure analysis of composite materials with manufacturing defects". In: *Mechanics of Composite Materials* 49.1 (2013), pp. 35–44. ISSN: 1573-8922. DOI: 10.1007/s11029-013-9318-6. URL: https://doi.org/10.1007/s11029-013-9318-6.

[10] S. Gomarasca et al. "Characterising microstructural organisation in unidirectional composites". In: *Composites Science and Technology* 215 (Oct. 2021), p. 109030. ISSN: 0266-3538. DOI: 10.1016/J.COMPSCITECH.2021.109030. URL: https://www.sciencedirect.com/science/article/pii/S0266353821003869.

[11] TU Delft Faculty of Aerospace Engineering. *Delft TapeLab.* URL: https://www.tudelft.nl/lr/delft-tapelab.

[12] TU Delft. *TU Delft NextGen Innovation Days – TapeLab.* URL: https://www.aanmelder.nl/tudnxtgeninnovationdays/tapelab?version=latest.

[13] Xin Liu et al. "Isothermal crystallisation ATP process for thermoplastic composites with semi-crystalline matrices using automated tape placement machine". In: *Composites Part B: Engineering* 227 (Dec. 2021), p. 109381. ISSN: 1359-8368. DOI: 10.1016/

J.COMPOSITESB.2021.109381. URL: https://www.sciencedirect.com/science/article/abs/pii/S1359836821007526?via%3Dihub.

[14] Hao Liu et al. "Study on the process of hot gas-assisted GF/PA5X thermoplastic composites automated tape placement". In: *Polymer Composites* 45.17 (2024), pp. 16021–16032. DOI: 10.1002/pc.28886. URL: https://4spepublications.onlinelibrary.wiley.com/doi/abs/10.1002/pc.28886.

[15] Daniel Kaczmarek et al. "An investigation of in situ impregnation for additive manufacturing of thermoplastic composites". In: *Journal of Manufacturing Processes* 64 (Apr. 2021), pp. 972–981. ISSN: 1526-6125. DOI: 10.1016/J.JMAPRO.2021.02.018. URL: https://www.sciencedirect.com/science/article/abs/pii/S1526612521001031?via%3Dihub.

[16] Simon Zeidler et al. "Novel Processes for the Production of Continuous Carbon Fiber-Reinforced Thermoplastic Polymers via Additive Manufacturing and Comparisons". In: *Polymers* 17.5 (2025). ISSN: 2073-4360. DOI: 10.3390/polym17050584. URL: https://www.mdpi.com/2073-4360/17/5/584.

[17] Kirill Minchenkov et al. "Pultrusion of thermoplastic composites with mechanical properties comparable to industrial thermoset profiles". In: *Composites Communications* 44 (Dec. 2023), p. 101766. ISSN: 2452-2139. DOI: 10.1016/J.COCO.2023.101766. URL: https://www.sciencedirect.com/science/article/abs/pii/S2452213923002747.

[18] Alexander Vedernikov et al. "Effects of the Pre-Consolidated Materials Manufacturing Method on the Mechanical Properties of Pultruded Thermoplastic Composites". In: *Polymers* 14.11 (2022). ISSN: 2073-4360. DOI: 10.3390/polym14112246. URL: https://www.mdpi.com/2073-4360/14/11/2246.

[19] Abd-Elrahman Korayem et al. "Characterization of interlaminar properties across processing parameters of consolidation of CF/PEKK composites for benchmarking performance". In: *Polymer Composites* 46.7 (2025), pp. 6714–6724. DOI: https://doi.org/10.1002/pc.29390. URL: https://4spepublications.onlinelibrary.wiley.com/doi/abs/10.1002/pc.29390.

[20] Ghulam Mustafa Memon et al. "Impact of mold temperature and fiber velocity on impregnation in carbon fiber polyamide 66 composites". In: *Physics of Fluids* (2025). DOI: 10.1063/5.0251030.

[21] Marco Tom Connor. "Consolidation mechanisms and interfacial phenomena in thermoplastic powder impregnated composites". en. PhD thesis. Lausanne: EPFL, 1995. DOI: 10.5075/epfl-thesis-1413. URL: https://infoscience.epfl.ch/handle/20.500.14299/209897.

[22] Kailashbalan Periasamy et al. "Interfacial Engineering Methods in Thermoplastic Composites: An Overview". In: *Polymers* 15.2 (2023). ISSN: 2073-4360. DOI: 10.3390/polym15020415. URL: https://www.mdpi.com/2073-4360/15/2/415.

[23] Osuke Ishida, Shiho Oda, and Kiyoshi Uzawa. "Impregnation process of large-tow carbon-fiber woven fabric/polyamide 6 composites using solvent method". In: *Composites Part A: Applied Science and Manufacturing* 180 (May 2024), p. 108068. ISSN: 1359-835X. DOI: 10.1016/J.COMPOSITESA.2024.108068. URL: https://www.sciencedirect.com/science/article/abs/pii/S1359835X24000654?via%3Dihub.

[24] Iakovos Tzanakis et al. "Cavitation in thermoplastic melts: New insights into ultrasound-assisted fibre-impregnation". In: *Composites Part B: Engineering* 229 (Jan. 2022), p. 109480. ISSN: 1359-8368. DOI: 10.1016/J.COMPOSITESB.2021.109480. URL: https://www.sciencedirect.com/science/article/pii/S1359836821008477?via%3Dihub.

[25] O. P.L. McGregor et al. “Pre-impregnated natural fibre-thermoplastic composite tape manufacture using a novel process”. In: *Composites Part A: Applied Science and Manufacturing* 101 (Oct. 2017), pp. 59–71. ISSN: 1359-835X. DOI: 10.1016/J.COMPOSITESA.2017.05.025. URL: https://www.sciencedirect.com/science/article/abs/pii/S1359835X17302087?via%3Dihub.

[26] Arnaud Saintonge et al. ““Hexacelsian slurry development for 2D woven alumina fiber impregnation in CMC fabrication””. In: *Open Ceramics* 19 (Sept. 2024), p. 100633. ISSN: 2666-5395. DOI: 10.1016/J.OCERAM.2024.100633. URL: https://www.sciencedirect.com/science/article/pii/S266653952400097X?via%3Dihub.

[27] Lakshmi Priya Muthe, Kim Pickering, and Christian Gauss. “Polylactide Composites Reinforced with Pre-Impregnated Natural Fibre and Continuous Cellulose Yarns for 3D Printing Applications”. In: *Materials* 17.22 (2024). ISSN: 1996-1944. DOI: 10.3390/ma17225554. URL: https://www.mdpi.com/1996-1944/17/22/5554.

[28] Hiroshi Nakamura et al. “Physical property control for innovative powder processes – Rheological control of concentrated slurry and wet granules”. In: *Advanced Powder Technology* 31.5 (May 2020), pp. 1784–1788. ISSN: 0921-8831. DOI: 10.1016/J.APT.2020.01.033. URL: https://www.sciencedirect.com/science/article/abs/pii/S0921883120300376?via%3Dihub.

[29] Xinwen Zhu, Dongliang Jiang, and Shouhong Tan. “The control of slurry rheology in the processing of reticulated porous ceramics”. In: *Materials Research Bulletin* 37.3 (Mar. 2002), pp. 541–553. ISSN: 0025-5408. DOI: 10.1016/S0025-5408(02)00674-8. URL: https://www.sciencedirect.com/science/article/abs/pii/S0025540802006748?via%3Dihub.

[30] Jiupeng Song et al. “The synergistic steric hindrance effect in the preparation of polyether ether ketone composites by powder slurry method”. In: *Polymer Composites* 43.4 (2022), pp. 2384–2395. DOI: https://doi.org/10.1002/pc.26548. URL: https://4spepublications.onlinelibrary.wiley.com/doi/abs/10.1002/pc.26548.

[31] F. Lindner, G. Puchas, and S. Schafföner. “Novel measuring method for prepreg processability of oxide fiber ceramic matrix composites”. In: *Composites Part A: Applied Science and Manufacturing* 162 (Nov. 2022), p. 107131. ISSN: 1359-835X. DOI: 10.1016/J.COMPOSITESA.2022.107131. URL: https://www.sciencedirect.com/science/article/abs/pii/S1359835X2200313X?via%3Dihub.

[32] Carlos Tiu, Lei Wang, and Ta Jo Liu. “Non-Newtonian effects on pre-metered reverse roll coating”. In: *Journal of Non-Newtonian Fluid Mechanics* 87.2-3 (Nov. 1999), pp. 247–261. ISSN: 0377-0257. DOI: 10.1016/S0377-0257(99)00066-X. URL: https://www.sciencedirect.com/science/article/abs/pii/S037702579900066X.

[33] Harvey Morpeth Thompson. “A theoretical investigation of roll coating phenomena”. May 1992. URL: https://etheses.whiterose.ac.uk/id/eprint/26364/.

[34] Texochem Industries. *Roller coating application techniques*. Mar. 2022.

[35] S. Tharmalingam and W. L. Wilkinson. “The coating of newtonian liquids onto a rotating roll”. In: *Chemical Engineering Science* 33.11 (Jan. 1978), pp. 1481–1487. ISSN: 0009-2509. DOI: 10.1016/0009-2509(78)85197-5. URL: https://www.sciencedirect.com/science/article/abs/pii/0009250978851975?via%3Dihub.

[36] Jiin-Yuh Jang and Peng-Yuan Chen. *Reverse Roll Coating Flow with Non-Newtonian Fluids*. Tech. rep. 3. 2009, pp. 536–552. DOI: https://doi.org/2009-CiCP-7691. URL: http://www.global-sci.com/.

[37] D D Edie et al. “THERMOPLASTIC COATING OF CARBON FIBERS N8 9-2 4 4 a8”. In: (1993). ISSN: 1988-1989.

[38] Eloi Andrieux. *Carbon fiber PEEK reinforced tape manufacturing: How does slurry properties and other process parameters influence final tape content and quality*. englsih. Tech. rep. Delft: TUDelft, Mar. 2025.

[39] P H Gaskell et al. "Modelling and analysis of meniscus roll coating". In: *Journal of Fluid Mechanics* 298 (1995), pp. 113–137. ISSN: 0022-1120. DOI: DOI : 10 . 1017 / S0022112095003247. URL: https : / / www . cambridge . org / core / product / C1E60EB81E924AEB65CE414E402A1AC8.

[40] H. Benkreira, M. F. Edwards, and W. L. Wilkinson. "A semi-empirical model of the forward roll coating flow of newtonian fluids". In: *Chemical Engineering Science* 36.2 (Jan. 1981), pp. 423–427. ISSN: 0009-2509. DOI: 10.1016/0009-2509(81)85024-5. URL: https : / / www . sciencedirect . com / science / article / abs / pii / 0009250981850245?via=ihub.

[41] Alexander Krok, Marián Peciar, and Roman Fekete. "Using the DPIV optical technique to measure the velocity of powder material in the space between the rollers in a roll compactor". In: *Powder Technology* 262 (2014), pp. 131–141. ISSN: 0032-5910. DOI: https : / / doi . org / 10 . 1016 / j . powtec . 2014 . 04 . 067. URL: https : //www.sciencedirect.com/science/article/pii/S0032591014003854.

[42] Fateh Ali et al. "Mathematical Analysis of Pseudoplastic Polymers during Reverse Roll-Coating". In: *Polymers* 12.10 (2020). ISSN: 2073-4360. DOI: 10.3390/polym12102285. URL: https://www.mdpi.com/2073-4360/12/10/2285.

[43] Hafiz Muhammad Atif, Fariha Jabeen, and Muhammad Asif Javed. "Mathematical study of viscoelastic polymer during roll-over-web coating". In: *Journal of Plastic Film & Sheeting* 40.1 (2024), pp. 30–50. DOI: 10 . 1177 / 87560879231204207. URL: https://doi.org/10.1177/87560879231204207.

[44] W B Russel. "Review of the Role of Colloidal Forces in the Rheology of Suspensions". In: *Journal of Rheology* 24.3 (June 1980), pp. 287–317. ISSN: 0148-6055. DOI: 10.1122/1.549564. URL: https://doi.org/10.1122/1.549564.

[45] L. Zhong et al. "Rheological behavior of xanthan gum solution related to shear thinning fluid delivery for subsurface remediation". In: *Journal of Hazardous Materials* 244-245 (Jan. 2013), pp. 160–170. ISSN: 0304-3894. DOI: 10.1016/J.JHAZMAT.2012.11.028. URL: https://www.sciencedirect.com/science/article/pii/S0304389412011193?via=ihub.

[46] Alireza Moradi, Changze Sun, and Zhongwei Guan. "Facilitating aqueous powder impregnation for manufacturing thermoplastic composites: A prepreg rig design and process optimisation". In: *Journal of Reinforced Plastics and Composites* 0.0 (2024), p. 07316844241243127. DOI: 10.1177/07316844241243127. URL: https://doi.org/10.1177/07316844241243127.

[47] Federico Peruzzini et al. "An effective viscosity model for suspensions of non-Brownian particles in aqueous xanthan gum matrices". In: *Rheologica Acta* 64.6 (2025), pp. 293–314. ISSN: 1435-1528. DOI: 10.1007/s00397-025-01508-9. URL: https://doi.org/10.1007/s00397-025-01508-9.

[48] Tamer A Sebaey, Mohamed Bouhrara, and Noel O'Dowd. "Fibre Alignment and Void Assessment in Thermoplastic Carbon Fibre Reinforced Polymers Manufactured by Automated Tape Placement". In: *Polymers* 13.3 (2021). ISSN: 2073-4360. DOI: 10.3390/polym13030473. URL: https://www.mdpi.com/2073-4360/13/3/473.

[49] David Hartung et al. "Manufacturing and Analysis of Natural Fiber-Reinforced Thermoplastic Tapes Using a Novel Process Assembly". In: *Sustainability* 15.7 (2023). ISSN: 2071-1050. DOI: 10.3390/su15076250. URL: https://www.mdpi.com/2071-1050/15/7/6250.

[50] MALVERN PANALYTICAL. *OPTIMIZING METAL POWDERS FOR ADDITIVE MANUFACTURING*. 2020.

[51] Kenro Mitsuda, Hiroshi Kimura, and Toshiaki Murahashi. "Evaporation and decomposition of Triton X-100 under various gases and temperatures". In: *Journal of Materials Science* 24.2 (1989), pp. 413–419. ISSN: 1573-4803. DOI: 10.1007/BF01107420. URL: https://doi.org/10.1007/BF01107420.

[52] Fiji team. *Fiji*.